

An investigation of optical properties in active and passive nanophotonic devices

PhD Thesis

Dun Qiao

A submission presented in partial fulfilment of the requirement of the University of South Wales / Prifysgol De Cymru for the degree of Doctor of Philosophy

Feb 2023

The logo of the University of South Wales, featuring a red square with rounded corners containing the text "University of South Wales" and "Prifysgol De Cymru" in white.

University of
South Wales
Prifysgol
De Cymru

Acknowledgement

I am grateful for the detailed and patient supervision by Dr Kang Li and Prof. Nigel Copner. Their insightful guidance on both theory and experiment work supported me in finishing this PhD project.

I would like to give my special appreciation to Prof. Guojie Chen and Dr Lai at Foshan University. Without your kind support, I could not be pursuing my academic career.

I wish to say a big thank you to all academic staff at WORIC of the University of South Wales, Dr Peter Rees, and Dr Yuanlong Fan, for your valuable advice on simulation and calculation, which help me a lot during PhD study.

I would like to thank Mr Adam Jones, Mr Yusuf Abubakar, Mr Sivagunalan Sicanathan, Mr Mahmud Sahal, Mr Chris Evered, Miss Bethan Copner, Mr Jiuyuan Zhu and Mr Yang Zhou. As my colleague at USW, brainstorming and valuable discussion among us inspire me greatly towards the research work.

I want to give special thanks to Dr Micheal Campell and Dr Ben Hughes from NPL for supporting the project.

I'm also thankful to Prof. Marc sorel and Dr Eugenio Di Gaetano from The University of Glasgow, their team gave me precious advice for the sample fabrication and fabricated the chip sample.

Thank you, my mom and dad. Your support and sacrifice give me the opportunity to pursue the academic career.

For my wife Jingyi Feng, thank you for always encouraging me. Without your patience and unconditional love, I can not get through this PhD journey.

Abstract

This thesis describes the simulation and experiment work of nanostructure design for active and passive nanophotonics devices.

The active device part focuses on organic light-emitting diodes (OLEDs), widely used new-generation display devices. The attention is concentrated on improving the light extraction of OLED devices, and different nanostructures are proposed based on numerical simulation for addressing the losses driven by surface plasma polariton and guided mode in OLEDs. Particularly, a novel polarized OLED structure based on photo cross-linkable luminescent mesogenic EML material is reported.

The passive device part introduces the development of a symmetrical dual-sweep source for the Frequency Scanning Interferometry (FSI) system based on Four Wave Mixing (FWM) in Silicon on Insulator (SOI) nano waveguides. Systematic research of non-linear optics in silicon is conducted, which paves the way for numerical simulation and further guides the design of SOI chips. Besides, corresponding fibre-to-chip coupling solutions are also proposed based on numerical simulation. The designed chip is tested experimentally, and the FWM phenomenon is investigated and discussed.

List of Publications during PhD study

1. Qiao, D., Li, K., Sivanathan, S., Copner, B., Copner, N., Campbell, M. and Hughes, B., 2023, January. Dual-frequency sweeping light source based on four-wave mixing in silicon-on-insulator nano-waveguide. In *Emerging Applications in Silicon Photonics III* (Vol. 12334, pp. 28-35). SPIE.
2. Zhu, J., Qiao, D., Jones, A., Zhang, B., Li, K. and Copner, N., 2023. 1.7 THz tuning range pivot-point-independent mode-hop-free external cavity diode laser. *Optics Express*, 31(3), pp.3970-3983.
3. Qiao, D., Chen, G., Gong, Y., Li, K., Fan, Y., Zhang, B., Jia, F., Abubakar, Y., Jones, A., Otung, I. and Copner, N., 2020. Design and optical characterization of an efficient polarized organic light emitting diode based on refractive index modulation in the emitting layer. *Optics Express*, 28(26), pp.40131-40144.
4. Qiao, D., Li, K., Copner, N., Gong, Y. and Chen, G., 2019, August. The Enhanced Light Extraction Top-emitting Organic Light-emitting Diode Based on Metallic Grating Anode. In *2019 IEEE International Conference on Manipulation, Manufacturing and Measurement on the Nanoscale (3M-NANO)* (pp. 49-52). IEEE.
5. Abubakar, Y., Gong, Y., Qiao, D., Fan, Y., Evered, C., Jones, A., Saleh, H.D., Li, K. and Copner, N., 2021. Enhanced narrowband mid-IR thermal radiation enabled by plasmonic stacked gratings. *OSA Continuum*, 4(9), pp.2481-2487.

Content

Acknowledgement	i
Abstract.....	ii
List of Publications during PhD study	iii
Content.....	iv
List of figures.....	viii
List of tables	xv
Chapter 1 Introduction	- 1 -
1.1 Research background	- 1 -
1.2 Motivation of the PhD project	- 2 -
1.3 Thesis structure	- 3 -
Chapter 2 Theory and methods for Photonic simulation	- 5 -
2.1 Maxwell’s equation.....	- 5 -
2.2 Finite-difference time-domain (FDTD) methods.....	- 6 -
2.3 Finite element simulation.....	- 12 -
2.4 Other numerical simulation methods	- 14 -
Chapter 3 Study of Active Devices – OLEDs.....	- 17 -
Disclaimer.....	- 17 -
3.1 Introduction.....	- 17 -
3.1.1 Optical losses of conventional OLED	- 17 -
3.1.2 Limitation of conventional bottom-emitting OLED	- 19 -
3.1.3 Limitation of the light extraction of polarized OLED.....	- 20 -
3.2 The target of this chapter	- 21 -

3.3	Design and simulation of TEOLED with metallic grating anode	- 22 -
3.3.1	Simulation model and mode analysis	- 22 -
3.3.2	optimization of the design of metallic grating anode	- 24 -
3.4	Design and simulation for enhancing light extraction of polarized OLEDs	- 26 -
3.4.1	Luminescent liquid crystal for the emission layer.....	- 27 -
3.4.1	Losses mode analysis of polarized OLEDs based on luminescent Liquid Crystal	- 30 -
3.4.2	Light extraction by refractive index gratings in EML.....	- 33 -
3.4.3	Enhancing polarized ratio with an extra crystallized emitting layer	- 40 -
3.5	Conclusion	- 43 -
Chapter 4	Study of Passive Devices – FWM on SOI waveguides.....	- 44 -
4.1	Introduction	- 44 -
4.1.1	Integrated Photonics	- 44 -
4.1.2	silicon waveguide and non-linear effect.....	- 47 -
4.2	The target of this chapter	- 50 -
4.3	Theory of non-linear optical effects in the silicon waveguide.....	- 52 -
4.3.1	The Optical Kerr effect in SOI material	- 53 -
4.3.2	Two-Photon Absorption	- 54 -
4.3.3	Free Carrier Absorption.....	- 56 -
4.3.4	Stimulated Brillouin Scattering in the silicon waveguide	- 57 -
4.3.5	The FWM in the silicon waveguide	- 58 -
4.4	Design and numerical simulation of SOI waveguide for FWM	- 62 -
4.4.1	Mode analysis of silicon waveguide.....	- 63 -
4.4.2	Dispersion modulation and FWM conversion calculation	- 67 -

4.5	Fibre-to-waveguide coupling	- 74 -
4.5.1	Simulation of the grating coupler	- 78 -
4.5.2	Design and simulation of edge coupler I: SU-8 covered taper coupler.....	- 79 -
4.5.3	Design and simulation of edge coupler II: Free space taper coupler -	85 -
4.5.4	Insertion loss from lensed fibre to edge coupler	- 88 -
4.6	Conclusion	- 90 -
Chapter 5	Experiment	- 91 -
5.1	Experimental set up.....	- 91 -
5.1.1	SOI chip samples	- 91 -
5.1.2	Manually alignment system.....	- 92 -
5.1.3	FWM testing system layout.....	- 93 -
5.2	Experiment 1: Coupling efficiency test	- 97 -
5.2.1	Coupling test of SU8-1	- 98 -
5.2.2	Coupling test of SU8-2.....	- 100 -
5.2.3	Coupling test of SU8-3.....	- 101 -
5.2.4	Coupling test of SU8-4.....	- 103 -
5.3	Experiment 2: FWM conversion efficiency test	- 105 -
5.3.1	Wideband FWM test of SOI chip.....	- 105 -
5.3.2	Wide band FWM test of HNLF.....	- 108 -
5.3.3	Wideband FWM test of nonlinear SOA	- 110 -
5.4	Experiment 3: Dual-Frequency sweeping (filtered FWM) measurement-	112 -
5.5	Conclusion	- 116 -
Chapter 6	Summary and Outlook.....	- 117 -
6.1	Contribution to knowledge.....	- 117 -

6.2	Limitation of work in thesis	- 118 -
6.3	Prospective work.....	- 118 -
	Bibliography	- 117 -
	Appendix.....	- 127 -
A.1	Script for CNSE method	- 127 -
A.2	Mask Drawing for lithography.....	- 130 -
A.3	SOI chip with free space coupler	- 133 -

List of figures

Figure 2.1 The Yee lattice and grid of FDTD methods.	- 9 -
Figure 2.2 The parameters of PML boundary	- 11 -
Figure 2.3 The meshing of FEM.....	- 13 -
Figure 3.1 Optical losses of conventional OLEDs	- 18 -
Figure 3.2 Structure of (a) Bottom-emitting and (b) Top-emitting OLED.....	- 20 -
Figure 3.3 Illustration of the proposed TEOLED structure with Ag nano-grating anode... ..	- 23 -
Figure 3.4 The 2D FEM simulated normalized field distribution E of TEOLED. (a) with flat Ag film anode (b) with Ag nanograting anode. The normalized intensity (E_2) of TEOLED (c) with flat Ag film anode (d) with Ag nanograting anode.	- 24 -
Figure 3.5 Emission spectra of normalized intensity with wavelength (a) for the different grating depth, (b) for the different grating periods.	- 25 -
Figure 3.6 The emission angular responses obtained by FDTD simulation.....	- 26 -
Figure 3.7 Potential molecule structure of EML material (BDAVB _i derivation) used in the manuscript.....	- 28 -
Figure 3.8 Model of the polarized OLED with crystallized EML.....	- 29 -
Figure 3.9 (a) 2D structure of OLEDs (XoZ plane), (b) Aligned rod-like shape molecules in the plane of EML from the top view(XoY plane), (c) Randomly distributed rod-like shape molecules in the plane of amorphous EML from the top view(XoY plane).	- 30 -
Figure 3.10 (a) Multi-layer structure of OLEDs with amorphous emitting layer; (b) Structure of OLED with crystallized emitting layer; (c) Normalized intensity distribution of lossy mode in OLEDs with amorphous emitting layer; (d) Normalized intensity distribution of lossy mode in OLEDs with crystallized emitting layer, the TE lossy mode is confined in emitting layer due to high ordinary refractive index;	- 32 -

Figure 3.11 The OLEDs structure with refractive index grating in its emitting layer, the amorphous and crystallized areas are arranged along the x-axis, T is the grating period, $F=A/T$ represent the fill factor of grating, and A is the width of crystallized areas. - 33 -

Figure 3.12 Simulated the electric field intensity distribution via side view. (a) Grating structure. (b) Non-grating structure. - 34 -

Figure 3.13 External quantum efficiency simulated for the reference device and devices with grating structures with different periods and different thicknesses of EML. (a) The EQE of the grating period from 200 nm to 600 nm with EML thickness at 50 nm, (b) The EQE of the grating period from 200 nm to 600 nm with EML thickness at 60 nm, (c) The EQE of the grating period from 200 nm to 600 nm with EML thickness at 70 nm, (d) The EQE of the grating period from 200 nm to 600 nm with EML thickness at 80 nm - 36 -

Figure 3.14 Purcell factor spectrum simulated for the reference device and devices with a thickness of EML of 50 nm. - 37 -

Figure 3.15 Simulation of the far field electric intensity distribution of reference devices and grating structure in TE and TM polarization, respectively. (a, b) The reference devices. (c, d) The grating structures ($T=400$ nm, EML thickness= 50 nm)..... - 38 -

Figure 3.16 Polarized ratio simulated for the reference device and devices with grating structures with different periods and different thicknesses of EML. (a) The Polarized ratio of the grating period from 200 nm to 600 nm with EML thickness at 50 nm, (b) The Polarized ratio of the grating period from 200 nm to 600 nm with EML thickness at 60 nm, (c) The Polarized ratio of the grating period from 200 nm to 600 nm with EML thickness at 70 nm, (d) The Polarized ratio of the grating period from 200 nm to 600 nm with EML thickness at 80 nm..... - 39 -

Figure 3.17 (a) EQE simulated for the reference device and devices with grating structures with different fill factors. (b) The polarized ratio of grating structure with different fill factors ($T=500$ nm)..... - 40 -

Figure 3.18 The OLED structure with an extra crystallized emitting layer underneath the grating structure. d is the thickness of the extra crystallized emitting layer..... - 41 -

Figure 3.19 EQE spectrum simulated for the reference device and devices with grating structures with different thicknesses of the extra emitting layer. (b) The polarized ratio of structure with different thicknesses d of extra emitting layer ($T=500$ nm, $F=0.3$).....	- 41 -
Figure 3.20 Normalized far-field intensity as a function of the viewing angle. ($T=500$ nm, $F=0.3$, emission wavelength=550 nm).	- 42 -
Figure 4.1 The structure of Silicon on Insulator (SOI) wafer with 220nm SOI layer.	- 47 -
Figure 4.2 Three typical structures of SOI waveguide. (a) Ridge/Wire waveguide. (b) Rib waveguide. (c) Slot waveguide.	- 48 -
Figure 4.3 Schematic of different non-linear optics processes. (a) SHG, (b) THG, (c) SFG, (d) FWM.....	- 49 -
Figure 4.4 (a) Basic schematic of FSI system. (b) Principle of FSI system.	- 51 -
Figure 4.5 Measured βTPA for 125 μm thick silicon wafer (black square) as a function of wavelength; Best fitting based on calculation from Garcia and Kalyanarama (solid red line).	- 55 -
Figure 4.6 Schematic of TPA in silicon (a) Degenerated TPA (b) Non-degenerated TPA.	- 56 -
Figure 4.7 Schematic of FWM in silicon (a) Energy level diagram of single mode Non-degenerated FWM, (b) frequency view of Non-degenerated FWM, (c) Energy level diagram of single mode Degenerated FWM (d) frequency view of Degenerated FWM.....	- 59 -
Figure 4.8 Geometry of buried SOI waveguide for simulation.	- 63 -
Figure 4.9 Calculated effective index of modes in 220 nm thick strip SOI waveguide versus width of waveguide.	- 64 -
Figure 4.10 Normalized E field intensity of TE modes of 1546 nm light wave for 220nm thick SOI waveguide with width sweeping from 300 nm to 700 nm; (a) TE0 of $W = 300$ nm, (b) TE0 of $W = 400$ nm, (c) TE0 of $W = 450$ nm, (d) TE0 of $W = 500$ nm, (e) TE0 of $W = 550$ nm, (f) TE0 of $W = 600$ nm, (g) TE0 of $W = 700$ nm, (h) TE1 of $W = 700$ nm, (i) TE2 of $W = 700$ nm.	- 65 -

Figure 4.11 Effective index and mode area of TE0 mode of strip waveguide with different width (a) effective index versus wavelength (b) effective mode area versus wavelength.....	- 66 -
Figure 4.12 The high order dispersion and linear phase mismatch versus signal wavelengths, the pump wavelength is 1546 nm. (a) Beta 2 versus signal wavelengths, (b) Beta 4 versus signal wavelengths, (c) Linear phase mismatch versus signal wavelengths, (d) $\Delta k_{Linear} \cdot L/\pi$ versus signal wavelengths	- 69 -
Figure 4.13 (a) The GVD of different width SOI waveguides with 220nm height. (b) the Phase mismatch versus signal wavelength. (c) the conversion efficiency calculated by the CNSE method. (d) the conversion efficiency is calculated by Small Signal Approximation method. Here the pump energy is set as 15 dBm, the coupling length is 10 mm, and the pump wavelength is 1546 nm.	- 71 -
Figure 4.14 The length sweeping of conversion efficiency, the width is 500 nm, the pump power is 15 dBm at 1546 nm (a) the result of CNSE versus signal wavelength of different coupling length (b) the result of small signal approximation versus signal wavelength of different coupling length.	- 72 -
Figure 4.15 The fine length sweeping result solved by CNSE, the width is 500 nm, the pump power is 15 dBm at 1546 nm, the max conversion efficiency and conversion bandwidth versus coupling length is shown.	- 73 -
Figure 4.16 Conversion of different pump energy versus signal wavelength, where the width is 500 nm, length is 2.2 mm, and pump wavelength is 1546 nm.....	- 74 -
Figure 4.17 Schematic of typical edge coupling taper coupler. (a) Forward taper coupler. (b)Inverse taper coupler.....	- 75 -
Figure 4.18 (a) The schematic of a grating coupler and the four propagating directions in the grating coupler. (b) The cross-section (from plane XoZ) of the grating coupler. .	- 77 -
Figure 4.19 Normalized E field of cross-section (from XoZ plane) of the grating coupler, the grating period is $T = 750 \text{ nm}$, $\Lambda = 375 \text{ nm}$. Incident wavelength is 1548 nm.....	- 78 -

Figure 4.20 The 2D-FDTD simulated coupling efficiency of a grating coupler for 220 nm thick SOI waveguide, the grating period is 750 nm, and the grating fill factor is 0.5.	- 79 -
Figure 4.21 The simulation model of the Su-8 taper coupler.	- 80 -
Figure 4.22 EIM calculated the effective index of modes of SU-8 outer waveguide. (Width $W_s=3 \mu m$, Thickness H_s sweeping from 0 to 3 μm)	- 81 -
Figure 4.23 Coupling efficiency versus taper length of different Width SU8 waveguides. ($W_{tip} = 80nm$, $W_S = 3\mu m, \lambda = 1546nm$).....	- 82 -
Figure 4.24 The Normalized E profile of SU-8 taper coupler ($W_t = 80nm$, $L_t = 50\mu m$, $\lambda = 1546nm$). (a) Top view (XoY plane). (b) Side view (XoZ plane) -	- 83 -
Figure 4.25 Normalized E field for different propagating distances, cross-section profile form YoZ plane. (a) X=40 μm , (b) X=30 μm , (c) X=20 μm , (d) X=10 μm , (e) X=5 μm , (f) X=0 μm , (g) X=-5 μm , (h) X=-10 μm , (i) X=-30 μm , (j) X=-50 μm	- 84 -
Figure 4.26 (a) The coupling efficiency versus wavelength of different taper lengths. (b) The coupling efficiency versus tip width of different taper lengths.....	- 85 -
Figure 4.27 The simulation model of the free space coupler.	- 86 -
Figure 4.28 The simulated E profile of the direct taper coupler ($W_{tip} = 100 nm$, $L_e = 25 \mu m$ $L_t = 50 \mu m$). (a) Top view (XoY plane). (b) Side view (XoZ plane) . -	- 87 -
Figure 4.29 Coupling efficiency versus Taper Length of the free space taper coupler with $W_{tip} = 100 nm$ and $\lambda = 1546 nm$	- 88 -
Figure 4.30 Schematic of the simulation model of lensed fibre to coupler facet coupling.	- 89 -
Figure 4.31 Coupling efficiency versus fibre to waveguide distance LG for different beam waists respectively.	- 90 -
Figure 5.1 Photos of the first batch of SOI chips (with SU-8 covered taper coupler), from left to right is the chips No. 1,2,3, and 4, respectively.....	- 91 -

Figure 5.2 Photos of the second batch of SOI chips (with free space taper coupler), from left to right is the chip no 1 and 2, respectively	- 92 -
Figure 5.3 The fibre-to-waveguide alignment system.....	- 93 -
Figure 5.4 Block diagram of the experimental testing system of SOI waveguide.	- 93 -
Figure 5.5 Block diagram of an experimental testing system for HNLF.	- 95 -
Figure 5.6 Block diagram of the experimental testing system for Non-linear SOA. .	- 95 -
Figure 5.7 Microscope view of SOI waveguide with SU-8 covered taper coupler No.1. ...	- 98 -
Figure 5.8 Microscope view of SOI waveguide with SU-8 covered taper coupler No.2. ...	- 100 -
Figure 5.9 Microscope view of SOI waveguide with SU-8 covered taper coupler No.3. ...	- 101 -
Figure 5.10 Microscope view of SOI waveguide with SU-8 covered taper coupler No.4.	- 103 -
Figure 5.11 Measured FWM spectrum of SOI chip by OSA. (a) FWM spectrum of the smallest detuning. (b) FWM spectrum of the largest detuning.	- 106 -
Figure 5.12 Measured wide band FWM results of SOI chip. (a) The SNR of idler SNR_i versus wavelength detuning $\Delta\lambda$, including sampled data points and fitting curve. (b) The conversion efficiency versus wavelength detuning $\Delta\lambda$, including sampled data points and fitting curve.	- 107 -
Figure 5.13 Measured FWM spectrum of HNLF1 by OSA. (a) FWM spectrum of the smallest detuning. (b) FWM spectrum of the largest detuning.	- 108 -
Figure 5.14 Measured wide band FWM results of HNLF1. (a) The SNR of idler SNR_i versus wavelength detuning $\Delta\lambda$, including sampled data points and fitting curve. (b) The conversion efficiency versus wavelength detuning $\Delta\lambda$, including sampled data points and fitting curve.	- 109 -
Figure 5.15 Measured FWM spectrum of HNLF2 chip by OSA. (a) FWM spectrum of the smallest detuning. (b) FWM spectrum of the largest detuning.....	- 110 -

Figure 5.16 Measured wide band FWM results of HNLF2. (a) The SNR of idler SNR_i versus wavelength detuning $\Delta\lambda$, including sampled data points and fitting curve. (b) The conversion efficiency versus wavelength detuning $\Delta\lambda$, including sampled data points and fitting curve.	- 110 -
Figure 5.17 Measured FWM spectrum of Non-linear SOA by OSA. (a) FWM spectrum of the smallest detuning. (b) FWM spectrum of the largest detuning.	- 111 -
Figure 5.18 Measured wide band FWM results of Non-linear SOA. (a) The SNR of idler SNR_i versus wavelength detuning $\Delta\lambda$, including sampled data points and fitting curve. (b) The conversion efficiency versus wavelength detuning $\Delta\lambda$, including sampled data points and fitting curve.	- 112 -
Figure 5.19 Transmission spectrums of long-pass and notch filter. (a) Long-pass filter. (b) Notch filter.	- 113 -
Figure 5.20 Dual sweeping generated by SOI waveguide. The left-side peaks are the filtered signal light plus the original signal light, and the right-side peaks are the idler peak after EDFA 3.....	- 114 -
Figure 5.21 Dual sweeping generated by HNLF 1. The left-side peaks are the filtered signal light plus the original signal light, and the right-side peaks are the idler peak after EDFA 3.....	- 114 -
Figure 5.22 Dual sweeping generated by HNLF 2. The left-side peaks are the filtered signal light plus the original signal light, and the right-side peaks are the idler peak after EDFA 3.....	- 115 -
Figure 5.23 Dual sweeping generated by Non-linear SOA. The left-side peaks are the filtered signal light plus the original signal light, and the right-side peaks are the idler peak after EDFA 3.....	- 115 -

List of tables

Table 2.1 Comparison among different simulation methods.....	- 15 -
Table 3.1 Refractive indices and the thickness of each layer	- 31 -
Table 4.1 Parameters for dispersion modulation and FWM simulation of SOI waveguide.	- 67 -
Table 5.1 Inventory list of adopted equipment	- 96 -
Table 5.2 Coupling test results of waveguide SU8-1.	- 99 -
Table 5.3 Coupling test results of waveguide SU8-2.	- 101 -
Table 5.4 Coupling test results of waveguide SU8-3.	- 102 -
Table 5.5 Coupling test results of waveguide SU8-4.	- 103 -
Table 5.6 Comparison among the FWM techniques based on experimental results	- 116 -

Chapter 1

Introduction

1.1 Research background

Since the 1960s, the development of microelectronics has given birth to the information revolution. Nowadays, expanding market scale requires advanced hardware every year for various aspects, such as processing, transmitting, display, sensing, and energy generating, which is beyond the conventional electronic systems' capabilities due to the physical limitation of the electron-basing systems predicted by Gordon Moore's law [1]. Light, or photons, has been seen as a decent medium for transmitting information since the 1970s [2] due to broadband characteristics, fast response, high volume data storage, as well as compatibility with modern electronic systems, thanks to the photoelectric effect summarized by Albert Einstein et al. [3]. Since the first Laser was demonstrated, various devices based on photonics technologies have been invented. In recent years, photonics technology has been seen as the next breakpoint for the information revolution. However, for a long time, the wide application and dense integration of photonics devices have been limited by the volume of devices and complicated structures for different purposes. Fortunately, photonics devices are compatible with advanced modern nano fabrication techniques promoted by the microelectronic industry, which pave a way for the miniaturisation of photonics devices and push the scale of photonic research down to the nanometre scale.

Nanophotonics studies the light-matter interaction and light behaviour at the nanometre level. The device is always the main topic of nanophotonic research. Like electronic devices, photonic systems are categorized as active and passive. Active devices involve energy conversion between photons and electrons, for instance, Lasers, photodetectors, optical switches, light sources, photovoltaics, active modulators, and solid-state imaging devices. Passive devices only relate to photons transferring and guiding. Optical fibres, waveguides, filters, polarizing controllers, attenuators, couplers, multiplexers and demultiplexers are

typically passive devices. Different purposing functions and material requirements of those devices challenge the photonics design.

A successful design of nanophotonic devices or structures allows researchers to effectively manipulate and control the light phenomena in wavelengths or sub-wavelengths for achieving different objectives. Nanophotonic devices are generally developed based on various classic prototypes, including photonic crystals, multilayer resonance cavities, nano gratings, ring resonators, and surface plasma polaritons (SPPs) arrays. With those structures, high-quality optical resonance is feasible by reducing the group velocity of electromagnetic waves and spatially confining the field at the subwavelength level, which is used in many devices. Photonic crystals and similar periodic structures are employed in active devices such as OLEDs to enhance their luminescence. Multilayer cavities, ring cavities, and cavities with other structures are applied in laser sources, filters, and detectors. SPPs are utilised for tailoring spectrum and optimising waveguides. Working wavelength and functions for all these structures are programmable with dimension and material adjustment. Modern computer technology and electromagnetic theories supply tools to researchers for predicting and optimizing devices' performance.

1.2 Motivation of the PhD project

This thesis includes two subprojects based on the nanophotonic design. The first is the design of active devices, namely the OLEDs, and another one is about the design of passive devices, in specific, the SOI waveguide for high efficiency and broadband FWM conversion on C band.

For the subproject about active devices part, the company partner of our research group held a patent for a novel cross-linkable luminescent liquid crystal material [4], which is promising to be applied in polarized OLEDs devices to overcome the in-plane emission losses. However, before the large-scale commercial application of such luminescent material, a proper nanophotonic structure design is required to quantitatively identify the potential performance and optimized geometrical design of the structure, which adopts this novel material. Besides, other technique to eliminate the other optical losses in OLEDs devices is vital as well for this project. My work investigated various techniques to reduce the optical losses in OLEDs, and analysed

the performance of OLED devices with this novel liquid crystal material as the emissive layer by comprehensive numerical simulation.

The subproject about the passive devices is initiated by our partner National Physics Laboratory (NPL), the project was looking for a solution to motion-induced errors in the FSI distance metrology system for high-value manufacturing, and the FWM was chosen as a promising approach to supply a dual-sweep laser source, which is the key point for motion error compensating FSI system. Previous research has been done by the FWM on the non-linear SOA [5]. The new approach is tending to use the SOI nano waveguide due to its small size and high nonlinear coefficient, and relative ease of acquisition, which benefits the miniaturisation and compactivity of the whole FSI system. However, to precisely manipulate the laser beam by FWM on SOI nano waveguide, a careful nanophotonic design needs to be carried out, which is covered by my work in this thesis. I have numerically analysed the non-linear properties of SOI waveguides by both simulation and experiment. The outcome of my work supplies a usable design of SOI chip that be applied for the dual sweep laser source for the FSI system.

1.3 Thesis structure

This thesis introduces the author's work towards the design of both active and passive nanophotonic devices, including OLEDs and SOI waveguides for wavelength conversion. The thesis contains three main chapters.

Chapter 2 looks at the simulation algorithm for photonics design. As the significant methodology for modern photonics design, especially the nanophotonic devices, the computational simulation methods based on classic electromagnetic theory are introduced. The simulation methods, including FDTD and FEM, employed as design tools in this thesis are discussed in detail.

Chapter 3 introduced subproject about active devices accomplished by the author, two types of active devices are introduced and researched, including TEOLEDs and polarized OLEDs. A novel top-emitting OLED with Ag grating anode is proposed for OLEDs first. An enhanced extraction structure based on luminescent liquid crystal for highly polarized OLED is proposed based on comprehensive simulation and discussion. The scenario of enhancement is introduced from the molecule level.

The subproject of passive devices is introduced in chapter 4. The objective is to develop on chip FWM conversion module with high conversion efficiency and broad conversion bandwidth for dual-frequency FSI systems. Systematic research about the non-linear effect in SOI waveguides is described, and an optimized design of SOI waveguide for FWM is proposed based on simulation. The fibre-to-waveguide coupler is then investigated and discussed. Two optimized edge coupler designs are presented based on simulation and fabrication perspectives.

Chapter 5 introduced the experiment about SOI waveguide and corresponding fibre to waveguide coupler. The SOI chips are fabricated and tested, and the result suggests the proposed design can significantly enhance the accuracy of the dual frequency FSI system, which is the first time an SOI waveguide has been applied to an FSI distance measurement system.

Eventually, chapter 6 summarises this thesis's work, emphasises the contribution to new knowledge about all the works introduced in this thesis, and gives a detailed future optimization perspective for all designs described in this thesis.

Chapter 2

Theory and methods for Photonic simulation

Current nanophotonic design is based on the electromagnetic theory, which has been developed for over a century since Maxwell's equations were proposed in 1873. For a simple optical structure or model, an analytical solution is easy to be obtained by theoretical derivation. However, the propagation of light in the natural environment is utterly complicated. For devices requiring practical applications, a numerical simulation based on corresponding input environmental parameters and compatible boundary conditions is necessary, which brings the researcher's ability to predict the performance of photonic devices and to find the optimized design in theory before production, thus saving both time and cost. In recent years, With the rapid development of computer science and electronic technology, the computing ability of modern computers has been significantly enhanced, making the computer assistant numerical electromagnetic simulation a more and more vital process in photonic design. Many theoretical algorithms are achieved by several program languages, including C, C++, Matlab and Python. Besides, many commercialized electromagnetic simulation software with more advanced features have been launched, including Comsol and Lumerical. In this Chapter, the Basic electromagnetic theory is introduced first, and then a series of numerical simulation methods adopted for the simulation of both active and passive photonic devices in this thesis are introduced.

2.1 Maxwell's equation

Light is a particular electromagnetic wave, and its transmitting obeys the same law as other electromagnetic waves. Based on classical electromagnetism theory, all electromagnetic phenomena can be described by the famous Maxwell's equations, which are given by

$$\begin{cases} \nabla \times \vec{E} = -\frac{\partial \vec{B}}{\partial t} \\ \nabla \times \vec{H} = J + \frac{\partial \vec{D}}{\partial t} \\ \nabla \cdot \vec{D} = \rho \\ \nabla \cdot \vec{B} = 0 \end{cases} \quad (2.1)$$

where the \vec{E} and \vec{H} are the intensity of the electric field and magnetic field, respectively. ρ is the free charge density of the medium. \vec{D} , \vec{B} and J are the electric displacement field, magnetic flux density, and free current density, respectively. They can be given by following equations

$$\begin{cases} \vec{D} = \epsilon_0 \vec{E} + \vec{P} \\ \vec{B} = \mu_0 \vec{H} + \mu_0 \vec{M}, \\ J = \sigma \vec{E} \end{cases} \quad (2.2)$$

where the \vec{P} , \vec{M} and σ are electrical polarization, magnetic polarization, and conductivity of the medium, respectively. ϵ_0 and μ_0 are permittivity and permeability of the vacuum, respectively. Interaction between light and matter is mainly electric interaction so that the medium can be assumed as non-magnetic without free charge, thus $\vec{M} = 0$, $J = 0$ and $\rho = 0$ respectively. With these conditions, equation 2.1 is then rearranged to

$$\begin{cases} \nabla \times \vec{E} = -\mu_0 \frac{\partial \vec{B}}{\partial t} \\ \nabla \times \vec{H} = \epsilon_0 \frac{\partial \vec{D}}{\partial t} \\ \nabla \cdot \vec{D} = 0 \\ \nabla \cdot \vec{B} = 0 \end{cases} \quad (2.3)$$

2.2 Finite-difference time-domain (FDTD) methods

K.S.Yee initials the FDTD in 1966 [6]; it is a numerical simulation that can obtain the distribution of the electromagnetic field in the time-domain by iterative calculation of Maxwell's equation based on substituting the continuous partial derivative of curl equation of Maxwell's equations with discrete finite-difference.

According to the curl equation of Maxwell's equation in equation 2.3, the curl equation in differential form can be given by

$$\begin{cases} \frac{\partial \vec{H}}{\partial t} = -\frac{1}{\mu} \nabla \times \vec{E} - \frac{\rho}{\mu} \vec{H} \\ \frac{\partial \vec{E}}{\partial t} = -\frac{1}{\varepsilon} \nabla \times \vec{H} - \frac{\sigma}{\varepsilon} \vec{E} \end{cases} \quad (2.4)$$

In the Cartesian coordinate system, both the \vec{E} and \vec{H} has their three corresponding components in three coordinate directions, respectively. Therefore the equation is rearranged to [7]

$$\begin{cases} \frac{\partial E_x}{\partial t} = \frac{1}{\varepsilon} \left[\frac{\partial H_z}{\partial y} - \frac{\partial H_y}{\partial z} - \sigma E_x \right] \\ \frac{\partial E_y}{\partial t} = \frac{1}{\varepsilon} \left[\frac{\partial H_x}{\partial z} - \frac{\partial H_z}{\partial x} - \sigma E_y \right] \\ \frac{\partial E_z}{\partial t} = \frac{1}{\varepsilon} \left[\frac{\partial H_y}{\partial x} - \frac{\partial H_x}{\partial y} - \sigma E_z \right] \end{cases} \quad (2.5)$$

and

$$\begin{cases} \frac{\partial H_x}{\partial t} = \frac{1}{\mu} \left[\frac{\partial E_z}{\partial y} - \frac{\partial E_y}{\partial z} - \rho H_x \right] \\ \frac{\partial H_y}{\partial t} = \frac{1}{\mu} \left[\frac{\partial E_x}{\partial z} - \frac{\partial E_z}{\partial x} - \rho H_y \right] \\ \frac{\partial H_z}{\partial t} = \frac{1}{\mu} \left[\frac{\partial E_y}{\partial x} - \frac{\partial E_x}{\partial y} - \rho H_z \right] \end{cases} \quad (2.6)$$

In the Cartesian coordinate system, any components of both \vec{E} and \vec{H} can be represented by a function relating to time and position $f(x, y, z, t)$, its discrete in time and the spatial domain is given by,

$$f(x, y, z, t) = f(i\Delta x, j\Delta y, k\Delta z, n\Delta t) = f^n(i, j, k). \quad (2.7)$$

By applying central difference approximation for the partial derivative of $f(x, y, z, t)$ with respect to time and spatial components, respectively, the following equations are obtained.

$$\left\{ \begin{array}{l} \left. \frac{\partial f(x, y, z, t)}{\partial x} \right|_{x=i\Delta x} \approx \frac{f^n\left(i + \frac{1}{2}, j, k\right) - f^n\left(i - \frac{1}{2}, j, k\right)}{\Delta x} \\ \left. \frac{\partial f(x, y, z, t)}{\partial y} \right|_{y=j\Delta y} \approx \frac{f^n\left(i, j + \frac{1}{2}, k\right) - f^n\left(i, j - \frac{1}{2}, k\right)}{\Delta y} \\ \left. \frac{\partial f(x, y, z, t)}{\partial z} \right|_{z=k\Delta z} \approx \frac{f^n\left(i, j, k + \frac{1}{2}\right) - f^n\left(i, j, k - \frac{1}{2}\right)}{\Delta z} \\ \left. \frac{\partial f(x, y, z, t)}{\partial t} \right|_{t=n\Delta t} \approx \frac{f^{n+\frac{1}{2}}(i, j, k) - f^{n-\frac{1}{2}}(i, j, k)}{\Delta t} \end{array} \right. \quad (2.8)$$

Figure 2.1 is the Yee lattice, which shows the spatial distribution of spatial nodes of discrete electric field and magnetic field and has been proved as the robust core scheme of the FDTD method. Inside the Yee cell, each magnetic field component is surrounded by four electric field components, and each electric field component is surrounded by four magnetic field components as well. This arrangement of \vec{E} and \vec{H} direction obeys both the Faraday's law of electromagnetic induction and Ampère's circuital law, which is suitable for computing the difference of Maxwell's equation. Alternate sampling between the electric field and magnetic field along the time is the core of the whole computing process; the sampling interval of the electric and magnetic field has a difference of half of the time step. Then by iteratively solving Maxwell's equation in each time step, the distribution of the electromagnetic field of the whole solving space in each moment is obtained.

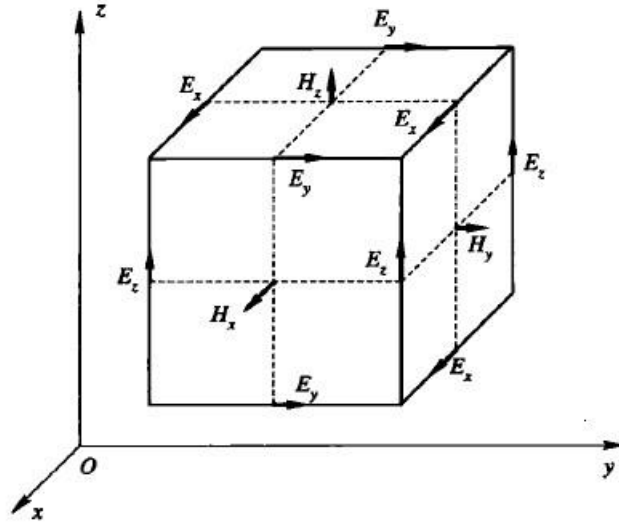


Figure 2.1 The Yee lattice and grid of FDTD methods.

The FDTD method solves Maxwell's equation via the approximation in equation 2.8. Therefore, error in each computing step is inevitable. With the increasing iterative steps and simulation time, the error will be accumulated to a value that needs to be considered. If the accumulated error from each step does not increase the total error, the simulation can be seen as stable or convergent. On the contrary, the simulation is unstable, which performs as the infinite increase of simulation results with an infinite increase of simulation time and step. The numerical stability analysis of FDTD is based on the Courant method. The stability condition of FDTD methods is given by,

$$\Delta t \leq \frac{\Delta l}{c\sqrt{N}} \quad (2.9)$$

Where Δt and Δl are time and spatial steps, respectively, N is the dimension of space. For the simulation in a 3-dimension Cartesian coordinate system, this equation is rearranged to

$$\Delta t \leq \frac{1}{c\sqrt{\frac{1}{(\Delta x)^2} + \frac{1}{(\Delta y)^2} + \frac{1}{(\Delta z)^2}}} \quad (2.10)$$

For an actual application, a high resolution of the simulation result is required for many complicate devices, which requires the high finesse of the simulation grid, in other words, the high finesse spatial step. Based on equation 2.9, a trade-off between the finesse of the time step and spatial step is crucial to ensure the convergence of the simulation. Additionally, the grid with high finesse requires enormous memory and computer computing resource, which must be addressed with various boundary conditions.

In theory, the simulation region of FDTD should be infinite. However, the simulation must be finite due to the limitation of computer memory. Therefore, a special treatment for the boundary of the simulation region is necessary. In general, the boundary of the simulation region should ensure that the wave at the boundary maintains radiation to the outer direction. In other words, no obvious reflection at the simulation boundary, and the internal spatial should have no distortion simultaneously. In 1994, Berenger proposed the perfect match layer (PML) based on Maxwell's equations as the boundary of FDTD simulation [8]. The PML is a layer of a particular medium with a wave impedance that perfectly matches the wave impedance of its neighbour medium. Therefore, the incident wave can pass through the interface of the PML without reflection. In addition, the PML is a high-absorbing medium, which could attenuate and absorb the incident wave in finite layer thickness.

In a 2-dimension Cartesian coordinate system, Maxwell's equation can be reduced as

$$\left\{ \begin{array}{l} \varepsilon_0 \frac{\partial E_x}{\partial t} = \frac{\partial H_z}{\partial y} \\ \varepsilon_0 \frac{\partial E_y}{\partial t} = -\frac{\partial H_z}{\partial x} \\ \frac{\partial E_y}{\partial x} - \frac{\partial E_x}{\partial y} = -\mu_0 \frac{\partial H_z}{\partial t} \end{array} \right. \quad (2.11)$$

The above equation is about the transverse electric wave, which only contains three components, including E_x , E_y , and H_z . Berenger mentioned that the critical point of PML is to split the magnetic field H_z into two sub-components H_{zx} and H_{zy} [8], where $H_z = H_{zx} + H_{zy}$. The equation 2.11 is then be rearranged to

$$\left\{ \begin{array}{l} \varepsilon_0 \frac{\partial E_x}{\partial t} + \sigma_x E_x = \frac{\partial (H_{zx} + H_{zy})}{\partial y} \\ \varepsilon_0 \frac{\partial E_y}{\partial t} + \sigma_y E_y = -\frac{\partial (H_{zx} + H_{zy})}{\partial x} \\ \mu_0 \frac{\partial H_{zx}}{\partial t} + \sigma_x^* H_{zx} = -\frac{\partial E_y}{\partial x} \\ \mu_0 \frac{\partial H_{zy}}{\partial t} + \sigma_y^* H_{zy} = -\frac{\partial E_x}{\partial y} \end{array} \right. , \quad (2.12)$$

where σ_x , σ_y , σ_x^* , and σ_y^* are the electric conductivity and magnetic conductivity of the medium, respectively. Equation 2.12 is a common form of the Maxwell equation, if $\sigma_x = \sigma_y = \sigma_x^* = \sigma_y^* = 0$, the equation 2.12 is degraded to the maxwell equation of free space, if $\sigma_x = \sigma_y$ and $\sigma_x^* = \sigma_y^* = 0$, it represents the conductive medium, and if $\sigma_x = \sigma_y$ and

$\sigma_x^* = \sigma_y^*$, it represents the absorbing medium. Besides, if the following conditions are satisfied.

$$\frac{\sigma_x}{\varepsilon_0} = \frac{\sigma_x^*}{\mu_0}, \quad \frac{\sigma_y}{\varepsilon_0} = \frac{\sigma_y^*}{\mu_0}, \quad (2.13)$$

The medium will have the same impedance as the free space, which means no reflection will occur when an incident wave propagates across the PML medium interface with an arbitrary incident angle, and the PML medium will eventually absorb the incident wave.

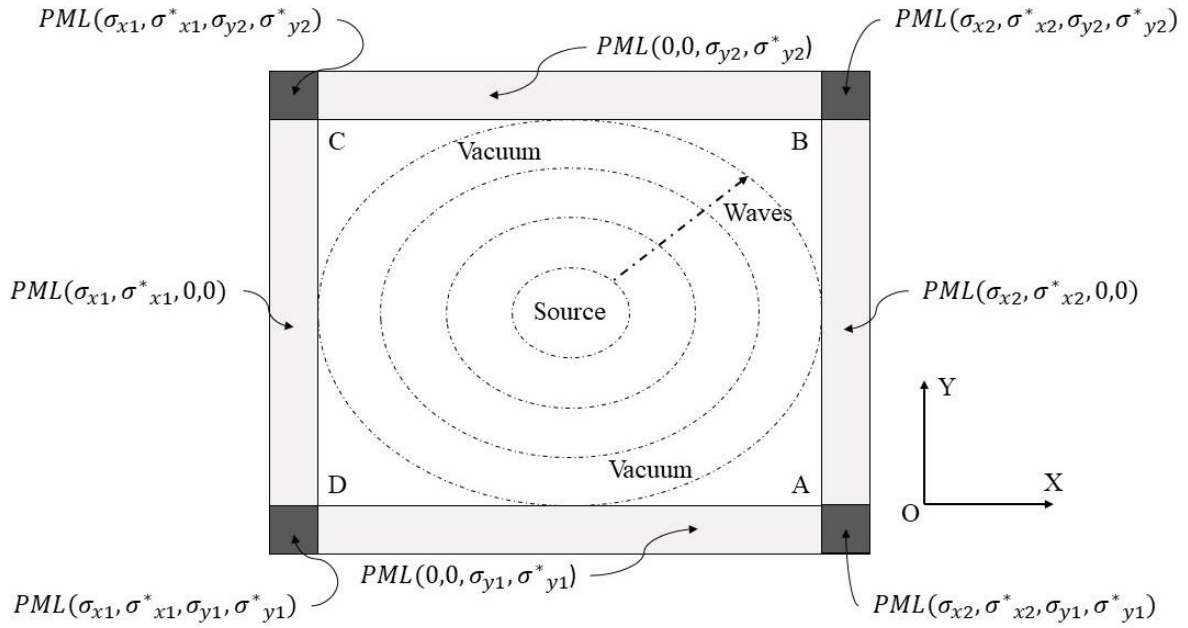


Figure 2.2 The parameters of PML boundary

Figure 2.2 illustrates the primary setting of the 2-D PML boundary surrounding an FDTD simulation region. There are two types of PML, including corner and side PML, the sides AB and CD are perpendicular to the x-axis, and their independence coefficients are set as $PML(\sigma_x, \sigma_x^*, 0, 0)$ to satisfy the impedance matching condition in equation 2.13. Correspondingly, the independence coefficients of sides BC and DA, which are perpendicular to the y-axis, are set as $PML(0, 0, \sigma_y, \sigma_y^*)$. As for the four corners area, there are set as $PML(\sigma_x, \sigma_x^*, \sigma_y, \sigma_y^*)$, which matches with side PML adjacent to it and further ensures the incident wave passes through the corner area without reflection. The PML is the most used absorbing boundary condition for FDTD simulation. Based on the requirements of the specific simulation problem, other boundary conditions are adopted, including periodic boundary, metal boundary, and symmetrical boundary [9, 10].

Another essential point of FDTD simulation is the definition of wave source. The wave sources in FDTD are generally a function of electric and magnetic components with respect to time. The wave source can be categorized as periodic and pulse source.

$$modf(n\Delta t) = \begin{cases} \sin(2\pi f_0 n\Delta t) e^{-\left[\frac{n-n_0}{n_{decay}}\right]^2} \\ e^{-\left[\frac{n-n_0}{n_{decay}}\right]^2} \sin(2\pi f_0 (n - n_0)\Delta t) \end{cases} \quad (2.14)$$

Equation 2.14 supplies three types of wave sources in FDTD, they are sine wave, Gaussian pulse, and bandpass filter Gaussian pulse, respectively, from top to bottom, in which the sine wave is a periodic source and Gaussian pulse is pulse type source, where the gaussian pulse is most adopted for FDTD since it can imitate the wideband source. Moreover, the wave source function requires different spatial rearrangements for different simulations and can be categorized as the surface source, line source, and point source.

With all these boundary conditions and source functions, the modern FDTD becomes more and more efficient and fast. Many commercial simulation software already exists in the market. All FDTD simulation in this thesis is conducted by Lumerical (Ltd.) FDTD solver.

2.3 Finite element simulation

FEM is the most used simulation method applied in numerical simulation for both engineering and academic research. R.Courant initially initialled it in 1943 to solve the problem of equilibrium and vibration via polynomial function at the multi-triangle domain [11]. The FEM then attracted the researcher of aerostructure. In 1956, engineers from Boeing illustrated a sample to solve the structure strength of an aeroplane wing with FEM [12]. The FEM was called the stiffness method by them. Then in 1960, R.W. Clough first applied FEM in civil engineering analysis [11], the first time the name FEM was used. Since then, the FEM theory has been rapidly developed and widely applied in numerical simulation of various continuous physics fields. With the development of modern computer science, the massive computing process in FEM is implemented by computers, which enhances the development of FEM a lot.

The two critical points of FEM are solving the partial derivative equations (PDE) and discretization. Various physics fields can be reformatted to a PDE by the functional method. The available minimum corresponds to the governing PDE and given boundary conditions. Therefore, the physics filed equation is transferred to a PDE. Then various simplified

variational solving methods are applied to solve the approximate numerical solution, for example, the strong form Galerkin method, the weak form Galerkin method, and the Rayleigh-Ritz method. Among these methods, the PDE is substituted by an approximate function to acquire the solution. Discretization, specifically, is a process that splits the continuous medium into various basic geometrical elements, usually called meshing. The physics field solution on whole simulation domain is obtained by assembling the PDE solution of each element. Unlike the FDTD, the FEM has more choices for meshing, including tetrahedrons, hexahedrons, and polyhedrons meshing. Figure 2.3 illustrates those three different meshing types. With various meshing schemes, the FEM is more suitable for simulating complicated structures.

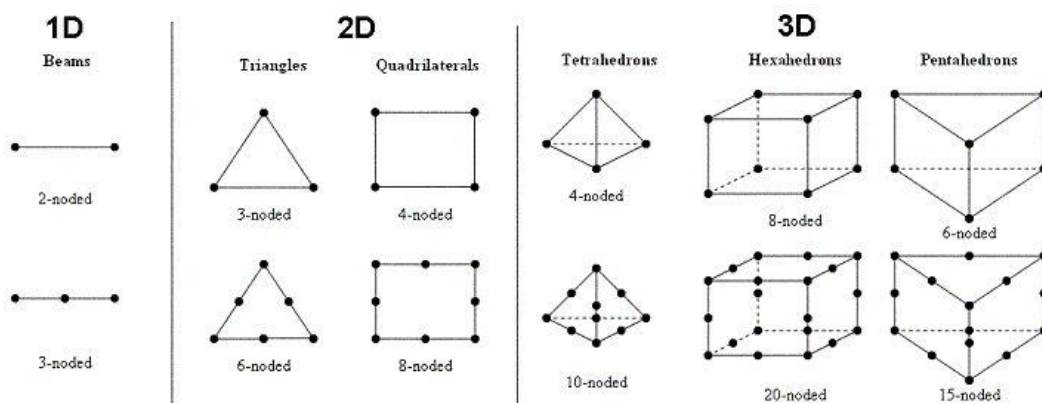


Figure 2.3 The meshing of FEM.

The core of the electromagnetic simulation is solving Maxwell's equations at a given boundary condition, which is applicable to use the FEM methods. There are three main steps for solving the EM model by FEM methods: pre-processing, solving, and post-processing. Pre-processing, including identifying solving regions, building mathematic models, and region meshing, depended on the requirements of different objects and devices. With proper PDE and boundary conditions, the solving process is then executed. During post-processing, the simulation results are analysed.

Like the FDTD method, selecting appropriate boundary conditions is vital for FEM simulation. Open space simulation is only the ideal occasion. The computer is not able to solve the EM field in infinite space. Therefore, the FEM simulation region should be confined to a limited region depending on the computer's hardware. PML boundary, as a widely used boundary condition, is also compatible with FEM simulation. Like the FDTD simulation, PML in FEM also matches with the impedance of neighbouring medium and boundary conditions, which could absorb the incident wave to eliminate influence on the result from reflection.

The advantage of FEM is its high applicability thanks to its flexibility and various mesh schemes. However, the universal approximation methods for PDE solution in FEM simulation consume more resources than FDTD, as the two main simulation tools, FDTD and FEM, are adopted for different devices design in this thesis. The FEM solver employed is the Comsol Multiphysics.

2.4 Other numerical simulation methods

Despite the two main electro-magnetic simulation methods adopted in this thesis, there are various simulation methods that suitable for different scenario and problem, for example, the Transfer matrix method (TMM) [13], Methods of lines (MOL) [14], Rigorous coupled wave analysis (RCWA) [15], Beam propagation method (BPM) [16], and Boundary element method (BEM) [17] etc.

All these simulation methods adopt whether integral algorithm or differential algorithm. The integral algorithm considers every node and cell and solves the matrix in the whole simulation region without being limited by boundary conditions, and it is a compact matrix. The grid of this type of algorithm uses an unstructured surface to divide the grid, mainly used For Fourier space analysis, it is an efficient semi-analytic broadband algorithm, but it is prone to convergence problems. The full-wave integration algorithm generally includes BEM and BPM which has determined the vector characteristics of the electromagnetic field. These simulation methods are limited to be used for 2.5D layered structures with acceptable accuracy.

Whether the differential algorithm only calculates the points in the local region and the matrix in the adjacent area. Due to the boundary conditions, the grid of this type of algorithm uses a structured body to divide the grid, which is mainly used for real space analysis. But this algorithm is relatively easier to converge. The differential algorithm includes FDTD, FEM, MOL, and RCWA, which describes infinite grids into finite grids through convergence conditions and is used in most high-precision 3D full-wave analysis electromagnetic software of arbitrary structures.

Here the Table 2.1 briefly summarized the basic principle of these simulation methods and compare their advantages and disadvantages.

Table 2.1 Comparison among different simulation methods

Simulation method	Basic principle	Advantages	Disadvantages
TMM	Calculating the energy propagation in homogeneous material layer and between interface	High efficiency, Accurate, no stability issue, arbitrary layer thickness, ease for periodic repetition	Limited applicability for only linear homogeneous model, unsuitable for diffraction simulation
BPM	Calculating the in-plane forward energy propagation without considering the reflection	Applicable for non-linear material, considering material dispersity, suitable for waveguide analysis	Limited accuracy, ignored reflection
MOL	Numerical calculation only in the X-Y direction, and analytical expanding to Z axis. Analysing the mutation between each conductor and medium	Suitable for periodic structure expanding in Z axis, rigorous solution, suitable for resonance analysis	Poor convergency on propagating direction, lower efficiency than RCWA in medium analysis
RCWA	Numerical calculation only in the X-Y direction, and analytical expanding to Z axis. Analysing each spatial harmonic wave and adopting plane wave as incident with arbitrary angle	Very suitable for periodic structure expanding in Z axis and diffraction analysis for large scale device, high accuracy, no stability issue	Poor convergency on propagating direction, poor efficiency for device with high permittivity and metal, inapplicable for finite structure
BEM	Solving the governing equations in regions	Suitable for curved surface or structure with low surface area	Limited accuracy for complicate structure,

	with deterministic boundary conditions	to volume ratio, scalable with FEM simulation, no stability issue	non-rigorous algorithm
FDTD	Chapter 2.2	Suitable for large scale parallel calculation in time-domain, very high accuracy, intuitive calculation, applicable for non-linear analysis, ease for virtualization, suitable for broadband analysis	Low efficiency for curved surface due to Yee mesh, complicate dispersive analysis
FEM	Chapter 2.3	Most mature and commercial algorithm, applicable for arbitrary structure	Complicate mesh taking enormous simulation resource

By comparing these simulation methods, the FDTD and FEM methods are more universal than other simulation methods, therefore they are adopted as the main simulation tools for this thesis.

Chapter 3

Study of Active Devices – OLEDs

This chapter studies the enhancement of efficiency by nanostructure for active devices, namely the OLEDs. The simulation works in this chapter are all set with active dipole source. Based on comprehensive numerical simulation and optimization, a metal grating structure and an index grating structure are proposed to enhance the light extraction of OLEDs.

Disclaimer

Part of the result and content in this chapter is already published in a journal paper [18] and a conference proceeding [19]. The author of this thesis is also the first author of those two publications. The publisher has authorised the permission to reuse for academic purposes and the creation of derivative works.

3.1 Introduction

3.1.1 Optical losses of conventional OLED

Optical sources are a prominent proportion of active devices. Organic light emitting diodes (OLEDs), invented in 1987 [20], as a new generation of flat-panel display and all-solid-state lighting technology, have been extensively developed in the last three decades. OLEDs attracts researchers' interest due to their intrinsic characteristics, including high brightness, beneficial emission characteristic, lower cost and power consumption. Nowadays, OLEDs have been successfully commercially applied in various commercial display devices, for example, smartphones, PC monitors, and televisions. Most of the research about OLED focus on materials design and synthesis of the organic emitting layer. With the evolution of organic photoluminescent material, the internal quantum efficiency of OLEDs has been significantly improved to nearly 100% utilizing phosphorescent material [21]. However, the optical out-coupling efficiency still confines the overall efficiency of OLEDs. Three factors mainly cause the optical losses in OLEDs, namely, the total internal reflection (TIR) between each layer,

Surface Plasma Polariton (SPP) on the metal-organic interface, and optical blockage due to the driven circuit.

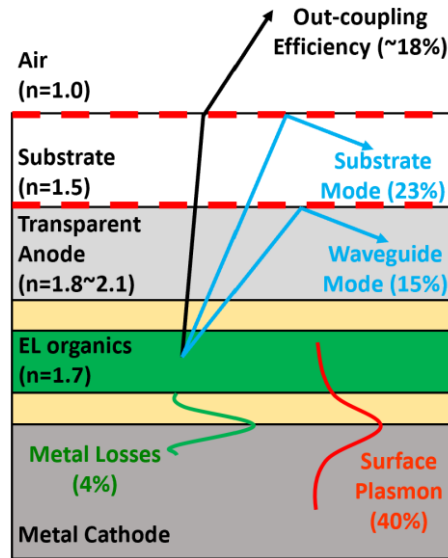


Figure 3.1 Optical losses of conventional OLEDs

In general, OLED is a multi-layer optical structure with two electrodes on the top and bottom, respectively. Figure 3.1 shows the structure of conventional OLEDs, cathode, organic layers, emitting layer (EL), and anode from the bottom to the top. Light is generated in the EL and emitted around. Due to the TIR caused by the mismatch of refractive index between each layer, the guided mode is generated. Usually, guided mode happens on the electrode-substrate and the substrate-air interfaces since the light propagates from the high index layer to the low index layer, which leads to TIR according to Snell's Law. Around 40% of the generated light energy is taken by the substrate and waveguide modes and finally absorbed. Besides, another 40% of generated light energy is converted to surface plasmon mode and eventually absorbed by the medium. The interaction between free electrons on the metal surface and incident photons generates SPP, an evanescent wave propagating through the surface of the metal layer. With all these optical losses, nearly 20% of the generated light energy is outcoupled from the substrate.

Several approaches have been proposed and verified to eliminate those optical losses and enhance OLED's light extraction efficiency (LEE). Typically, scattering structure is one of the main methods to enhance the optical extraction of OLEDs by recovering the energy absorbed by substrate mode. The first scattering structure is reported by T. Yamasaki to increase the efficiency of OLEDs in 2000 [22]. Since then, various designs have been presented to eliminate optical losses. The micro-lens array [23-27] and scattering layer [28-30] are adopted as external

structures attached to the surface substrate to decrease the substrate loss. Similarly, Periodic structures, including diffraction grating [31, 32], conjugate structures[33], photonic crystals [34], and low-index grids [35-38], are utilized to recover the losses mainly caused by waveguide mode and SPP inside the multi-layer structure of OLEDs. In addition, the microcavity effect can improve the overall LEE of OLEDs [39], as well as a gradient refractive index (GRIN) substrate, which can adjust the ratio of the light-waveguided modes [40]. All those structures mentioned rely on precisely sub-wavelength level nanophotonic design to control OLEDs' out-coupling.

3.1.2 Limitation of conventional bottom-emitting OLED

Another problem for LEE is the blockage by the driven circuit, which generally involves many thin-film transistors and capacitors integrated into the substrate. Most OLEDs adopted the conventional structure shown in Figure 3.1, namely the bottom-emitting OLEDs (BEOLEDs), in this case, light outputs from the substrate side, where the driven circuit reduces the aperture ratio for out-coupling. In order to increase the aperture ratio of OLEDs and avoid that blockage, the structure of Top-emitting organic light-emitting diodes (TEOLEDs) is proposed.

Most of the conventional OLEDs employed a bottom-emitting layout because they were aimed at the large-scale device, for example, television, where the blockage area of the driven circuit is far less than a single pixel area. However, with the explosive demand for high-resolution tiny-scale displays on mobile devices, including smartphones, tablets, and laptops, the blockage of the circuit becomes a big problem for their small pixel area. Therefore, to avoid the blockage from the driven circuit in the substrate, the top-emitting structure is proposed, where the light outputs from the non-substrate side. Figure 3.2 illustrates the structure of bottom and top emission OLEDs, respectively. The semi-transparent anode is the crucial point of TEOLEDs. The early-stage TEOLEDs adopt transparent conductive metal oxides (TCOs) as an electrode at the emitting side; for instance, Indium Tin Oxide (ITO) [41], Aluminium Zinc Oxide (AZO) [42] and Indium Zinc Oxide (IZO) [43], which was widely used as the anode of BEOLEDs. TCOs are commonly coated on a glass substrate for obtaining a homogenous thin film by sputtering, compatible with the fabrication process of BEOLEDs. However, for TEOLEDs, the sputtering process will inevitably damage the organic layer, which is more unstable than the glass substrate, and further deteriorate the performance of the whole device. Although a buffer layer between the organic layer and anode could protect the organic layer

during sputtering, it could introduce more guided mode losses due to an extra layer with a mismatched index.

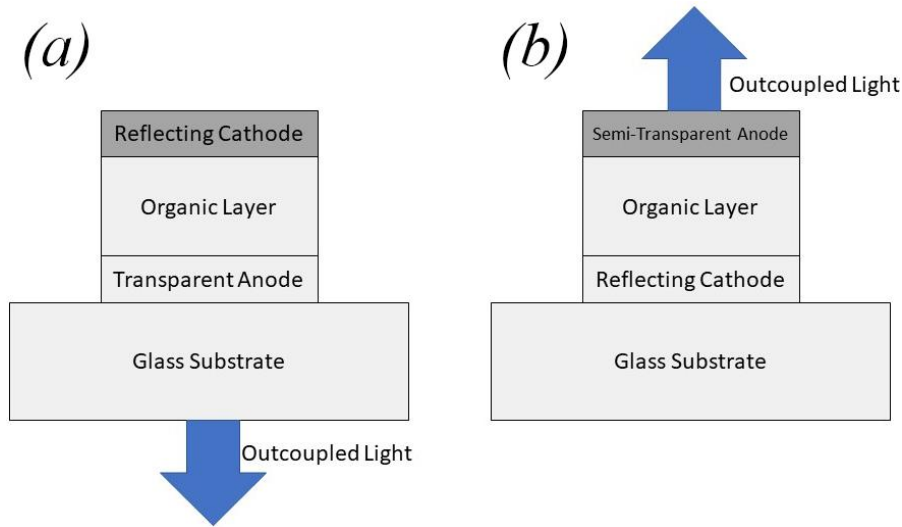


Figure 3.2 Structure of (a) Bottom-emitting and (b) Top-emitting OLED.

Due to the limitations of TCOs' application on TEOLEDs, ultra-thin metal film electrode was considered a promising candidate because metal can be coated by evaporating, which is less harmful to the organic layer. Metal electrode typically represents cathodes in OLEDs. The most straightforward solution is to make the metal cathode thinner for transparency. Most electrode metal is semi-transparent below 20 nanometres, but ultra-thin metal film could decrease conductivity dramatically [44], making the trade-off between transparency and conductivity the critical point of TEOLEDs design. Besides, since the reflectivity of Aluminium, the most used cathodes material, is too high, several dual metal electrodes TOLEDs, in other words, both cathode and anodes made by metal are proposed, and the light is supposed to output from the semi-transparent metal anode side. Ag was adopted as the anode for the mentioned type TEOLEDs thanks to its low working function, which achieves a decent balance between the electric and photonic performance of whole devices [45]. However, dual metal electrode design introduces extra SPPs loss on the interface between the metal anode and organic layer [46]. Besides, micro-cavity effects caused by the double metal electrodes [47] also influence the performance of TEOLEDs [25, 26, 48]. Nanostructure on Ag anode has been reported to eliminate these losses [49].

3.1.3 Limitation of the light extraction of polarized OLED

Most research on OLEDs has been focused on unpolarized emissions. The polarized OLED is the prominent next-generation light source of liquid crystal displays (LCDs) backlight

and three-dimensional display systems. Since Dyreklev et al. first reported directly producing linear polarized emissions by adopting aligned polymer film in 1995 [50], alignment of the emissive layer based on luminescent liquid crystal material in OLEDs became the critical point for achieving highly polarized emission and attracted more interest. Various approaches have been developed to produce an aligned emitting layer, such as an electrostatic field generated by mechanical friction [50, 51], Langmuir-Blodgett (LB) deposition technique [52] and application of self-organization properties of liquid crystal material [53]. Rod-like uniaxial molecules, such as oligofluorene, thiophene and oxadiazole derivatives, typically composite the aligned emitting layer. Most rod-like molecules' transition dipole moments are along their long axis [54]. Thus, high effective polarized emission can be achieved by orderly orienting these molecules.

Although incorporating aligned material in the emitting layer does implement polarized emission, the anisotropy of the optical constants of the emitting layer is correspondingly changed due to its high relevance to the orientation of molecules [54]. More specifically, the in-plane ordinary refractive index is raised, which increases the optical loss due to the transverse electric (TE) mode and further influences the optical extraction efficiency of the whole device. However, the molecule orientation-dependent anisotropy makes it feasible to manipulate an emitting layer's refractive index and enhance extraction efficiency. Previous work has reported outcoupling characteristic modifying of OLEDs by modulating the refractive index to form a refractive index pattern [55]. Logically, the precise alignment methods and appropriate optical structure design became two main challenges for high-efficiency polarized OLEDs.

3.2 The target of this chapter

This chapter is aiming for enhancing the light extraction of both conventional OLEDs and polarised OLEDs.

Firstly, for improving the performance of conventional OLEDs, a top-emitting structure with metallic grating anode at the emitting side is adopted, an optimized structure is proposed basing on the optimization and simulation.

Another part of this chapter looks at enhancing the light extraction of polarised OLEDs, a novel luminescent liquid crystal material is adopted as the emission material. Simulation work

is proposed to investigate the best index grating profile and device structure to improve both the light extraction and polarized ratio of the polarized OLEDs by eliminating the guided mode losses in such devices.

3.3 Design and simulation of TEOLED with metallic grating anode

3.3.1 Simulation model and mode analysis

A TEOLED structure with a metallic nano grating anode is proposed in this chapter, with a discussion based on simulation results adopting Finite Elements methods (FEM) and Finite difference time domain (FDTD). The basic structure of the BEOLED contains a cathode, anode and organic layers between the two cathodes, including the electron transport layer (ETL), emissive layer (EML) and hole transport layer (HTL). As mentioned before, the typical anode material for BEOLED is ITO, and the material of EML adopted in this report is Al/Aluminum 8-hydroxyquinoline (Alq3) which has an emission peak of around 528 nm. The HTL is set as N, N -bis(naphthalene-1-yl)-N, N-bis(phenyl) benzidine (NPB). Additionally, the cathode material is Al due to its high working function. The simulation model does not consider the ETL since it has a similar refractive index with the neighbouring organic layer. Geometrically, the conventional BEOLED structure employed for comparison is AL/Alq3/NPB/ITO/GLASS, and their corresponding thickness is 600 nm, 60 nm, 60 nm, 100 nm and 3000 nm, respectively.

By taking advantage of the Extraordinary optical transmission (EOT) phenomenon, a novel design of TEOLED by replacing the conventional ITO anode with a plasmonic metallic grating is proposed. For this TEOLED structure, the Al cathode is attached to the glass substrate. Ag is adopted for the anode material due to its relevantly high conductivity and good transparency at the nanofilm state. As shown in Figure 3.3, the entire structure of TEOLED is Glass/AL/Alq3/NPB/Ag. The thickness of EML and ETL were both decided to be 60 nm. The thickness of cathode AL is 600 nm. This structure is equivalent to a microcavity structure with two metal cavity reflectors, where one reflector is Ag thin film with nano grating. The SPP exists at the Ag/NPB interface and Al/Alq3 interface. Approaches have been attempted to recover the SPP mode's energy at the Al cathode. Leiming Wang et al. have proposed a structure to reduce the SPP on the cathode/organic interface [56]. On the contrary, this design mainly concerns reducing losses caused by the SPP on the anode and the micro-cavity effects.

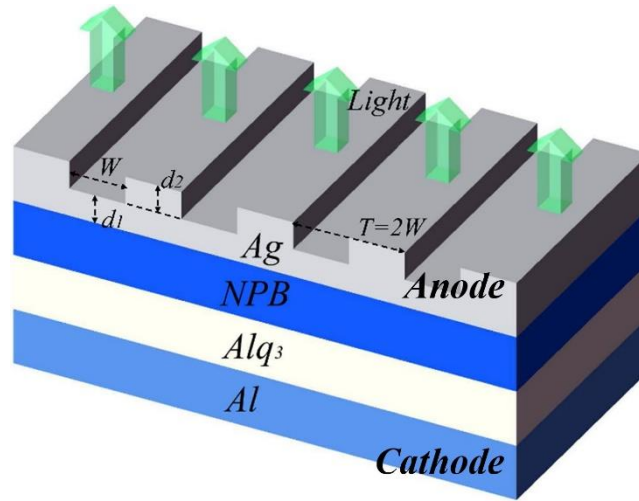


Figure 3.3 Illustration of the proposed TEOLED structure with Ag nano-grating anode.

The spontaneous emission of OLED is referred to as vertical and horizontal dipoles placed in homogeneous and isotropic EML [57]. For simplicity, the dipole was placed on the interface between the Alq3 and NPB layers.

Figure 3.4 shows the normalized near-field distribution and normalized intensity of the TOLED with 20 nm thickness flat Ag film anode (a)(c) and grating Ag anode (b)(d), respectively calculated by 2D FEM simulation carried out in Comsol multi-physics. The top and double side boundaries are set as PML to avoid the deviation caused by reflection. The Al cathode represents a reflection mirror and has enough thickness to prevent the light output from the bottom side. Especially for the grating anode model, the grating constant W is set as 300 nm close to a half wavelength of the emission peak of EML material, and the thickness of Ag film d_1 and grating d_2 are 5 nm and 30 nm, respectively.

SPP mode is observed on both the Air/Ag and Ag/NPB interface in Figure 3.4(a). The dipole source's near-field emission interacts with the Ag film's inner surface, generating the SPP at the Ag/NPB interface as seen as a periodic semi-spheric pattern on the interface. SPP mode also appears at Air/Ag interface because semi-transparency of thin Ag film. In addition, due to the micro-cavity formed by relevant high reflective Ag film and Al cathode, a tiny part of waveguide mode is also generated in the organic layer, which leads to another part of energy loss.

As a comparison, Figure 3.4(b) shows that SPP on both Air/Ag and Ag/NPB interfaces are significantly reduced. Most of the SPP mode is recovered. The waveguide mode of the organic layer is also reduced because the grating structure changes the Ag anode's effective

reflectivity. These mode profile analyses prove the potential of nano-grating to enhance the LEE of TEOLED. The intensity patterns also show a similar trend as can be seen in Figure 3.4(c) and (d), a strong SPP wave is observed at both sides of Ag anode layer in Figure 3.4(c). With grating applied, an obvious outcoupling wave is seen in Figure 3.4(d).

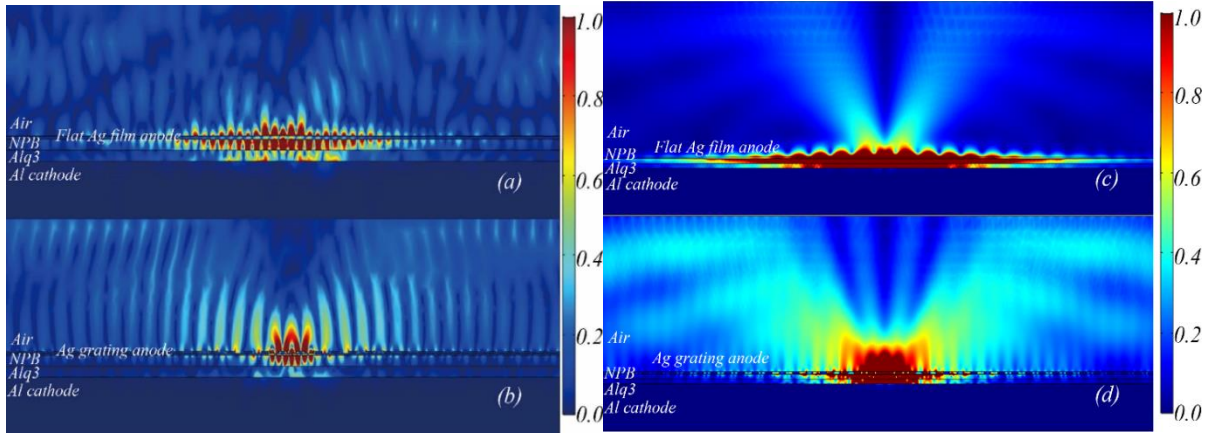


Figure 3.4 The 2D FEM simulated normalized field distribution E of TEOLED. (a) with flat Ag film anode (b) with Ag nanograting anode. The normalized intensity (E^2) of TEOLED (c) with flat Ag film anode (d) with Ag nanograting anode.

3.3.2 optimization of the design of metallic grating anode

The FDTD simulation is implemented to sweep the gratings period to optimise the design. Figure 3.5 shows the emission spectrum of OLEDs obtained by FDTD simulation. For the simulation model, a dipole source is placed at the centre of Alq3 layer for representing the emission, a 2D monitor is placed in the air region, the extraction efficiency is derived by the energy received by the monitor normalized to the dipole energy. The red line is the conventional BEOLED model, as mentioned above. Its efficiency is low because of the significant refractive index difference between the ITO and glass, which suggests most of the generated light energy is trapped in the ITO and organic layers [47]. The black curve represents the spectrum of TEOLED with a flat Ag anode as a comparison for the grating anode. By converting the bottom-emitting to top-emitting structure with replacing the ITO/glass layers with a thin silver film, the emissivity is seen as a significant enhancement, which is almost two times higher than the conventional OLED at the wavelength of 600 nm.

The extraction efficiency can be further increased by etching periodic structures on the silver layer surface. For the grating profile, the different d_2 represents the different etching depths, the thickness of the bottom layer of Ag d_1 is 5 nm as a trade-off between transparency and conductivity. Figure 3.5 (a) shows the spectra of different etching depths of grating with same periods, the 30 nm etching depth shows relatively good overall intensity, chosen as the

optimized values for the following period sweeping. In Figure 3.5 (b), the rest of the curves are the normalized emission spectra of the nano-grating anode with different periods. The intensity can be remarkably enhanced in different wavebands with different periods. When the period is 300 nm, it has two emission peaks at 500 nm and 575 nm in several. When the period is 500 nm, the peak is 528 nm. FDTD simulations of this structure indicate a potential 60% increase in the normalized emissivity over that of a conventional BEOLED in some particular wavelength. Generally, this grating with a period at 500 nm and 600 nm is better than others.

Additionally, the spectrum of all the grating structures has two peaks except the grating with a 500nm period. The peaks on the left are relatively stable compared to those on the right. The left side peaks are caused by the microcavity of the whole TEOLED structure depending on the depth between the cathode and anode, which is constant. Therefore, the left side peaks are stable around 520nm. For the ridges on the right, with the changing of the grating period from 300nm to 500nm, a blue shift trend is found, and then the right-side peaks' central wavelength experiences a redshift trend along the period changing from 500nm to 700nm. The right-hand peak fluctuates remarkably within the changing of the grating period. The emission spectrum of the grating period at 500nm can be taken as the best design. The two peaks overlap at 510nm, reflecting good monochromaticity and benefits for the OLED display performance.

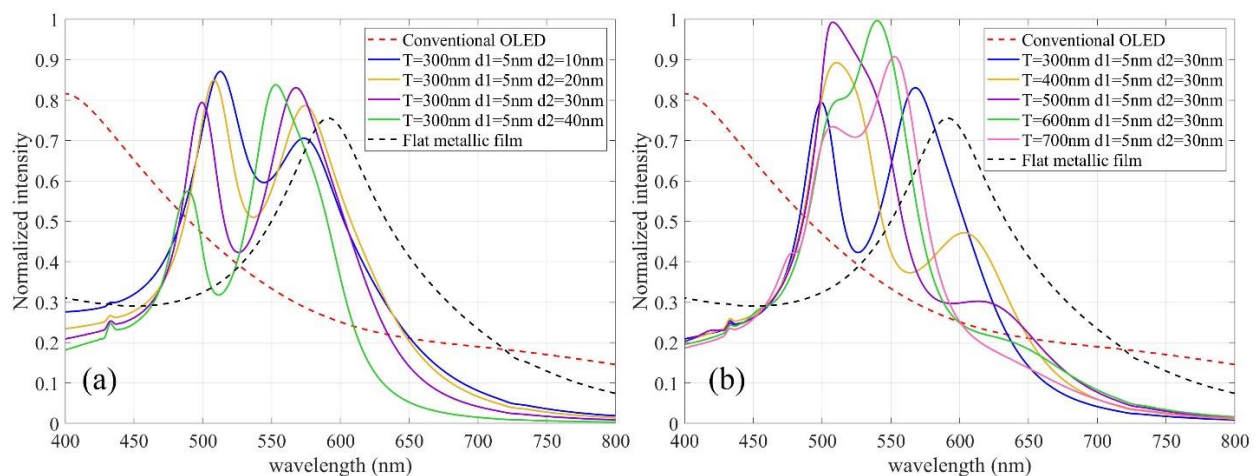


Figure 3.5 Emission spectra of normalized intensity with wavelength (a) for the different grating depth, (b) for the different grating periods.

Furthermore, the emission angle determines the visual angle of OLED devices, an essential feature for OLEDs as display devices. The emission spectrum's normalized far field angle profile is calculated by FDTD and shown in Figure 3.6. The blue curve shows the angular response of TEOLED with flat Ag film, which is relevantly low and distributes as Lambert emission. As shown with the red curve, the Ag nano-grating structure's efficiency is enhanced

conspicuously. The grating period is chosen as $T=500$ nm according to the optimization result in Figure 3.5 (b). Generally, its spectrum is shown as Lambert emission, but it has two little peaks at a symmetrical angle due to the grating dispersion. The two peaks also match the previous result. In Figure 3.4 (d), the normalized intensity distribution figure shows emission enhancement in a specific angle symmetrically as well. The black curve is the emission angle distribution of the conventional BEOLED. The emission energy of the Ag grating structure is significantly better than both BEOLED and TEOLED with a flat Ag film anode. The design of TEOLED with metallic grating anode possesses a broad angle response and higher emission intensity. These two properties make the proposed metallic grating-assisted structure promising for practical applications.

It is worth mentioning that the periodic grating thickness is smaller than the total silver anode thickness. Both of them are mentioned earlier as d_1 and d_2 . The thickness of the silver layer can guarantee the anode with excellent electric performance.

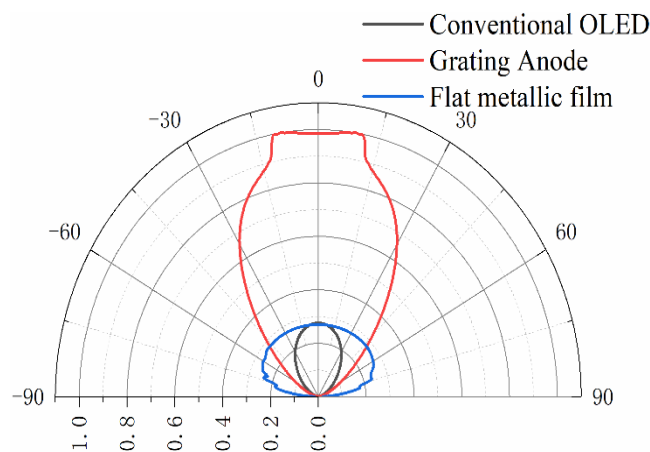


Figure 3.6 The emission angular responses obtained by FDTD simulation.

3.4 Design and simulation for enhancing light extraction of polarized OLEDs

This section proposes a simulation-based design of enhanced light extraction polarized OLED devices with a periodic index difference nanostructure based on refractive index manipulation, which is feasible by utilizing photoalignment luminescent liquid crystal [58]. The photoalignment luminescent LC is achieved by compounding photoalignment moiety at both ends of the chain of the emissive small-molecules with rod-like shape, and the

photoalignment moiety will crosslink to each other under ultraviolet (UV) exposure, which forces the long axis of the molecules to align uniformly. Therefore, periodic refractive index changed nano-pattern can be precisely produced and controlled by exposing the material to a UV interference pattern [58]. By introducing the refractive index grating, the External Quantum Efficiency (EQE) of the devices is enhanced up to 56% with preferable geometric parameters at 550 nm emission wavelength. Furthermore, a structured design with an extra uniformly aligned layer is proposed and researched to improve the polarized ratio to 28 dB under the premise that the EQE has been enhanced via refractive index grating. Detailed analysis indicates that TE and transverse magnetic (TM) mode losses are recovered and outcoupled via the refractive index grating while the grating modulates the polarization characteristic.

3.4.1 Luminescent liquid crystal for the emission layer

A Luminescent liquid crystal material based on BDAVBi molecules is adopted for the emission layer of this design, which is a patented organic material concept initialled by the co-operator company of this project, Lomox Ltd [58]. The orientation of the molecules inside the emission layer profoundly influences the refractive index, conductivity, and emitting polarizability. This section introduces the scheme of molecule alignment based on the potential structures of proposed LC molecules first and then discusses the influences of the orientation of molecules on the optical and electrical properties of luminescent LC materials.

The Aggregation-induced emission (AIE) liquid crystal molecules were synthesized successfully using AIE as core chromophores for the luminescent liquid crystal [59, 60]. Typically, (E)-stilbene core materials have been commercially applied in OLEDs as a passive polarized filter[61]. 4,4'-[4,4'-Biphenyldiyl]di(E)-2,1-ethendiyl]bis(N, N-diphenylanilin) (BDAVBi), one of the (E)-stilbene derivatives, is also widely developed as core chromophores [61] and can be employed as the emission core of LC molecules. Figure 3.7 shows the proposed one of the potential LC's molecular structures based on the BDAVBi core. The BDAVBi core at the centre supplies the emission function of whole molecules.

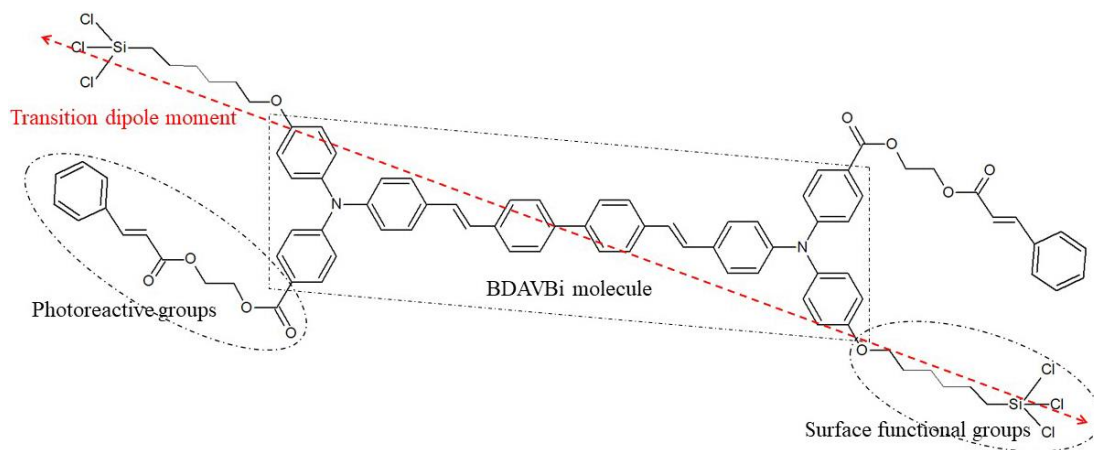


Figure 3.7 Potential molecule structure of EML material (BDAVBi derivation) used in the manuscript.

The molecule shown in Figure 3.7 possesses a rod-like shape spatially. For a rod-like molecule, its transition dipole moment generally coincides with its long molecule axis [54], in which the molecule's orientation dominates the direction of the electric field vector during emission. The aligned emission film is proven to achieve emission with a high polarized ratio. In 1995, Dyreklev et al. performed oriented substituted polythiophene for light emission with a polarized ratio up to 60:1 [50]. They suggested that the electronic properties of conjugated polymers are governed by the delocalized π -electron system. Alignment of the polymer chain will perform an electronically anisotropic material since the dipole transitions are oriented along the main chain direction. Optical absorption and photoluminescence will be stronger parallel to the orientation direction simultaneously [50]. The transition dipole moment from S_0 (ground state) to S_1 (lowest singlet excited state) is known to be predominantly oriented along the long axis of the molecule, along the system series of pi-conjugated bonds [62]. Therefore, the effective dipole emitters in organic film with all molecules in same orientation are aligned along the same direction as the long axis of molecules.

If all the molecules in the EML can be perfectly aligned in the same direction, linearly polarized emission can be achieved. The Photo-crosslinking and photo-alignment material had already been synthesized and demonstrated [63], where a photoreactive group is employed for achieving those functions. The photoreactive group adopted for this design is cinnamate ester, which has been tested as the photo cross-linkable end group for liquid crystal to achieve photoalignment [58, 64] and can also be used as the mesogenic unit for luminescent liquid crystal materials [65, 66]. As seen in Figure 3.7, photoreactive end groups are bonded at both ends of BDAVBi molecules. Therefore, the orientation of proposed luminescent liquid crystal molecules can be manipulated by an external electric field, for example, an electrostatic field

or an incident light wave. Besides, the promising liquid crystal molecule is not only photo-alignment available, but also photo cross-linkable, which means the photoreactive group will react with the same group on neighbouring molecules when exposed to linearly polarized ultraviolet (UV) light. Hence, a crystallized emission layer with aligned molecules can be fabricated[67]. As shown in Figure 3.8, the molecules in the emission layer are all in-plane aligned in the same direction.

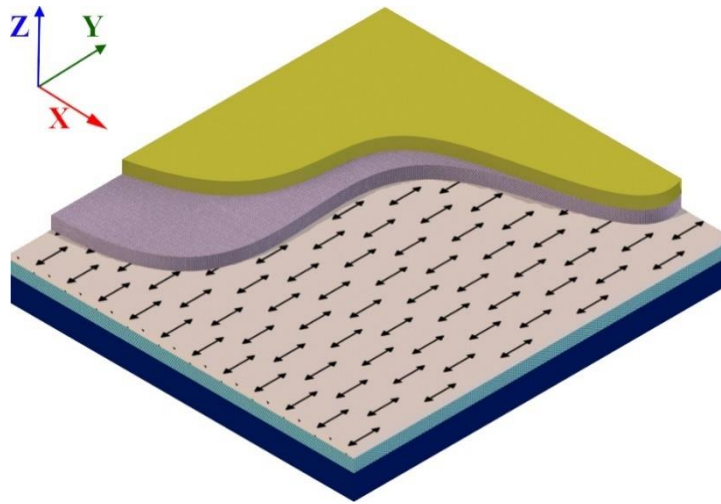


Figure 3.8 Model of the polarized OLED with crystallized EML.

However, the alignment leads to anisotropy in the optical constant. In the case of molecules with rod-like shapes, their molecular polarizability along the long axis is significantly larger than in the other directions. This is because the electrons moving inside an organic molecule is easier than between the molecules, which results in anisotropy in molecular polarizability [20]. Therefore, a high birefringence can be achieved in perfectly horizontally aligned EML. Notably, in this homogenous aligned EML, the refractive index component in the y-axis, n_y , is significantly enhanced because the long molecular axes are oriented in the y direction. Although the in-plane oriented (aligned) BDAVBi material has not been reported, for liquid crystal molecules, the in-plane alignment is not difficult to achieve [67, 68]. As mentioned, the EML material adopted is a luminescent liquid crystal based on BDAVBi derivation. This liquid crystal material's in-plane alignment is achievable by exposure to particular linearly polarized UV lights, also known as photoalignment [67, 69]. Besides, in 2002, researchers from Hull university proved that the quantum efficiency of photoluminescence of fluorene-based luminescent moiety is increased by cross-linking caused by compounding the photoreactive end groups [63], so the emission of BDAVBi core is supposed not be influenced significantly after compounding those end groups.

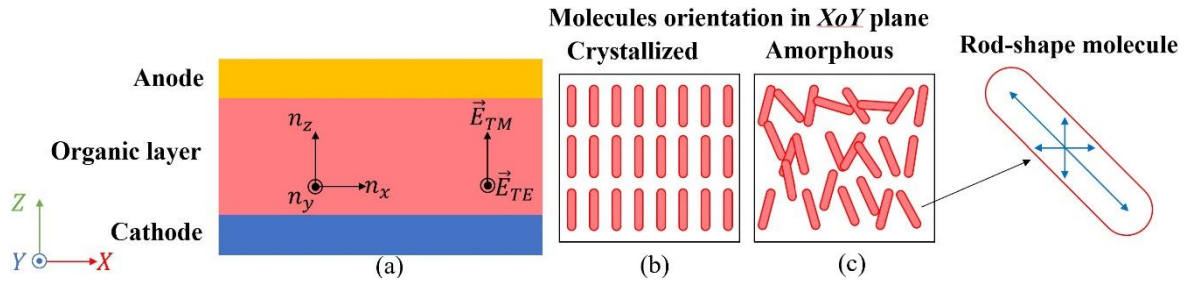


Figure 3.9 (a) 2D structure of OLEDs (XoZ plane), (b) Aligned rod-like shape molecules in the plane of EML from the top view(XoY plane), (c) Randomly distributed rod-like shape molecules in the plane of amorphous EML from the top view(XoY plane).

The orientation of molecules also influences the conductivity of the whole EML layer. First, improving the degree of molecular orientation can promote a considerable overlap of the wavefunction of π -orbitals among π -conjugated molecules, which is a promising method for achieving high charge-carrier mobility [70]. Therefore, the maximum conductivity is achieved with perfect alignment of the EML layer; in other words, all molecules are in the same direction. In summary, highly aligned molecules lead to both higher conductivity and highly polarized emission. Since this research mainly concerns optical properties, the conductivities for different orientation statuses are assumed to be the same to simplify the simulation.

3.4.1 Losses mode analysis of polarized OLEDs based on luminescent Liquid Crystal

Because of the anisotropy index of luminescent LC material due to the structure and orientation of its molecules, the polarized OLEDs based on it may have different optical loss compared to conventional OLEDs (Figure 3.1). This section analysis the optical losses of polarized OLED by numerical simulation. Figure 3.10 (a) and (b) illustrate the OLED simulation model with amorphous and crystallized EML, respectively. From the top to the bottom of the structure, a 100 nm ITO layer represents the anode, 60 nm α -NPD is adopted as hole transport layer (HTL), 100 nm LC material is EML, 60 nm Alq3 is the electron transport layer (ETL), and 300 nm Aluminium is the reflective cathode for the devices. The refractive index of the EML material, luminescent LC based on BDAVBi, has never been measured. However, the indices of aligned BDAVBi film were reported with strong anisotropy[71], and Yokoyoma et al. have investigated the anisotropy refractive index of BDAVBi at crystallized status [72]. The adopted refractive index of EML for the simulation is fixed. The values are $n_y \approx 2.4$, $n_x = n_z \approx 1.8$, which is the value around the most prominent point on the index spectrum in for n_o and n_e , respectively from Yokoyama's result. The refractive index Yokoyama tested is from BDAVBi film with molecules oriented in the horizontal direction.

More specifically, the long molecular axis of each molecule is in the substrate plane without alignment. Therefore the film they tested is negative birefringence. The EML material for this design is a liquid crystal (BDAVBi derivation) which can be homogeneous aligned along the Y axis (in the plane) as mentioned. Because the long molecular axes of all molecules in EML are oriented in the Y axis (homogeneous alignment), the n_y of our LC should not be less than the n_o Yokoyama tested. Besides, Yokoyama et al. proved that longer molecular length leads to more significant anisotropy in their previous work [73]. The proposed LC molecules have a longer main chain than BDAVBi core molecules, which means higher birefringence. Therefore, the largest value of the refractive index tested by Yokoyama is adopted for simulation. Besides, the refractive index at amorphous status can be calculated by the following equation.

$$n_{iso} = \sqrt{\frac{2n_e^2 + n_o^2}{3}} \quad (3.1)$$

Where n_e and n_o are the extraordinary and ordinary refractive indices, respectively. The refractive indices and the thickness of each layer we used in the simulation are shown in Table 3.1.

Table 3.1 Refractive indices and the thickness of each layer

layers	Material	Thickness	refractive index
substrate	Glass	3000 nm	1.5
anode	ITO	100 nm	1.8
HTL	α -NPD	60 nm	1.78
EML	LC Material (BDAVBi derivation)	50~150 nm	$n_y \approx 2.4$, $n_x =$ $n_z \approx 1.8$, $n_{iso} \approx 2.1$ [72]
ETL	Alq ₃	60 nm	1.76
Cathode	Aluminium	300 nm	1+6j

In general, OLEDs with a multi-layer structure forms an optical cavity. The spatial distribution of different optical eigenmodes highly determines the optical losses of OLEDs and

provides the basis for designing nanostructures to enhance optical extraction. Therefore, by utilizing a finite difference eigenmode (FDE) solver in Lumerical FDTD software, an eigenmode analysis for structures based on the parameters in Table 1 is performed to identify the optical losses in polarized OLEDs with crystallized EML as shown in Figure 3.10(c). For the model with an amorphous emitting layer, the loss channel of TE eigenmode is mainly located at the interface between the ITO anode and HTL, which behave like typical conventional OLED structures [74]. However, the TE mode loss channel of the crystallized model moves inside the emitting layer due to its higher in-plane ordinary refractive index n_y , as shown in Figure 3.10 (d). Therefore, unlike most of the previous research that focused on the design of the optical nanostructure located at the anode and cathode interfaces of conventional OLEDs to improve the extraction efficiency, more attention should be given to nanostructure inside the EML to enhance the extraction efficiency and EQE of polarized OLEDs based on LC material. In particular, this work focuses on designing the periodic index change grating in the EML.

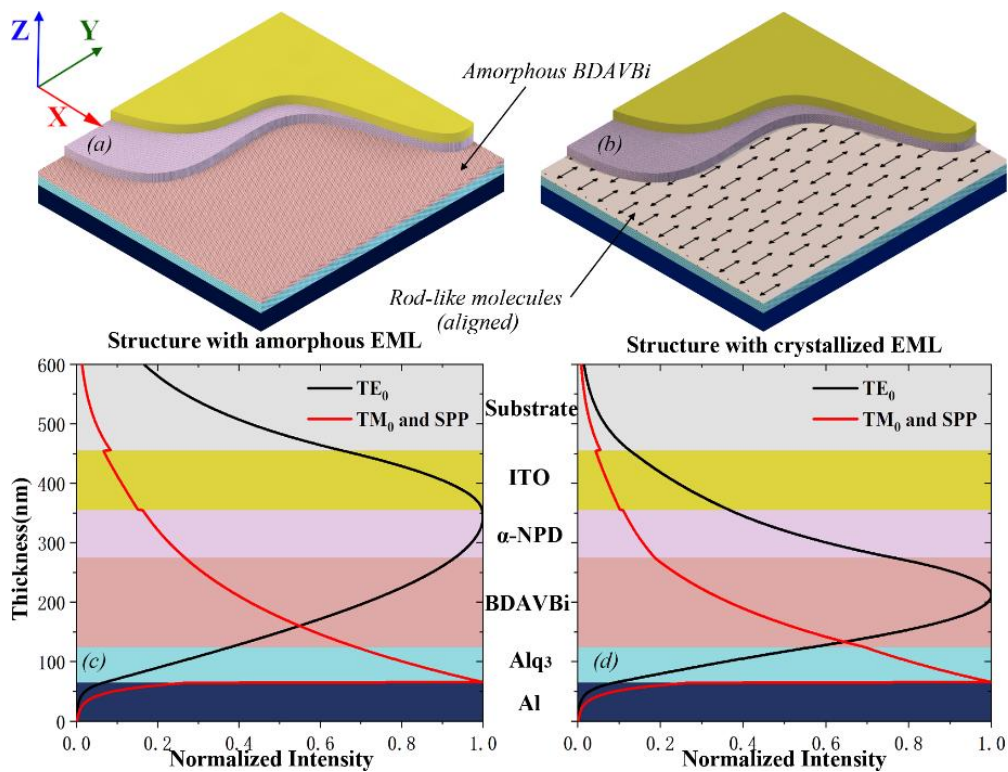


Figure 3.10 (a) Multi-layer structure of OLEDs with amorphous emitting layer; (b) Structure of OLED with crystallized emitting layer; (c) Normalized intensity distribution of lossy mode in OLEDs with amorphous emitting layer; (d) Normalized intensity distribution of lossy mode in OLEDs with

crystallized emitting layer, the TE lossy mode is confined in emitting layer due to high ordinary refractive index;

3.4.2 Light extraction by refractive index gratings in EML

According to the above results and discussion, the crystallization of the emitting layer indeed impacts the EQE of devices, where anisotropy of aligned EML leads to a significant TE waveguide mode loss channel at the EML. To suppress this energy loss and recover it to the output, we propose a refractive index grating in the EML, as shown in Figure 3.11. This grating expands along the x-axis, which can be potentially fabricated based on the photo-crosslink properties of the emitting material [58]. By compounding photo alignment moiety to BDAVBi molecules, the formed BDAVBi derivation can show liquid crystal characteristics. When the LC material is exposed under the interference fringes formed by UV light, the material in the exposed area (bright fringe area) undergoes photochemical cross-linking and curing to keep the rod-like molecules arranged in order stably; that is, the rod-like dichroic molecules are arranged in one direction. After that, the entire structure is heated so that the area where the photochemical cross-linking does not occur becomes a liquid with a disorderly distribution of rod-shaped molecules due to the increase in temperature, and then UV exposure is performed on all areas again. The amorphous regions are also crosslinked and cured. Finally, a stable index change grating structure is formed, consisting of a highly stable crystallized area and an amorphous area alternately, as shown in Figure 3.11.

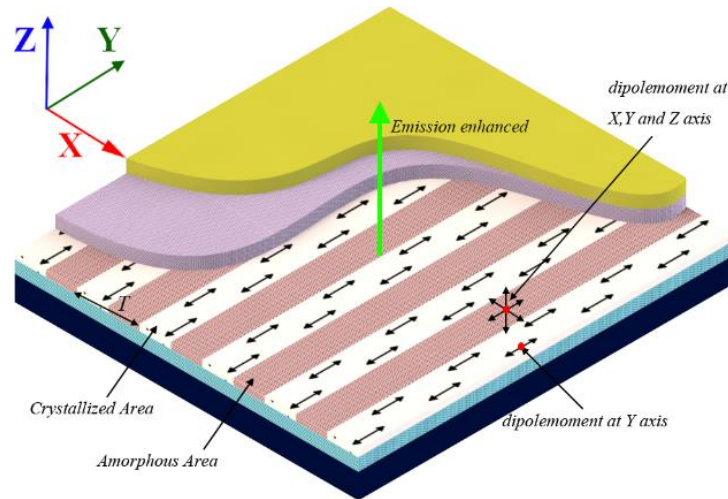


Figure 3.11 The OLEDs structure with refractive index grating in its emitting layer, the amorphous and crystallized areas are arranged along the x-axis, T is the grating period, $F = \Lambda/T$ represent the fill factor of grating, and Λ is the width of crystallized areas.

The FDTD method is employed for the simulation of the grating model. The structure of the grating model is shown in Figure 3.11. The material and thickness of each layer used in this

model are generally the same as in Table 3.1. The difference is that the refractive index gratings formed by periodical isotropic and anisotropic areas in the EML are considered in this model. As a comparison, an EML with a crystallized area without formed gratings is also simulated to study the enhancement in outcoupling efficiency and EQE. The reference devices in the remainder of the text will have the same geometric parameters as the grating devices.

The simulation is based on the classic 2-dimensional dipole model on XoZ plane, while a dipole array located in the centre of the z span of the EML represents the excitons [75]. For amorphous EML, the excitons inside it have random oscillation directions. To perform it precisely, each dipole in the amorphous area has three representative oscillating directions perpendicular to each other: in-plane direction (x and y axis) and vertical direction (z axis). On the contrary, in the crystallized area, the long axis of rod-like molecules is aligned along the y-axis, as shown in Figure 3.12. Their transition dipole moments and the oscillating direction are set along the y-axis. Additionally, to simplify the simulation, the molecular density and conductivity of the amorphous and crystallized are assumed to be the same, which ensures the dipole amount in the two areas is identical.

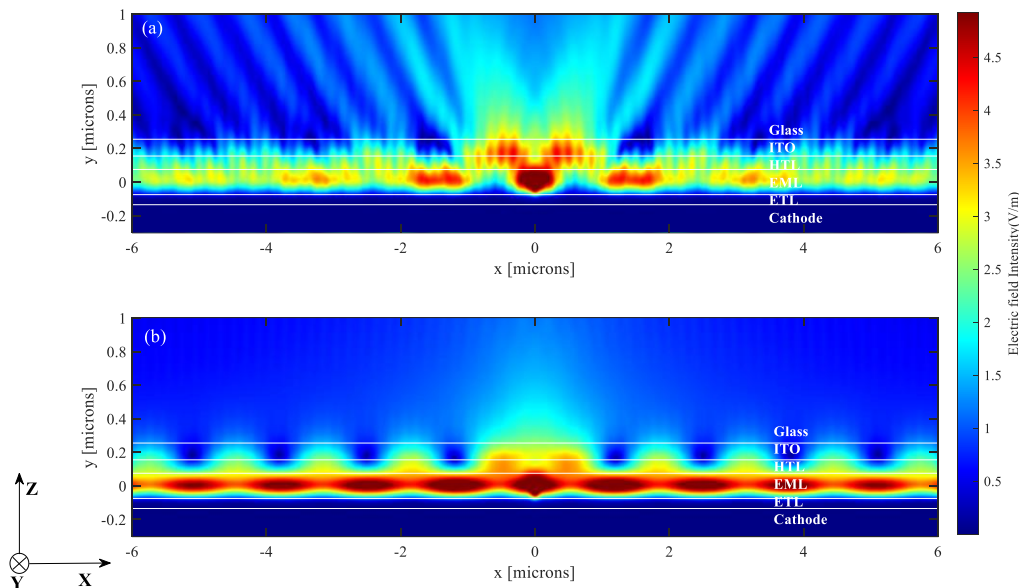


Figure 3.12 Simulated the electric field intensity distribution via side view. (a) Grating structure. (b) Non-grating structure.

Firstly, a simple 2-D one-dipole model simulation is implemented to verify the optical extraction effect of the refractive index change grating. The oscillation direction of the dipole is set along the z direction. Figure 3.12 shows the simulated electric field intensity from a section view of both grating and non-grating structures at 550 nm emission wavelength. Figure 3.12 (b) reveals clear periodical intensity patterns in the EML layer along the x-axis, which are

the TE waveguide modes transmitting in the EML layer. Since the dipole moment is set at the y -axis, its waveguide modes alternate strong and weak patterns along the x -axis. Besides, the intensity of the waveguide modes decreases along the x -axis due to the absorption of the medium.

In contrast, the TE waveguide modes experience a dramatic decrease along the x -axis in the EML with the grating structure, as shown in Fig. 4(a). Additionally, a series of alternating fringes are observed in the glass layer of the OLED with a grating structure. The waveguide modes in the EML are extracted, and light outcoupled in the glass substrate are enhanced.

EQE is commonly adopted to present the performance of OLED devices. The following equations generally derive the EQE of OLEDs.

$$EQE = \eta_{out} \times IQE \quad (3.2)$$

$$IQE = \frac{\gamma_{rad}}{\gamma_{rad} + \gamma_{nrad}} \quad (3.3)$$

Here, η_{out} is the optical outcoupling efficiency of the structure, and IQE is the internal quantum efficiency of the EML material. In this model, the IQE is considered 0.8 to simplify the simulation because the BDAVB_i is a fluorescent material. The $\gamma_{rad} = 0.8$ and $\gamma_{nrad} = 0.2$ are the EML's radiative and nonradiative decay rates, respectively. However, the energy of the dipole in homogeneous media is different from that in free space. The surrounding media and structures deeply influence the emission rate of the dipole. Hyunsu Cho et al. have investigated the influence of the Purcell factor of the dipole system on the simulation accuracy. The EQE can be substituted by the following equation [76]:

$$EQE_{full} = \gamma_{rad} \times \eta_{out} \times \frac{1}{1 - \gamma_{rad} + P(\lambda)\gamma_{rad}} \quad (3.4)$$

Where $P(\lambda)$ is the Purcell factor of the model, which is the ratio of dipole power to the source power in the FDTD solver. Note that η_{out} can be obtained in simulation via normalizing the outcoupled power to the source power. The outcoupled power is the total power received by a one-meter radius semi-circle at the far field. Therefore, EQE can be calculated via the above equation.

Polarization performance is usually the primary target for the design of these devices. The polarized ratio is generally applied for estimating the performance of polarized OLEDs and can be calculated based on the following equation [77].

$$\text{polarized ratio} = 10 \cdot \log \left[\frac{T_{TE}}{T_{TM}} \right] \quad (3.5)$$

Where T_{TM} and T_{TE} are the transmission of TM and TE polarized light, respectively. Their transmission is the ratio of outcoupled power to original dipole power.

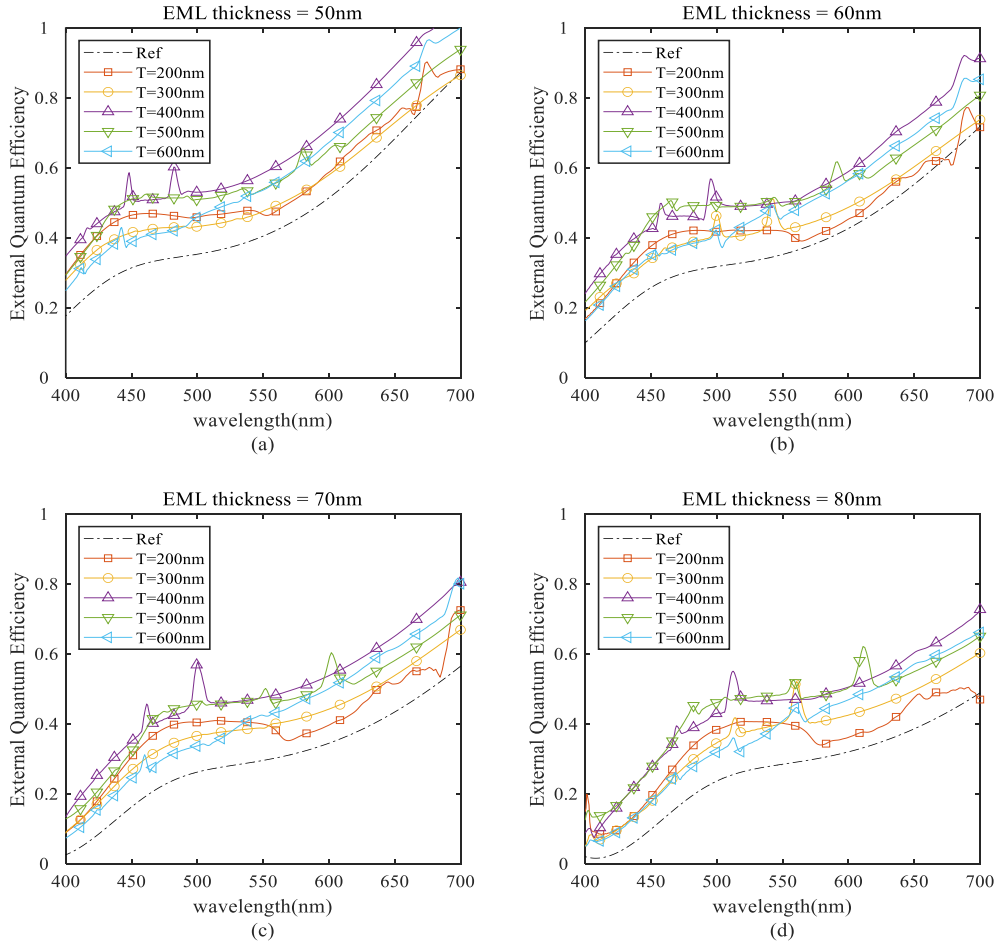


Figure 3.13 External quantum efficiency simulated for the reference device and devices with grating structures with different periods and different thicknesses of EML. (a) The EQE of the grating period from 200 nm to 600 nm with EML thickness at 50 nm, (b) The EQE of the grating period from 200 nm to 600 nm with EML thickness at 60 nm, (c) The EQE of the grating period from 200 nm to 600 nm with EML thickness at 70 nm, (d) The EQE of the grating period from 200 nm to 600 nm with EML thickness at 80 nm

Figure 3.13 above illustrates the simulation results of EQE of grating structures with periods from 200 nm to 600 nm and thicknesses of EML from 50 to 80 nm, respectively. The black dot curves in each sub-figure in Figure 3.13 (a) to (d) represent the EQE of a structure with total anisotropic EML at each thickness. Generally, these four groups of curves show a redshift trend with the EML layer's increasing thickness. For each figure, the EQE of structures with grating periods from 200 nm to 600 nm all show enhancement, which proves that the refractive index grating can enhance the EQE of whole devices. With the increasing grating

period, the EQE in all four figures experience an initial increase and then a drop after the periods exceed 400 nm. At the wavelength of 550 nm, the structure with a grating period of 400 nm and EML thickness of 50 nm shows the highest EQE.

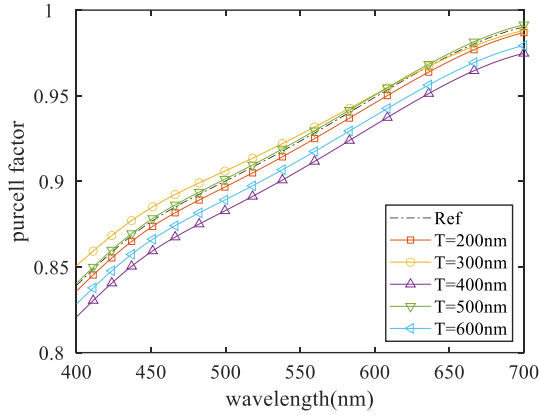


Figure 3.14 Purcell factor spectrum simulated for the reference device and devices with a thickness of EML of 50 nm.

In Figure 3.13, the grating structure with a period of 400 nm shows higher EQE. Purcell factor is introduced in the EQE calculation to improve the accuracy. The Purcell factor is the enhancement of a quantum system’s spontaneous emission rate by its environment. The Purcell factor adopted in this simulation is defined by the following equation.

$$Purcell\ factor = \frac{P_{dipole}}{P_{homo}} \quad (3.6)$$

Where P_{dipole} is the power of the dipole source radiated in the microcavity, and P_{homo} is the power that would be radiated in a homogeneous medium. In this simulation, it is an electrical dipole coupling with the microcavity of OLEDs, especially the EML layer. The Purcell factor could be influenced by both the geometry of the cavity and the refractive index [78]. In this case, because the proposed nanostructure is index grating, the grating period influences the medium surrounding each dipole, which influences the Purcell factor and further influences the EQE. Figure 3.14 shows the results of the Purcell factors against wavelength at different gratings periods with the thickness of EML of 50 nm. It can see lower Purcell factors at T=400 nm compared with other grating periods. Accordingly, the EQE can be worked out from Equation 3.4, which shows higher EQE with a gratings period of 400 nm compared with others.

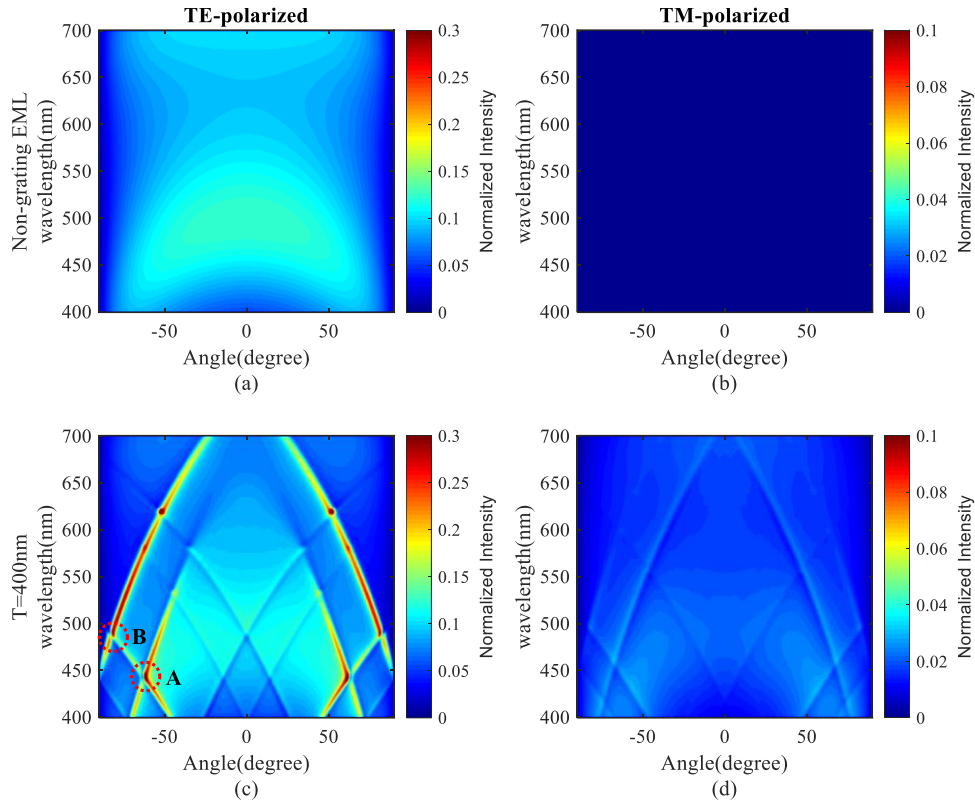


Figure 3.15 Simulation of the far field electric intensity distribution of reference devices and grating structure in TE and TM polarization, respectively. (a, b) The reference devices. (c, d) The grating structures ($T=400\text{ nm}$, EML thickness= 50 nm).

It is noticeable that each EQE spectrum in Figure 3.13 has several peaks, which are caused by the overlap between different dispersion orders of optical modes [79]. Figure 3.15 shows the electric intensity distribution in the far field for structures with a grating period of 400 nm and non-grating structures. The EML thickness is 50 nm in both cases. The far-field profiles are simulated with respect to emission angle and wavelength changes. EQE spectrum of the 400 nm grating period has pronounced peaks around 450 nm and 480 nm wavelengths in Figure 3.13(a). Correspondingly, its far-field distribution in Figure 3.15(c) shows the overlapping points of TE dispersion at wavelengths 450 nm and 480 nm , which are points A and B, respectively. Every peak of the EQE curves in Figure 3.13(a) has a corresponding overlapping point in its far-field distribution. Generally, the effectiveness of refractive index gratings leads to the overall lifting of EQE curves shown in Figure 3.13(a), which can be illustrated as a brighter area in Figure 3.15(c, d) compared with the reference non-grating device shown in Figure 3.15(a, b). In addition, Figure 3.15(b) does not show any pattern, and this is because the EML of the non-grating model is crystallized, which means all the dipoles in this model oscillate in the same direction and emission in the same polarization, so there is no power of TM mode can be observed in far-field of the non-grating model.

In summary, the peaks, in other words, the overlapping point, indicate specific enhancement at the corresponding wavelength. With these characteristics, grating structures enhances the optical extraction and EQE of whole devices. As the grating is designed to expand in the plane, TE mode experiences higher intensity at the overlapping point than TM mode, which confirms the purpose of our design.

Although the EQE of each period and grating thickness shows noticeable enhancement, the polarized performance of all the grating structures is not ideal. As seen in Figure 3.16, the polarized ratio of structures with different grating periods and thicknesses is generally lower than 10 dB. To further improve the polarized performance, an investigation of the effects of the fill factor on the polarized ratio is required, and the structure's optimal period must be determined first. It is obvious that grating with a 500 nm period shows the highest polarized ratio in all thicknesses, and EQE of a 500 nm period grating structure with a 50 nm thickness is acceptable. Consequently, the structure with $T=500$ nm and EML thickness with 50 nm, which shows 51.5% EQE and 8 dB polarized ratio at 550 nm emission wavelength, is chosen as the ideal model for further optimization of polarized performance.

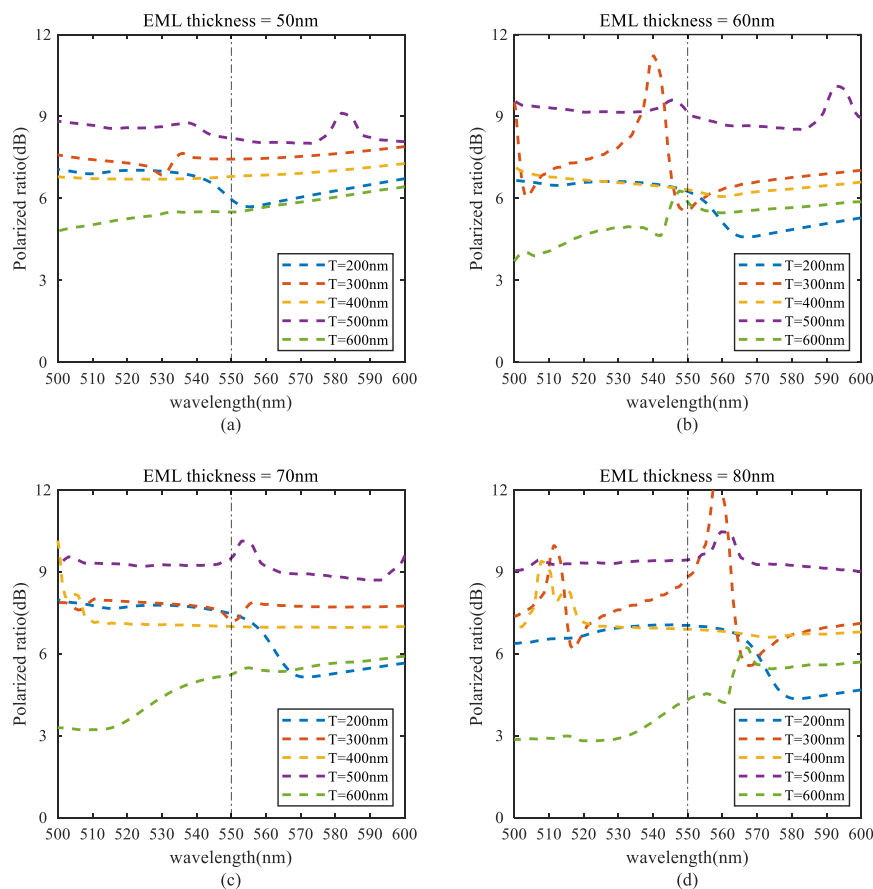


Figure 3.16 Polarized ratio simulated for the reference device and devices with grating structures with different periods and different thicknesses of EML. (a) The Polarized ratio of the grating period

from 200 nm to 600 nm with EML thickness at 50 nm, (b) The Polarized ratio of the grating period from 200 nm to 600 nm with EML thickness at 60 nm, (c) The Polarized ratio of the grating period from 200 nm to 600 nm with EML thickness at 70 nm, (d) The Polarized ratio of the grating period from 200 nm to 600 nm with EML thickness at 80 nm

The influence of the fill factor on the polarized ratio is first investigated to enhance the polarised ratio. The fill factor of grating refers to the ratio of the width of the crystallized area to the grating period. Unlike the previous simulation, the amounts of dipoles in the crystallised and amorphous areas are proportionally adjusted with the corresponding fill factor. A simulation with a fill factor sweeping from 0.3 to 0.7 at $T=500$ nm is applied. As shown in Figure 3.17(b), the polarized ratio drops slightly with the rise of the fill factor. Besides, the increase of the crystallized area leads to the increase of the effective refractive index of the EML layer, which further influences the EQE performance. In Figure 3.17(a), EQE experiences a decrease as the fill factor increase from 0.3 to 0.7. In conclusion, increasing the fill factor for merely 1 dB enhancement on polarized ratio decrease the EQE correspondingly by 10%, which is not very significant. Thus, an alternative method to enhance the polarized ratio is required.

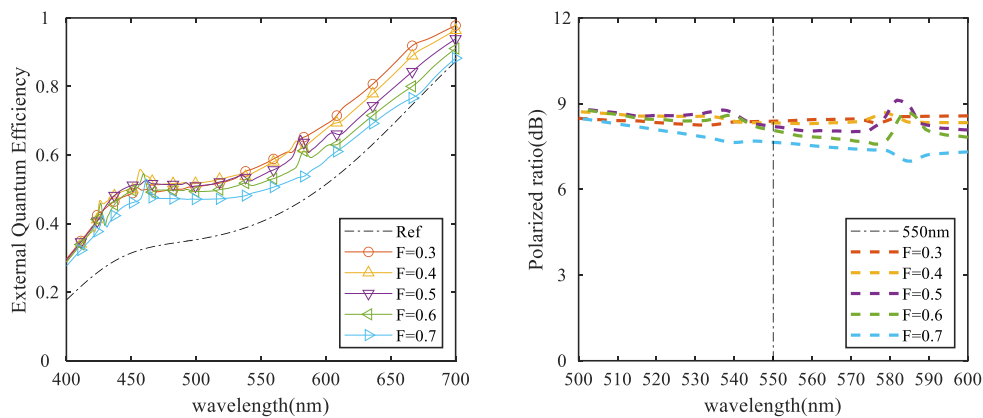


Figure 3.17 (a) EQE simulated for the reference device and devices with grating structures with different fill factors. (b) The polarized ratio of grating structure with different fill factors ($T=500$ nm).

3.4.3 Enhancing polarized ratio with an extra crystallized emitting layer

In section 3.4.2, the EQE and polarized ratio of OLEDs with grating structure employing LC material based on BDAVBi as EML material is comprehensively discussed, and significant EQE enhancement is achieved by inducing index change grating. However, the polarized ratio remains low (below 11 dB). An extra crystallised emitting layer is introduced based on the previous design to improve the polarized ratio without affecting the EQE enhancement from gratings. The simulation model is shown in Figure 3.18. An additional layer of crystallized EML is inserted beneath EML with a designed grating structure. Based on the optimized design

parameter of grating obtained in the last Section ($T=500$ nm, $F=0.3$, EML thickness with 50 nm), simulations were implemented to investigate the influence of extra layer thickness d to EQE and polarized ratio.

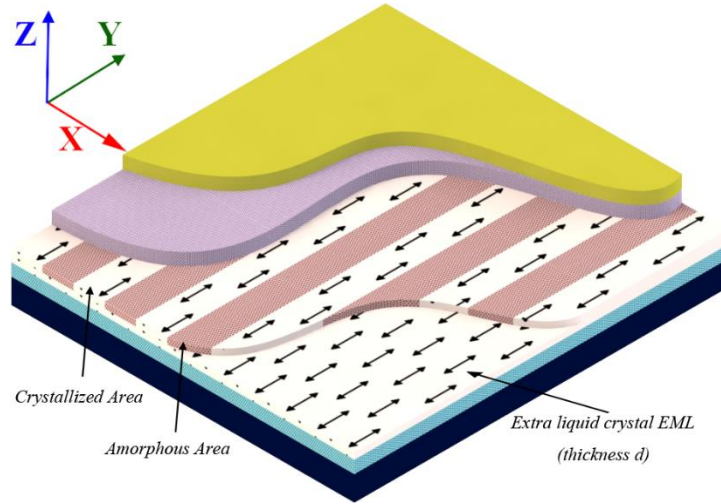


Figure 3.18 The OLED structure with an extra crystallized emitting layer underneath the grating structure. d is the thickness of the extra crystallized emitting layer.

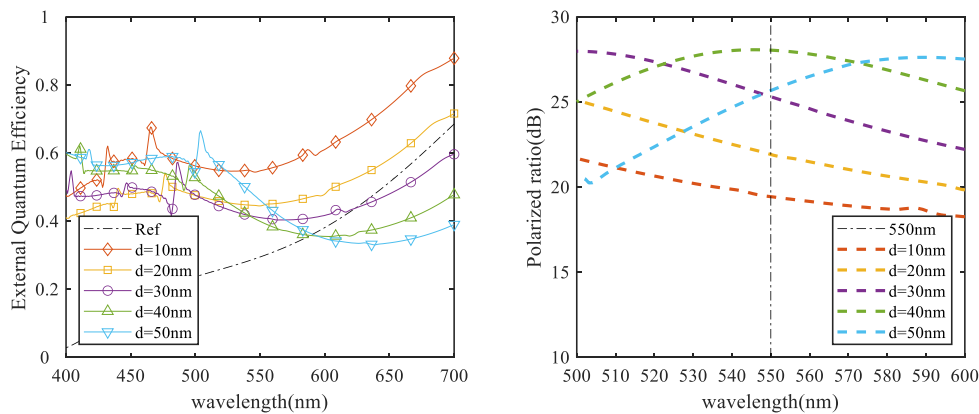


Figure 3.19 EQE spectrum simulated for the reference device and devices with grating structures with different thicknesses of the extra emitting layer. (b) The polarized ratio of structure with different thicknesses d of extra emitting layer ($T=500$ nm, $F=0.3$).

Figure 3.19 illustrates the EQE and polarized ratio with a change of thickness of extra layer d . Black dot curves in Figure 3.19(a) are the EQE from the model employing a crystallized EML with 60 nm thickness, which equals the sum of the thickness of the grating layer (50 nm) and the stated thickness (10 nm) of the extra layer. Remarkably, the EQE spectrum in Figure 3.19(a) experiences a decrease at the 500 nm-700 nm region with the increase of d . This is because the increasing thickness leads to larger optical thickness between the cathode and anode, which moves the outcoupling centre of the cavity and further influences the EQE in the desired wavelengths, but this decreasing of EQE is acceptable because the

polarized ratio is enhanced significantly. As expected, the polarized ratio is improved up to 28 dB at the wavelength of 550 nm when d increases to 50 nm shown in Figure 3.19(b). As comparison, the highest polarized ratio of polarized OLEDs based on luminescent liquid crystal material is reported to be around 20.3 dB [80]. Furthermore, based on the simulations with different geometrical dimensions of the structure, it is noticeable that the enhancing waveband is adjustable by changing the thickness of the extra layer and the whole EML layer. Simultaneously, the polarization ratio is guaranteed at a higher level.

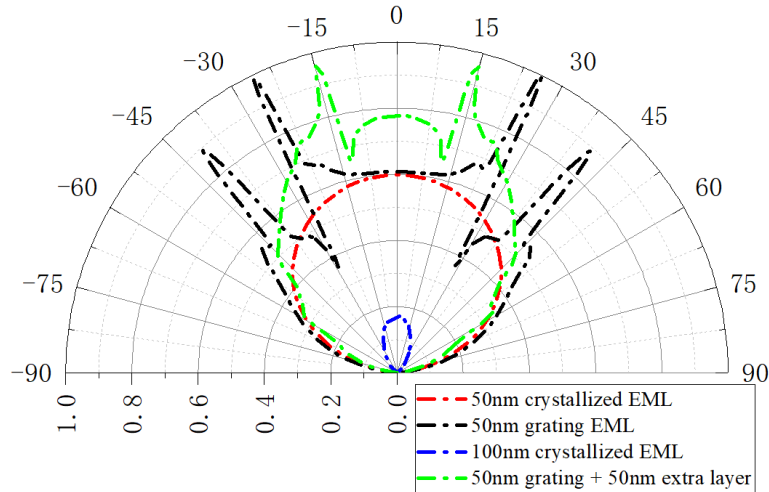


Figure 3.20 Normalized far-field intensity as a function of the viewing angle. ($T=500$ nm, $F=0.3$, emission wavelength=550 nm).

The far-field angular emission profile is another essential value to estimate the angular visibility of OLED devices. In Figure 3.20, the red and blue curves are structures with a total crystallized EML (without grating) of 50 nm and 100 nm thickness, respectively. Remarkably, the intensity of 50 nm thickness is much higher than the 100 nm thickness. This is because of the redshift trend due to increased thickness. A minimum point of the curve moves closer to the 550 nm emission wavelength with the thickness increased from 50 nm to 80 nm (see Figure 3.13). This trend continues with the further thickness increase. The green curve in Figure 3.20 shows that the emission intensity of the structure with $d=50$ nm extra crystallized emitting layer is enhanced in the full range of emitting angle. Compared with the structure with only 50 nm grating EML (black curve), the 50 nm grating plus 50 nm crystallized layer (without grating) structure has better uniformity in the entire viewing range, and its curve is similar to a Lambertian radiator, which is better for application in display.

3.5 Conclusion

Firstly, the TEOLED structure with Ag nanograting anode is investigated to enhance LEE. The FEM simulation result of field distribution indicates that the Ag grating anode can reduce the SPP and waveguide modes of TEOLED devices. Then FDTD simulation optimises the grating design by adjusting the grating period. The calculation predicts that a 60% enhancement of light extraction efficiency could be achieved by Ag grating anode on TEOLED with a period at 500nm. Additionally, the simulation result of the angular emission profile shows good viewing angle properties of the proposed structure, promising the commercial application potential of the metallic anode TEOLED.

Secondly, a conceptual design of high linearly polarized OLEDs with a refractive index grating in the emitting layer has been proposed and researched via numerical simulation. The influences on EQE and polarized ratio induced by EML thickness, grating period, grating fill factor and extra layer thickness are investigated comprehensively. A change in EML thickness can move the centre of the emission waveband of the entire structure, and a change in the grating period influences the enhancement of EQE. The grating fill factor only slightly influences both the EQE and polarized ratio. Furthermore, an extra crystalized emission layer significantly improves the polarized ratio with good EQE in the designed wavelength band. Finally, the optimized structure with a grating period of 500 nm and filling factor of 0.3 for emitting layer and extra emitting layer with a thickness of 50 nm shows 47% EQE and up to 28 dB polarized ratio at 550 nm emission wavelength. 56% EQE and 19 dB polarized ratio are also achieved at 550 nm emission wavelength with the flexible, designed structure ($T=500$ nm, $F=0.3$, and $d=10$ nm). In addition, the optimized structure has significant light extraction enhancement at each viewing angle. Due to the nature of the photo-alignment and photo-crosslink of LC material based on BDAVBi derivations, this grating structure is easy to fabricate and, therefore, could be a promising approach for the polarized OLEDs light source with scaling to high-volume manufacturing.

Chapter 4

Study of Passive Devices – FWM

on SOI waveguides

Chapter 4 focuses on the non-linear effect in passive devices, namely the FWM on SOI waveguide. Optimized designs of SOI waveguide and corresponding fibre-to-chip coupler based on numerical simulation are proposed for achieving high conversion broadband FWM, which is presented for high precision absolute distance measurement technique.

4.1 Introduction

4.1.1 Integrated Photonics

Integrated Circuit (IC) technology has significantly reformed human civilization since the 1970s. Nowadays, Chips based on ICs are embedded in every device, from smartphones to large airliners. The modern calculation, communication, fabrication, transportation, and the internet all rely on IC technology. Until the 2010s, Moore's law precisely predicted the technique revolution and market expansion of ICs. However, in the last decades, the advancement of semiconductor technology experienced its bottleneck due to physics law and economic limitations.

Meanwhile, the requirements for faster speed, wider band, higher efficiency, and cheaper cost increased significantly, making the ICs more critical for individuals and nations. The last three years' epidemic also reinforces the importance of chips in modern life. The photon, another ideal information carrier, attracted much attention from researchers and industry to further expand the functions and performance of semiconductor devices. After a few decades of development, Photonic Integrated Circuits (PICs) play an increasingly more prominent role in the semiconductor industry. Unlike the electronic integrated circuit, the PICs chip contains photonic devices that work with photons and electro-photon interactions. The idea of integrated photonics was started almost simultaneously with ICs. In 1969, Stewart E. miller initialled the concept of integrated optics. They enlightened the future of photonics research about integrated

photonic devices with electronic components based on the in state of the art microelectronics and optoelectronics technology at that time [81]. Smoekh and Yariv proposed a concept to integrate both electronic and photonic components on one single semiconductor substrate to achieve a repeater for fibre optics communication in 1972 [82], which provides an essential structure for following researchers about the blueprint of integrated optics. Since then, efforts have been made to achieve integrated photonics devices. The integrated optics devices or circuits contain active and passive components, including a source, waveguide, modulator, sensors, and coupler. Ideally, all the components should be fabricated on a single substrate to form a monolithic PIC. However, most PICs are heterogeneous because no single semiconductor material can satisfy different performance requirements to form different devices. Since the 1960s, various semiconductor materials have been applied to fabricate PICs, which can be categorized as direct band and indirect band materials. Materials with the direct band are generally used for active components, including high-power laser sources, Electro-Optic Modulators (EOM), photodetectors, and sensors. On the contrary, the indirect band material is hard to be applied for source devices since its radiative transition rate is relevantly low due to involving phonons during its radiative transition from the conductive band to the valence band. Therefore, indirect band materials are commonly used in passive components such as waveguides, couplers, and sensors with bonding with other materials.

Lithium Niobate, Germanium, and III-V compound semiconductors are most used for integrated active components. At the early stage of integrated optics, LiNbO_3 was adopted for most photonics components [83]. The Lithium Niobate material was considered one of the most promising materials for integrated photonics. It is used to fabricate optical switches and low-voltage EOM thanks to its excellent linear photoelectric effect [84]. The Germanium was seen as a promising candidate in the infancy of IC technology, and it can also be used in PIC. Germanium is commonly used for near-infrared photodiodes since its band gap energy. Although the Germanium has an indirect band, it can be transformed into a quasi-direct band via energy band engineering and be further applied for luminescent applications [85]. The III-V material is a series of compound semiconductors composed of elements in the third and fifth main groups. For example, Gallium Arsenide (GaAs), as a direct band III-V material, has been commercially applied for 850nm Lasers and detectors [86] and can be used for composing quantum well with ternary GaAlAs [87]. Another representative example of III-V material is Indium Phosphide (InP), commonly used as the substrate of III-V components [88]. An advantage of III-V materials is that they can compose various ternary or quaternary compounds,

for example, the $\text{Ga}_{1-x}\text{P}_x\text{In}_{1-y}\text{As}_y$ composed of GaAs, GaP, InAs, and InP, with different proportions, respectively. By adjusting the proportion of different elements, both their lattice structure and energy level structure are variable and further influence the refractive index and band gap, which means its properties are adjustable to satisfy different devices, including waveguides [89, 90], amplifiers [91, 92], near-infrared lasers [93], and detectors [94]. However, the highly integrated application of these materials is still limited because of their complex fabrication process and the relatively high volume of devices.

Passive on-chip devices have a more flexible choice of materials than active components. The essential part for passive devices is the waveguide; waveguides must connect all functional modules for cooperative working and advanced functions. Silicon dioxide (silica), Silicon Nitride (SiN), Silicon on Insulator (SOI) and some organic materials are mainly used for the waveguide in PIC [95]. The silica on silicon was used for waveguides in early-stage PICs. The refractive index of silica can be changed by doping germanium [96]. Therefore, a buried waveguide can be formed by doping in a particular area of silica. However, the large dimension of silica compares with others confines its applications. Various polymer is also used for fabricating waveguide, for example, Benzo Cyclobutene (BCB) [97], Polymethyl Methacrylate (PMMA) [98], and SU-8 photoresist [99]. The polymer waveguide is easy to fabricate and low cost, but they are easily damaged by high temperature, contamination, dissolution, and mechanical strength, thus hard to integrate with other materials. The SiN is widely used for isolating layers in Complementary Metal Oxide Semiconductor (CMOS) process. Recently, SiN has been increasingly used for waveguides and PICs [100, 101]. One of its advantages is the variable refractive index by adjusting the airflow proportion during the PECVD process of fabrication, which lets the SiN be seen as a promising candidate for PICs.

The last introduced material is the SOI, a material comprised of placing a thin film of silicon on a layer of insulated silicon dioxide substrate forming a silicon-silica-silicon sandwich structure, which has been widely used in PICs. Figure 4.1 illustrates a typical structure from the cross-sectional view of an SOI wafer. From bottom to top, there are silicon substrate layers, box layers made of silica, silicon on an insulator layer, and a cladding layer typically made of PECVD silica. Objectively speaking, silicon is not the best choice from a photonics perspective because the photoelectric conversion efficiency of silicon material is relatively low due to its indirect bandgaps, which limit its application for active devices, for example, the light source. Besides, the central symmetrical lattice structure makes direct electro-optic modulation on silicon impossible. However, due to the high compatibility with current CMOS technology

[102], the mass production of PICs based on SOI is cheap and straightforward compared with other materials. Therefore, the SOI is the most widely used material for waveguides and is seen as the mainstream for future PICs. The silicon material is transparent at 1.3~1.7 μm wavelength range. It is ideal to be widely applied for high confinement waveguides owing to high refractive index (3.5 around 1.5 μm wavelength), which means a small cross-sectional dimension of silicon waveguide for single mode and significantly reduces the dimension of PICs. Besides, although silicon is indirect band material, it can still be bonded with other materials to inject passive components. In recent years, a series of optical devices have been achieved using the SOI material, including couplers [103, 104], tuneable attenuators [105], optical switches [106] and modulators [107].

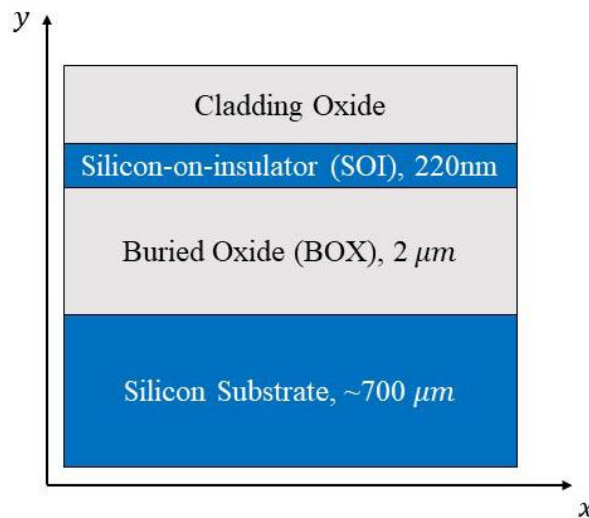


Figure 4.1 The structure of Silicon on Insulator (SOI) wafer with 220nm SOI layer.

4.1.2 silicon waveguide and non-linear effect

The two widely used SOI wafers are 220 nm and 340 nm in thickness of the silicon layer. Various waveguides have been proposed, in which the most used type is a rectangular waveguide, which can be categorized as a ridge waveguide, rib waveguide and slot waveguide. Figure 4.2 shows the cross-sectional structure of those three types of SOI waveguides. The ridge waveguide is the most suitable for single-mode propagation [108], which has the smallest effective area and most extensive effective index and highest confinement on the light wave propagation inside among those three types. The ridge waveguide typically provides the smallest bending radius thanks to its small effective mode area and cross-sectional dimension, which benefits ultra-dense photonic circuits. However, high confinement also suggests high propagating losses [109, 110]. The rib waveguide has a thin layer of silicon basement, as shown in Figure 4.2 (b), which releases confinement on the light wave, reduces the losses, and leads

to a relatively more significant dimension than the ridge waveguide. Another problem of rib waveguides is the high order mode loss since this structure allows mode leaking to the thin silicon basement, which requires highly accurate coupling alignment for being used in a fibre system. A slot waveguide is designed to propagate light in a low-index medium between to silicon ridge waveguide. The two side boundaries of the low index medium result in high quasi-TE components amplitude in the low index region [111, 112], which could suppress the propagation of quasi-TM mode. Among these waveguides, the most promising candidate is the ridge waveguide since it is much easier to fulfil the single mode conditions with this structure. The single mode FWM could supply sufficient conversion band for covering the C band. The rib waveguide is excluded due to potential inter-modal FWM, and the slot waveguide is excluded since most light energy is propagated outside silicon.

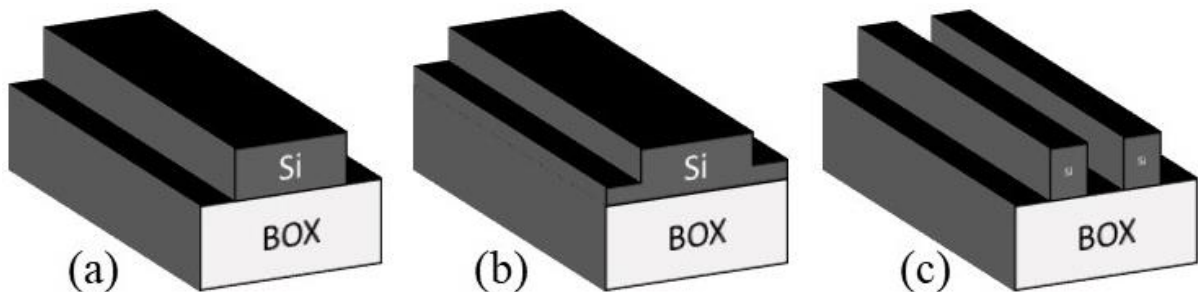


Figure 4.2 Three typical structures of SOI waveguide. (a) Ridge/Wire waveguide. (b) Rib waveguide. (c) Slot waveguide.

Nonlinear optics is an essential topic of modern optics research. It focuses on the research of nonlinear effect and corresponding application on optical medium with the interaction of coherent incident light. The interaction between medium and incident light could generate new frequency components. The interaction changes the medium's refractive index, polarizability, and absorption coefficient. Several typical nonlinear optics processes are shown in Figure 4.3, which include second harmonic generation (SHG) [113], sum frequency generation (SFG) [114], third harmonic generation (THG) [115], and four-wave mixing (FWM) [116], where the SHG and SFG are 2-order nonlinear effect, THG and FWM are 3-order nonlinear effect. Phase matching condition is crucial to achieving these non-linear effects. Besides, the medium should also have sufficient 2-order ($\chi(2)$ effect) or 3-order ($\chi(3)$ effect) polarizability [117].

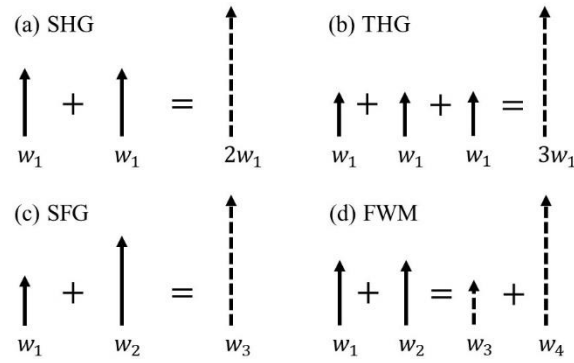


Figure 4.3 Schematic of different non-linear optics processes. (a) SHG, (b) THG, (c) SFG, (d) FWM

In addition, there are other 3-order non-linear effects of those as mentioned earlier, such as self-phase modulation (SPM) [118], cross-phase modulation (XPM) [119], and stimulated Raman scattering [120]. This project will mainly focus on the FWM in SOI waveguide for generating two symmetrically swept lasers for frequency scanning interferometry (FSI). Generally speaking, the intensity of the non-linear response is dominated by both intensity of incident light and the non-linear coefficient of material [117]. The non-linear coefficient is determined by the non-linear refractive index and efficient mode area, in which the non-linear refractive index is the intrinsic properties of materials. The efficient mode area mainly depends on the transmitting medium, which can be optimized by the dedicated geometrical design of the medium. High non-linear fibre (HNLF), photonic crystal fibre (PCF), and non-linear waveguide are the three most common mediums applied in non-linear optics. The PCF and HNLF are compatible with the current fibre optics system. They have higher non-linear coefficients than conventional single-mode fibre (SMF). The HNLF is commonly made from material with high nonlinearity, and PCF is a kind of organic fibre with a periodical pattern of air hollows embedded. Its nonlinearity is tuneable by tuning the period and dimension of air hollows [121].

However, the fibre-based non-linear mediums have relatively high cross-sectional area, typically micrometres level, which limits the power intensity and density inside them and further limits their non-linear response. The SOI material has both a high refractive index and a non-linear refractive index [122]. Thanks to the mature nanofabrication techniques, a non-linear SOI waveguide can be easily obtained now, which can confine the guided mode down to the sub-micrometres level due to the high refractive index. Such a small mode area can significantly enhance the guided power density, which allows lower incident power to achieve the non-linear effect. Additionally, the sub-micrometres level cross-sectional area is lower than the c-band wavelengths commonly adopted in telecommunication, which means the

transmission of the c-band wave is very sensitive to the change of the waveguide dimension [123]. Therefore, the waveguide's dispersion properties are easily tuned by changing the cross-sectional dimension to apply to different applications. Several optical non-linear effects were applied to achieve wavelength conversion and multiplication. In particular, the FWM, as a third-order nonlinear process which generates a new frequency of light from the interaction of two or more incident lights in a non-linear medium, has been investigated and seen as one of the main approaches to wavelength conversion in silicon photonics [123, 124], besides, it can be further applied in Optical Signal Processing [125], Optical Parametric Amplification [126], and Frequency Comb Generation [127].

4.2 The target of this chapter

This research aims to design and fabricate an SOI waveguide for achieving high conversion broadband Four Wave Mixing (FWM) to provide dual frequencies symmetrically sweeping laser source for the frequency scanning interferometry (FSI) system. The proposed wavelength conversion devices should work around the C band (1530 nm to 1565 nm).

The FSI is a technique for absolute distance measurement for single or multi-targets, which could be applied in many industries, including large-scale parts assembly (aero plane wing, shipbuilding) [128], robot arm calibration [129], and tiny deformation detection for structural analysis. It is generally a Michelson-type interferometer as shown in Figure 4.4 (a), a sweeping laser is split into two beams, one is bounced back by the reference mirror, and another is reflected back by the target, and finally received by the photodiode and then be processed by the signal analysis unit for solving the target distance. Figure 4.4 (b) explains the basic principle working flow for FSI signal process. Due to the optical path differences between the two arms, the beam reflected by the target will be a little bit delayed by τ . With a continuously sweeping laser source with a pre-determined frequency tuning range B , a stable distance-correlated beat frequency is detected by photodiode along the time domain. By applying Fast Fourier Transform (FFT), a stable distance-correlated peak signal is reconstructed in the frequency domain, which could be used for defining the target distance.

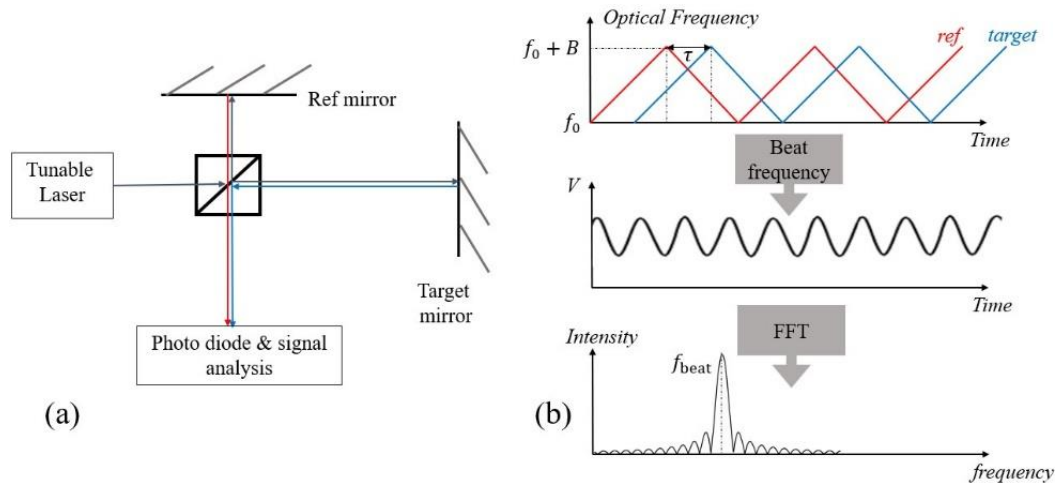


Figure 4.4 (a) Basic schematic of FSI system. (b) Principle of FSI system.

However, the accuracy of conventional single-frequency FSI is suffered from unwanted deliberate movement and vibration of both the target and sensing system., therefore a Dual-frequency sweeping concept was proposed to overcome this problem and enhance FSI accuracy, in which the second sweeping laser could compensate the measurement error induced by reasons above [130]. For the dual frequencies FSI, the two sweepings need to be synchronized and swept in the opposite direction along the frequency domain; in other words, one laser is tuned to a higher frequency, and another is tuned to a lower. Therefore FWM technique can be utilized to generate an idler beam with the exact frequency change and phase as the original signal beam, which perfectly matches the requirements of dual-frequencies FSI. Dual frequencies FSI achieved by FWM employing nonlinear semiconductor optical amplifier (SOA) have been achieved before [5]. However, their accuracy is still limited by the FWM conversion bandwidth and efficiency of non-linear SOA, which has been previously reported with 20 nm conversion band and -10 dB for highest conversion efficiency [131]. For non-linear OSA, it is difficult to retain a large signal to noise ratio for converted signal of FWM and the conversion efficiency decreases swiftly with increasing conversion band [132].

Thus, this project aims to design a suitable SOI waveguide, including coupling components for the FSI system. The benefit of employing SOI waveguide is making the whole FSI more compatible and minimised. There are three main topics in this chapter 4. The first is the nonlinear effect investigation of SOI waveguide, mainly the 3-order nonlinear effect. Mode analysis, phase matching, group velocity dispersion, high order nonlinear dispersion and FWM conversion efficiency of SOI ridge waveguide with different geometry dimensions were simulated and calculated via eigenmode solution, finite element method and Coupled

Nonlinear Schrödinger equations (CNSE). The second topic is mainly focused on the fibre-to-waveguide coupling technique, the design and optimization of two types of edge coupler including SU-8 covered taper coupler and free space coupler is discussed. Since an on-chip tuneable laser that satisfies the demand of FSI does not exist, the waveguide for FWM generating still must be deployed in a fibre optical system. Besides, the nonlinear conversion efficiency is also extremely sensitive to the input energy, which makes the waveguide to fibre coupling for our project an even more vital issue. Two types of edge couplers were designed and optimized for our application. The last topic is the test and experiment of SOI waveguide. Coupling efficiency, FWM conversion properties, and generated dual frequency sweeping properties are tested and demonstrated in the lab. All samples of SOI waveguide with coupler are fabricated in Glasgow University by e-beam lithography and tested in our lab at the University of South Wales. The allocated test results were summarized in this thesis to estimate the project's output and ignite the way for future work.

4.3 Theory of non-linear optical effects in the silicon waveguide

Naturally, non-linear optical effects are the result of the interaction between light and matter. More specifically, the electric polarization of the medium is caused by the interaction between the electric field of light and the carriers in the medium (for example, electrons and holes in silicon material). According to Maxwell's equation (Equation 2.2), the intensity of this process is defined as the polarization density of the medium \vec{P} , and for the light-matter interaction, it is given by,

$$\vec{P} = \vec{P}_L + \vec{P}_{NL} \quad (4.1)$$

Where \vec{P}_L and \vec{P}_{NL} are linear and non-linear electric polarization, respectively. Generally, the \vec{P}_{NL} is neglectable when the electric field of incident light is weak. However, for high-power applications or interactions with high nonlinearity medium, the non-linear electric polarization must be considered. The non-linear electric polarization density is given by following the series equation,

$$\vec{P}_{NL} = \vec{P}^{(1)} + \vec{P}^{(2)} + \vec{P}^{(3)} + \dots + \vec{P}^{(n)} + \dots \quad (4.2)$$

The $\vec{P}^{(n)}$ is the n^{th} order component of non-linear electric polarization correlating to n^{th} power of the electric field \vec{E} of incident light. The following equations give their relationship,

$$\vec{P}^{(n)}(t) = \sum_{\alpha_1, \alpha_2, \dots, \alpha_n} \epsilon_0 \chi^{(n)}(\omega_{\alpha_1}, \omega_{\alpha_2}, \dots, \omega_{\alpha_n}) |\vec{E}(\omega_{\alpha_1}) \vec{E}(\omega_{\alpha_2}) \dots \vec{E}(\omega_{\alpha_n}) e^{-i \sum_{m=1}^n \omega_{\alpha_m} t}| \quad (4.3)$$

Where $\chi^{(n)}$ is defined as the n^{th} order electric polarization ratio of the medium. It is a tensor with several elements. The number of elements is related to the order number n , for n^{th} order non-linear polarization. It involves the interaction among n incident electric fields or the incident lights with different frequency $\vec{E}(\omega_{\alpha_n})$. This work mainly focuses on the third non-linear effect. To simplify, the 3rd order non-linear electric polarization is written as,

$$P^{(3)}(\omega) = \epsilon_0 K \chi^{(3)}(-\omega; \omega_1, \omega_2, \omega_3) E_{\omega_1} E_{\omega_2} E_{\omega_3} \quad (4.4)$$

The number K is the optical constant depending on a specific optical process [133].

Despite the similar non-linear optical characteristics of the silicon waveguide and the non-linear fibre, the silicon waveguide also posse unique non-linear characteristics as semiconductor materials. This section introduces the theory and mathematic models adopted for the FWM simulation of silicon waveguides on SOI. The different non-linear effects considered for the FWM calculation are introduced, including the Kerr effect, Two-photon absorption, Free Carrier absorption, and Stimulated Brillouin Scattering. Then the theory and coupling equation of FWM is introduced.

4.3.1 The Optical Kerr effect in SOI material

The Optical Kerr effect is a third order nonlinear effect that the refractive index of the medium will change as a response to interaction with the external electric field change. The optical Kerr effect could occur without an external electric field. The incident light with enough intensity offers an electric field for its self-modulation because it is also an electromagnetic wave. The optical Kerr effect in SOI is very similar to it in optical fibres. Both are intensity dependent. The Kerr effect in SOI is characterized by its non-linear Kerr coefficient n_2 , which is crucial for the third-order non-linear effect. The n_2 has been reported as a range from 2.5×10^{-18} to $14.5 \times 10^{-18} m^2/W$. The n_2 is expressed as the following equation [117].

$$n_2 = \frac{3\chi_{Re}^{(3)}}{4c\varepsilon_0 n_0^2} \quad (4.5)$$

Where the c , ε_0 and n_0 are speed of light, permittivity, and refractive index in a vacuum, respectively. The $\chi_{Re}^{(3)}$ is the real part of 3rd order non-linear coefficient. When the wavelength of incident light is pre-determined, the intensity dependant non-linear refractive index is then equal to [117],

$$n(I) = n_0 + n_2 \quad (4.6)$$

Here the I is the intensity of incident light, n_0 is the refractive index of the material. Like the optical fibre, the light transmitted in the SOI waveguide is strictly confined inside the waveguide, there for the non-linear coefficient γ of SOI waveguide can be defined with effective mode area A_{eff} and non-linear Kerr coefficient n_2 .

$$\gamma = \frac{2\pi n_2}{\lambda A_{eff}} \quad (4.7)$$

Since optical fibre and SOI nano-waveguide usually have relevantly complicated sectional structures, so their effective mode area cannot be evaluated by commonly used $1/e^2$ average methods. Their effective mode area is defined as,

$$A_{eff} = \frac{(\iint_{-\infty}^{+\infty} |F(x, y)|^2 dx dy)^2}{\iint_{-\infty}^{+\infty} |F(x, y)|^4 dx dy} \quad (4.8)$$

the $F(x, y)$ is the mode profile function for different guided modes, which can be derived from mode analysis based on the FEM simulation mentioned before. With A_{eff} from rigorous simulation, the non-linear coefficient of the SOI waveguide is obtained.

4.3.2 Two-Photon Absorption

Two-Photon Absorption (TPA) indicates the non-linear process in that medium absorbs two photons simultaneously for stimulation from a normal ground state to a higher energy state. Since the energy of a single photon is insufficient to achieve such stimulation, two photons are required simultaneously, and the total energy of two photons is equal to or larger than the gap energy between two states. With the absorption of two photons, the stimulation from the ground state to the excited state is achieved through a virtual state. The hypothesis of TPA was initialled by Maria Goeppert-Mayer in 1931 [134], but the TPA was impossible to be observed

until the 1960s. When the Laser was invented [135], the scientist could demonstrate this process for the first time thanks to the high power density of the Laser. The probability of TPA is proportional to the energy of incident light, which indicates its nonlinearity [136]. Since the TPA process is highly power dependent, α_{TPA} , which is the nonlinear coefficient of TPA is given by [137],

$$\alpha_{TPA} = \beta_{TPA} \cdot I \quad (4.9)$$

Where β_{TPA} is the coefficient of degenerated TPA, which is correlated with the imaginary part of the non-linear coefficient of the material. Therefore, it can be given by [137],

$$\beta_{TPA} = \frac{-3\omega}{2c^2 n_0^2 \epsilon_0} \text{Im}(\chi^{(3)}) \quad (4.10)$$

The following figure shows the relationship between β_{TPA} and wavelength of the incident light, the data is based on Alan's experiment and Garcia's calculation [138, 139].

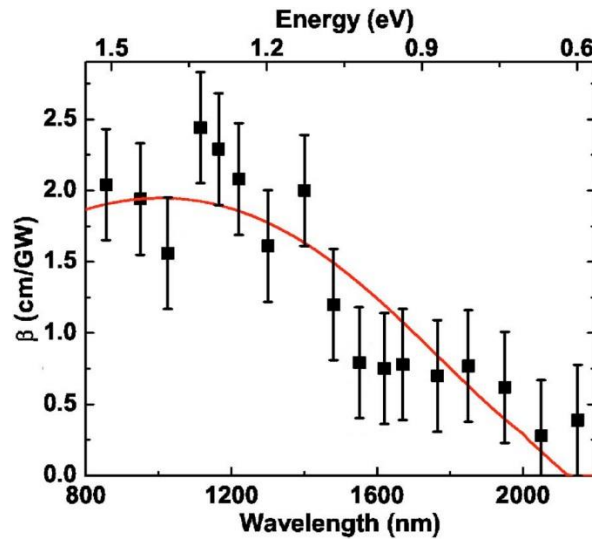


Figure 4.5 Measured β_{TPA} for 125 μm thick silicon wafer (black square) as a function of wavelength; Best fitting based on calculation from Garcia and Kalyanarama (solid red line).

As shown in Figure 4.5, the TPA is unneglectable in the application utilizing a non-linear effect Silicon waveguide, especially for the wavelength smaller than 2200 nm [122]. Since the band gap of silicon material E_g is around 1.12eV, when the energy of incidence photon is larger than $E_g/2$, the TPA will occur. The following Figure 4.6 present the TPA schematic in silicon. When the two incident photons have the same frequency, it is the degenerated TPA; when the frequencies are different, it is a non-degenerated TPA. A phonon is involved in both processes since silicon is indirect bandgap material. In silicon waveguides, the TPA is also

related to the dimension of a waveguide. The injecting power to the silicon waveguide can not be very high for commonly used 220 nm and 340 nm thickness; otherwise, the TPA will dominate the losses due to high power density for the nano-waveguide. Typically, the limitation of injection power for 220 nm thickness silicon waveguide is 300 mW (25 dBm).

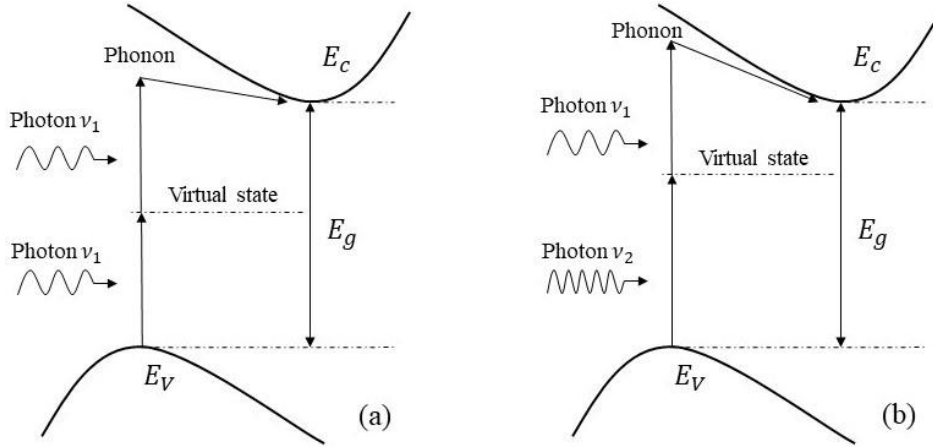


Figure 4.6 Schematic of TPA in silicon (a) Degenerated TPA (b) Non-degenerated TPA.

4.3.3 Free Carrier Absorption

Free Carrier Absorption is a phenomenon that occurs in semiconductor when free charge carrier excites to another intra-band energy level or sub energy level, and absorbs photon simultaneously, which results in absorption of the incident light by semiconductor material. For silicon waveguides, free electrons and holes will be generated in the valence and conductive bands when TPA occurs while the light is transmitting through. These free carriers, including electrons and holes, can interact with incident light, which results in the Intra-band Transition of free carriers [140] and the absorption effect for incident photons. If the incident light is a superfast pulse, the free carrier concentration N in SOI waveguide can be given by [140-142],

$$\frac{dN(t)}{dt} = \frac{\beta_{TPA}}{2h\nu_0} I^2(t) - \frac{N(t)}{\tau_{eff}} \quad (4.11)$$

Where h , ν_0 , I , and τ_{eff} are the Planck constant, light frequency, light intensity, and carrier lifetime, respectively. With the carrier concentration, the free carrier absorption coefficient $\Delta\alpha$ is given by following The Drude-Lorenz equation [143],

$$\Delta\alpha = -\frac{e^3\lambda^3}{4\pi^2c^3\varepsilon_0n} \left[\frac{\Delta N_e}{(0.26m_0)^2\mu_e} + \frac{\Delta N_h}{(0.39m_0)^2\mu_h} \right] \quad (4.12)$$

Where μ_e and μ_h are the mobility of electrons and holes, respectively, N_e and N_h are the concentration of electrons and carriers, respectively, m_0 is the mass of the electron. e is

the elementary charge. The above equation suggests that the FCA highly depends on the concentration of free carriers. Increasing the intensity of incident light enhances the TPA. Meanwhile, the concentration of free carriers is also increasing, consequently leading to higher FCA.

4.3.4 Stimulated Brillouin Scattering in the silicon waveguide

SBS is a third-order nonlinear phenomenon that involves interaction between travelling-wave photons and phonons, namely the light wave and acoustic wave. This process results in scattering of photons due to the phonons. In the SOI waveguide, leakage of phonons to the silica box layer (unlike fibre) prevented observation of SBS in the SOI platform. Most researchers aim to design specific structures to enhance the SBS for other applications to confine the phonons by a local etching of the buried oxide in a pedestal waveguide structure [144] or a fully suspended silicon membrane structure [145]. Even for this enhanced design, the SBS is still hard to be observed (lower than the threshold) in short (mm, cm level) SOI waveguide because of the weak overlap between guided optical and acoustic modes.

That said, the conventional silicon waveguide as an SBS material has inherently poor SBS gain coefficient, high speed of sound, and significant acoustic losses. For reference, the estimated SBS gain coefficient g_P which is around $2.4 \times 10^{-12} (m * W^{-1})$ [146]. To estimate the SBS impact on the FWM in SOI waveguide, the SBS threshold equation (equation 4.13) in fibre is adopted for the complex SOI SBS coupler model [147], as the fibre could be seen as the worst-case scenario. Here g_P is the SBS gain coefficient, A_{eff} is the effective area of the waveguide at end facet. L_{eff} is the effective length of the SOI waveguide. According to the Agarwal's nonlinear optics handbook, the SBS pump threshold is given by $P_{th} = G_{th} \cdot A_{eff} / (g_P L_{eff})$ [117, 148], where G_{th} is the exponential gain of SBS [149], basing on the critical condition of SBS from equation 9.2.4 in Agarwal's handbook, the G_{th} is commonly taken as value 21 at critical pump energy [117]. To calculate the threshold with certain linewidth of pump and SBS signal, an extra term $(\Delta\nu_B + \Delta\nu_p) / 2\Delta\nu_B$ is multiplied to Agarwal's equation, which give us the equation 4.13, where $\Delta\nu_B$ and $\Delta\nu_p$ are the SBS wave linewidth (Unit: GHz) and pump wave linewidth (Unit: kHz), respectively. Particularly, the constant A has values as two times of G_{th} as $A = 2G_{th} = 42$.

$$P_{th} \approx G_{th} \times \frac{1}{g_P} \frac{A_{eff}}{L_{eff}} \times \frac{\Delta\nu_B + \Delta\nu_p}{2\Delta\nu_B} = A \times \frac{1}{g_P} \frac{A_{eff}}{L_{eff}} \times \frac{\Delta\nu_B + \Delta\nu_p}{\Delta\nu_B} \quad (4.13)$$

According to the This equation estimates the SBS pump threshold for an SOI waveguide with a $400 \times 600 \text{ nm}$ cross-sectional dimension. The waveguide length is assumed as 10^{-2} m , with the effective area A_{eff} as $0.24 \times 10^{-12} \mu\text{m}^2$, which is an estimated value based on the cross-sectional area of waveguide for simplifying the calculation. The calculated SBS pump threshold P_{th} is around 420W, much higher than the power of the tuneable laser and amplifier proposed for this project. For this reason, the SBS impact is not considered for FWM conversion efficiency calculation and simulation.

4.3.5 The FWM in the silicon waveguide

Four-wave mixing (FWM) is a well-known technique to achieve all-optical control wavelength conversion, which has been widely applied in all-optical communication and all-optical processing system. Most commercial FWM-based devices are built with optical fibre due to deep and comprehensive research towards optical parametric amplification (OPA) and wavelength conversion processes based on in-fibre FWM. The refractive index and non-linear coefficient of silicon are significantly higher than fibre, which allows high conversion efficiency FWM to be achieved in silicon nano-waveguide with dimensions far less than optical fibre.

FWM is a third-order non-linear process described by $\chi_{(3)}$ coefficient as well, it will occur when at least two optical beams with different frequencies are transmitted simultaneously in the same non-linear medium. Figure 4.7(a) is the energy level diagram for the single-mode non-degenerated FWM process, which express the interaction between four different frequencies. Assuming two incident lights as pump lights with different angular frequency ω_1 and ω_2 , due to third-order non-linear electric polarization of medium and SPM and CPM, two new frequencies ω_3 and ω_4 will be generated. If a light beam of ω_3 or ω_4 also incident to the medium, it will be amplified as optical parametric amplification (OPA), as can be seen in Figure 4.7(b). The frequency of four beams follows $f_1 + f_2 = f_3 + f_4$, the frequency difference between f_3 and f_1 is equal to the difference between f_2 and f_4 .

If two of the three incident beams are at the same frequency, the process is then transformed to degenerated FWM. As it is shown in Figure 4.7(c), for this case, the two incident beams with the same frequency can be seen as a single pump beam with frequency f_p and photon energy $\hbar\omega_p$, then an incident signal beam with a nearby frequency f_s could be amplified by the pump beam, the amplification of each signal photon $\hbar\omega_s$ will absorb the

energy of two-photon from the pump beam $\hbar\omega_p$ and generate a new photon with energy $\hbar\omega_i$, which is normally called idler frequency or idler beam. The idler frequency f_i will be located at the opposite side of the signal frequency f_s about the pump frequency f_p . The idler frequency and signal frequency are symmetric with respect to the pump frequency.

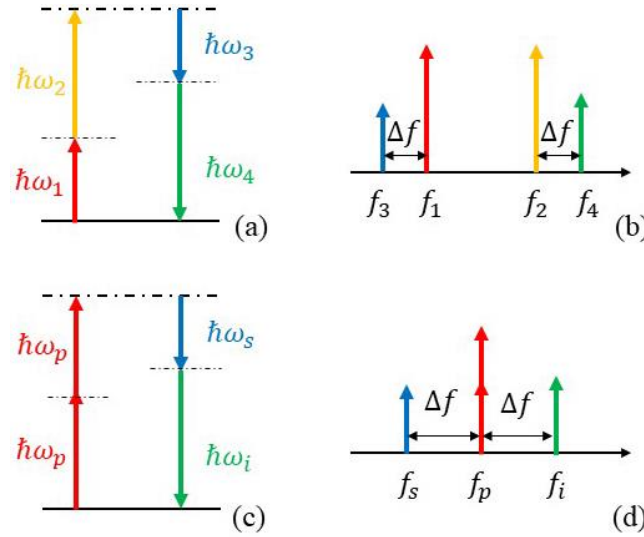


Figure 4.7 Schematic of FWM in silicon (a) Energy level diagram of single mode Non-degenerated FWM, (b) frequency view of Non-degenerated FWM, (c) Energy level diagram of single mode Degenerated FWM (d) frequency view of Degenerated FWM.

According to this correlation between idler light and signal light of FWM, it is ideal for generating a symmetrical sweeping dual-frequencies source for the FSI system. The dual-frequencies FSI requires the intensity of light frequency to maintain at a comparable level [130], which makes the conversion efficiency of FWM crucial for our SOI waveguide design, here the method of calculation of FWM conversion efficiency in silicon waveguide is introduced. The maximum efficiency of FWM conversion only occurs when the phase-matching condition of two incident lights is satisfied [117]. For non-degenerate FWM, the phase-matching condition is given by,

$$k_1 + k_2 = k_3 + k_4 \quad (4.14)$$

Where $k = 2\pi/\lambda$ is the wavenumber for different beams involved in an FWM interaction. Obviously, for degenerated FWM, equation 4.14 is reformed to,

$$2k_p = k_i + k_s \quad (4.15)$$

Where k_p , k_i and k_s are wavenumber of pump, idler, and signal light, respectively, when the phase-matching condition is broken, their linear phase mismatch is,

$$\Delta k_{Linear} = 2k_p - k_i - k_s \quad (4.16)$$

With the energy conversion condition $1/\lambda_i = 2/\lambda_p - 1/\lambda_s$ [150] derived from equation 4.15, the linear phase mismatch is approximately transformed to,

$$\Delta k_{Linear} = -\beta_2(\Delta\omega)^2 - \frac{1}{12}\beta_4(\Delta\omega)^4 \quad (4.17)$$

Where $\Delta\omega = |\omega_p - \omega_s|$ is the frequency mismatch between the signal and pump light. Apparently, the frequency difference between the idler and pump beam should be the same value. β_n is the n^{th} order dispersion coefficient of the waveguide, it is equivalent to the n^{th} order derivative of effective index n_{eff} of silicon waveguide with respect to angular frequency, the β_n is given by the following equations [117],

$$\beta = n_{eff}k, k = \frac{2\pi}{\lambda}, \beta_n = \frac{d^n \beta}{d\omega^n} \quad (4.18)$$

Where β and ω are propagating constant and angular frequency, respectively. The mode effective refractive index n_{eff} is defined as the ratio of the propagating (or phase) constant β to the wavenumber k in a waveguide, which is used to quantify the increase in the wavenumber caused by the wave medium. The effective index depends on several factors, including the geometrical design of the silicon waveguide, the surrounding material index, mode wavelength and mode number. In this work, it is solved by an eigenmode solver with FEM simulation. The obtained effective refractive index n_{eff} is an array of values with respect to frequency, then its derivative is calculated using equation 4.18 for the dispersion analysis of the SOI waveguide. It is noticeable that the linear phase mismatch is a function with respect to frequency mismatch $\Delta\omega$, which seems contradicted to β_n derived from n_{eff} with respect to frequency. However, in simulation, the pump wavelength is treated to be constant. Therefore the $\Delta\omega$ can be resubstituted to a function with respect to signal frequency. For the proposed system, the dual sweeping frequencies for FSI indicate the signal and idler beam, and the input beams of the theoretical model are simplified to a sweeping signal and a constant pump wavelength.

As a non-linear process, the phase mismatch of the FWM process also contains a non-linear term, which is given by,

$$\Delta k_{non-linear} = 2\gamma P_{pump} \quad (4.19)$$

Where γ is the non-linear coefficient, which is given by equation 4.7, and P_{pump} is the power of the pump wave. In addition, the effective mode area A_{eff} at pump wavelength for calculating γ is also solved by FEM simulation. With equations 4.19 and 4.17, the phase mismatch Δk of FWM in SOI waveguide is given by,

$$\Delta k = 2\gamma P_{pump} - \Delta k_{linear} = 2\gamma P_{pump} + \beta_2(\Delta\omega)^2 + \frac{1}{12}\beta_4(\Delta\omega)^4 \quad (4.20)$$

It is easy to be found that the non-linear term is a constant value for our model since the pump light is assumed to be a constant wavelength with steady power input. Thus the phase mismatch is seen as a function with respect to the signal wavelength (or frequency), which indicates that the dispersion modulation based on the geometry of the SOI waveguide is the vital factor for the design process, the condition of maximum conversion will be the equalization between non-linear and linear phase mismatch.

The frequency tuning range in an FSI system is crucial for measurement resolution and accuracy [151]. Therefore a broad tuning range laser is usually adopted as the signal source of the FSI system, which creates challenges in the design of the SOI waveguide to achieve broad FWM conversion bandwidth. The FWM conversion band should be wide enough. A generated idler light should have a comparable intensity to the signal light, which signifies the importance of accurate calculation of conversion bandwidth and efficiency. Typically, approximate processing is adopted for treating the small signal of the FWM process, and the conversion efficiency CE_{approx} is given by [152],

$$CE_{approx} = \frac{P_i}{P_{s_0}} = \left[\frac{\gamma P_{pump}}{g} \sinh(gL) \right]^2 \quad (4.21)$$

Where L is the effective interaction length. P_i and P_{s_0} are the converted idler power and injected signal power, respectively. g is the parametric gain coefficient.

$$g = \sqrt{\left[\gamma P_{pump} \Delta k_{linear} - \left(\frac{\Delta k_{linear}}{2} \right)^2 \right]} \quad (4.22)$$

However, the conversion efficiency CE_{approx} obtained by this method does not account for the absorption of silicon waveguide. Gao et al. explained another approach for conversion efficiency solving based on the CNSE [150]. With the phase mismatch obtained, the following

equations are solved by a customized MATLAB script (see appendix A.1) to get the amplitude of the pump, signal, and idler signal, respectively.

$$\left\{ \begin{array}{l} \frac{dA_p}{dL} = -\frac{1}{2}(\alpha_p + \alpha_{TPA_p} + \alpha_{FCA_p})A_p + j\gamma_p \left[|A_p|^2 + 2|A_s|^2 + 2|A_i|^2 \right] A_p \\ \quad + 2j\gamma_p A_p^* A_s A_c \exp(j\Delta kL) \\ \frac{dA_s}{dL} = -\frac{1}{2}(\alpha_s + \alpha_{TPA_s} + \alpha_{FCA_s})A_s + j\gamma_s \left[2|A_p|^2 + |A_s|^2 + 2|A_i|^2 \right] A_s \\ \quad + j\gamma_s A_c^* A_p^2 \exp(j\Delta kL) \\ \frac{dA_i}{dL} = -\frac{1}{2}(\alpha_i + \alpha_{TPA_i} + \alpha_{FCA_i})A_i + j\gamma_i \left[2|A_p|^2 + 2|A_s|^2 + |A_i|^2 \right] A_i \\ \quad + j\gamma_c A_s^* A_p^2 \exp(j\Delta kL) \end{array} \right. \quad (4.23)$$

Where α , α_{TPA} and α_{FCA} are linear absorption, twin photons absorption (TPA), and free carrier absorption (FCA) coefficient, respectively. The parameters A_p , A_s and A_i are the amplitude of the pump, signal, and idler, respectively. L is the coupling length of the SOI waveguide. The conversion efficiency is then given by:

$$CE_{CNSE} = \frac{P_i}{P_{s_0}} = \frac{A_i^2}{P_{s_0}} \quad (4.24)$$

The conversion efficiency derived by CNSE is more comprehensive than the CE_{approx} since the absorption effects are considered. The conversion efficiency calculated by both methods is all with respect to the frequency of the signal beam in this thesis. The conversion band can then be accounted as the -3dB band or the Full Width Half Maximum (FWHM) of the main peak in the spectrum of conversion efficiency.

4.4 Design and numerical simulation of SOI waveguide for FWM

In this section, the simulation and corresponding result of the FWM in SOI waveguide are introduced step by step. Firstly, the mode analysis of silicon waveguide with variable cross-sectional dimensions is conducted by commercial FEM software. Then dispersion analysis and modulation of the silicon waveguide are implemented. Finally, the conversion efficiency results with respect to different parameters are obtained. Based on these simulation results, a design of silicon waveguide on SOI is initiated for fabrication.

4.4.1 Mode analysis of silicon waveguide

An accurate simulation of the mode profile is crucial for the FWM simulation. The effective index and effective mode area as a function with respect to frequency are required for phase mismatch calculations. The mode profile of the SOI waveguide correlates to both the cross-sectional dimension and the wavelength of the guided mode. For this project, the waveguide should be designed to work in the C band because the peripheral optical devices for the FSI system are all working in the C band. Furthermore, the C band supplies various choices of devices. Therefore, this project adopts the 220 nm thick silicon layer SOI platform for the FWM waveguide design rather than the 340 nm platforms because 220 nm is the cut-off thickness for satisfying the single mode condition of wavelength around 1550 nm, and further avoid the multi-mode on vertical direction of the waveguide's cross-section. Maintaining the single mode is crucial for this project since the conversion of intermodal FWM experiences more loss than the single FWM [153], the 220nm silicon waveguide is covered by PECVD silica with over 3 μm thickness for cladding layer. In simulation, the thickness of cladding layer is treated as infinite for simplification, since its dimension is far bigger than the silicon core.

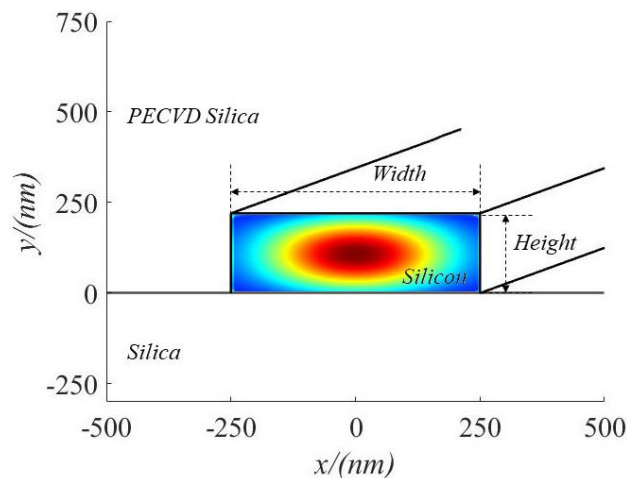


Figure 4.8 Geometry of buried SOI waveguide for simulation.

To achieve high conversion FWM in a silicon waveguide, the proposed waveguide should be able to confine and propagate the light wave at the C band. A fast mode search based on the effective index method (EIM) is conducted to verify that. The test wavelength is set as 1546 nm, since the proposed pump laser source for the experiment is 1545~1546 nm. Figure 4.8 shows the modal used for mode simulation. As can be seen, the model is a buried strip of silicon waveguide surrounded by silica. The upper side cladding layer silica is supposed to be the

PECVD fabricated silica due to the process for fabrication, but in simulation, it is treated as same as the silica in the box layer. The original refractive index data adopted for the simulation is from Palik's Handbook [154]. For mode search simulation, a single index value at 1546 nm is adopted ($n_{box} = 1.444$, $n_{core} = 3.47$, $n_{cladding} = 1.444$). Obviously, the only changeable variable for influencing the mode profile is the width because the height is fixed at 220 nm, and the width is sweeping from 200 to 1000 nm. Figure 4.9 is the effective index n_{eff} for possibly existed mode calculated by EIM versus the width of the waveguide at 1546 nm wavelength. In the result, only the modes above the cladding index are possibly guided. The bottom boundary is the cladding index. The fundamental quasi-TE mode (TE0) is mainly focused for this project, which is the most used mode for 220nm thick SOI devices [102]. It is seen that the cut-off width for the single TE0 mode is located at 350 nm, where the higher order TE1 mode appearances, and the TE2 mode is supported with width bigger than around 680 nm. To avoid the potential intermodal losses, the mode higher than TE2 needs to be avoided. Besides, although the waveguide width below 350 nm supports pure single-mode propagation, the low effective mode index (<2.2) indicates insufficient confinement of the silicon core, which leads to increasing losses and poor non-linear coefficient. Therefore, a width range from 300nm to 700nm is adopted for a more accurate FEM mode simulation of the TE0 mode. Additionally, effective indices of the quasi-TM modes in 220 nm thick SOI waveguide are generally poor, and they are not accounted for in the dispersion analysis for FWM calculations.

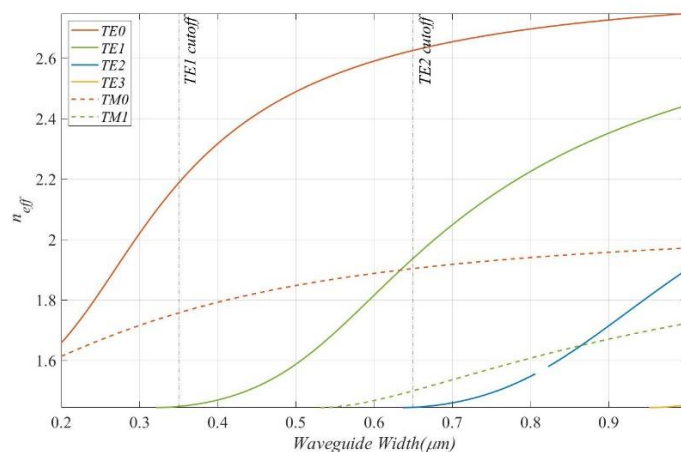


Figure 4.9 Calculated effective index of modes in 220 nm thick strip SOI waveguide versus width of waveguide.

The eigenmode solver of COMSOL is employed for accurate mode solving and the dispersion effective index calculation. The modal used is generally the same as EIM mode

searching, but the index adopted is the dispersion material index. Figure 4.10 is the fundamental TE mode distribution with a width from 300 nm to 700 nm. Generally, the confinement of silicon waveguides gets stronger with increasing width. Waveguide with a width from 400 to 700 nm is capable to confine most of the energy inside the silicon core, as shown in Figure 4.10(b-g) with increasing width, the energy concentrating at the side wall decreases. Notably, in Figure 4.10(a), it can be seen that most of the energy is propagated outside the 300 nm width silicon waveguide due to narrow dimension. Besides, the Figure 4.10 (h) and (i) show TE1 and TE2 mode for the width of 700 nm, respectively, higher mode exists, which should be avoided for this project. Therefore, width range from 400 to 600 nm is adopted for the dispersion analysis and FWM calculations.

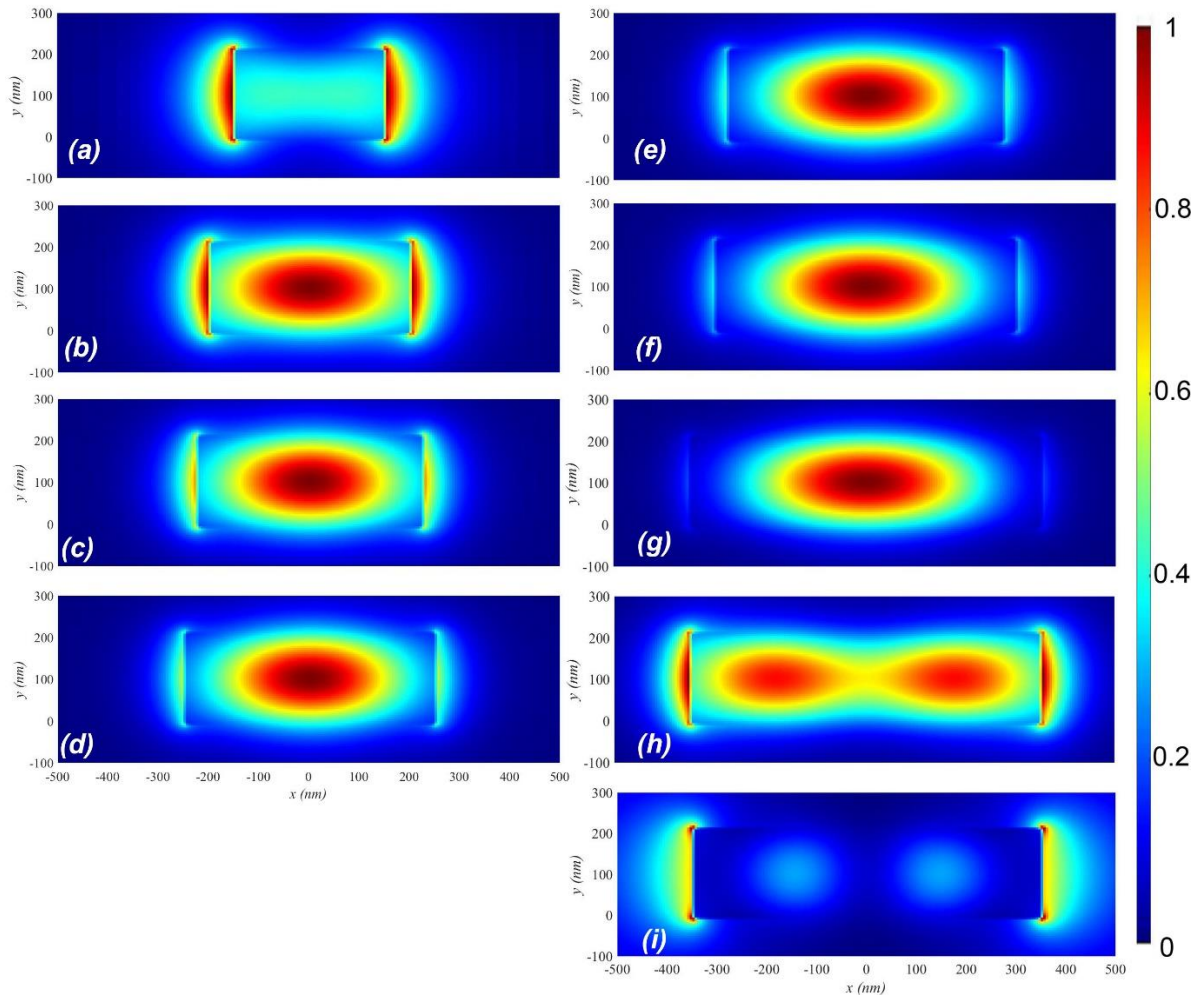


Figure 4.10 Normalized E field intensity of TE modes of 1546 nm light wave for 220nm thick SOI waveguide with width sweeping from 300 nm to 700 nm; (a) TE0 of $W = 300$ nm, (b) TE0 of

$W = 400 \text{ nm}$, (c) TE0 of $W = 450 \text{ nm}$, (d) TE0 of $W = 500 \text{ nm}$, (e) TE0 of $W = 550 \text{ nm}$, (f) TE0 of $W = 600 \text{ nm}$, (g) TE0 of $W = 700 \text{ nm}$, (h) TE1 of $W = 700 \text{ nm}$, (i) TE2 of $W = 700 \text{ nm}$.

To calculate the dispersive effective index n_{eff} and mode area A_{eff} , the A_{eff} is calculated by equation 4.8 based on the mode profile data obtained by the Lumerical eigenmode solver. Parametric sweep along the wavelength band from 1450 to 1650 nm for TE0 mode with width from 400 to 600 nm is performed, and the sweeping step is 50 nm to leave sufficient tolerance for fabrication. Figure 4.11 illustrates the n_{eff} and A_{eff} versus wavelength. It is seen that the effective index generally decreases with increasing wavelength. The effective index difference between 400 nm and 450 nm at same wavelength is larger than the difference between 550 nm and 600 nm, that suggests the effective index of mode is saturated with increasing width, or the cross-sectional area, this trend is witnessed at TE0 curve in Figure 4.9 as well. Also, the index of a narrow waveguide drops faster than a broader

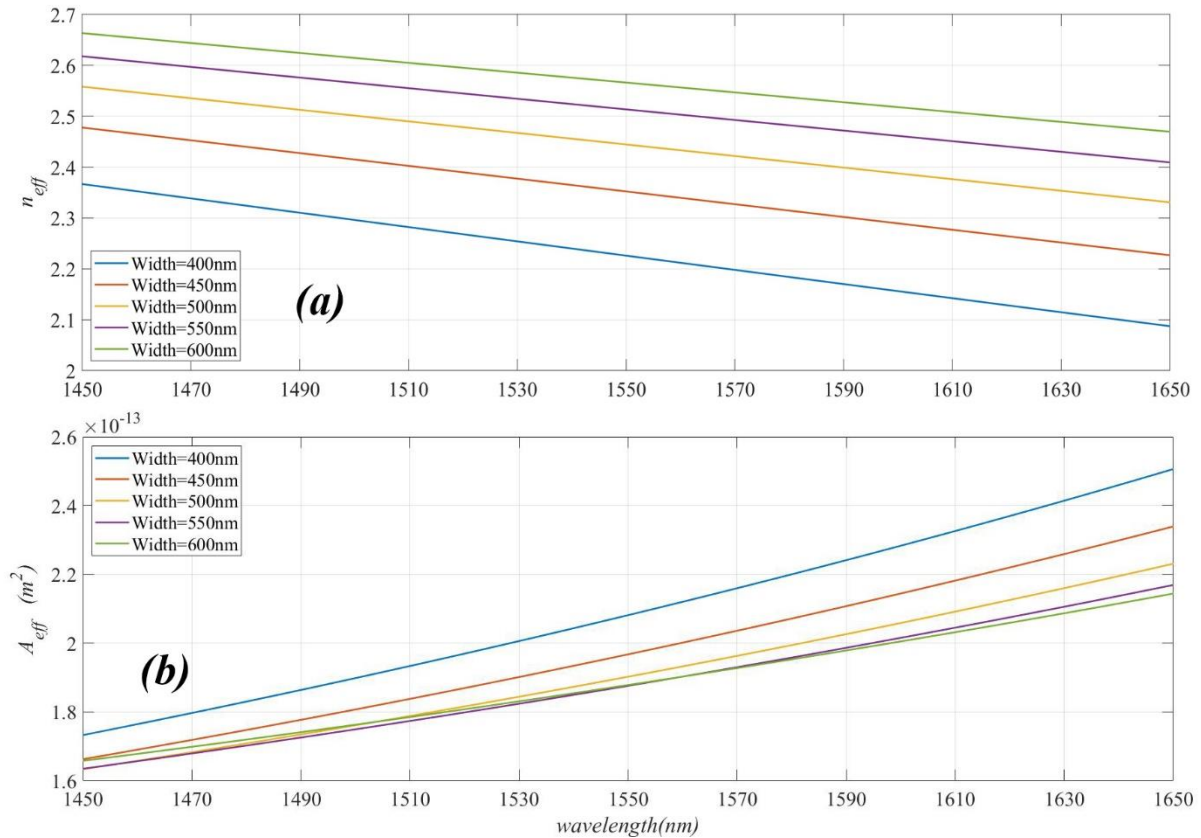


Figure 4.11 Effective index and mode area of TE0 mode of strip waveguide with different width (a) effective index versus wavelength (b) effective mode area versus wavelength.

waveguide because more energy will concentrate on the side wall and propagate in the cladding layer with wavelength rising, which leads to the drop of n_{eff} . As for the effective mode area, it also be seen a limitation with increasing width. A_{eff} drops with increasing of width since

narrow waveguide has more energy propagated through the low confinement area, the cladding, which significantly enhances the effective mode area. With increasing width, more energy will be guided in the silicon core, and this will reach a limit when all energy is confined in the core.

4.4.2 Dispersion modulation and FWM conversion calculation

The last section discussed the mode simulation and analysis of a strip SOI waveguide, with the obtained n_{eff} and A_{eff} , the high-order dispersion is calculated, and phase mismatch is analysed in this section. Then the FWM conversion is calculated through CNSE and small signal approximation methods introduced in chapter 4.3.5. Table 4.1 lists all parameters adopted for the FWM calculation.

Table 4.1 Parameters for dispersion modulation and FWM simulation of SOI waveguide.

symbol	meaning	value	unit
λ_p	Pump wavelength	1546	<i>nm</i>
λ_s	Signal wavelength	1450 – 1650	<i>nm</i>
n_2	Non-linear refractive index	5.59×10^{-18} [155]	m^2/W
τ_{eff}	Carrier lift time for FCA	1.1×10^{-9} [156]	<i>s</i>
β_{TPA}	TPA coefficient	9.95×10^{-12} [155]	m/W
P_{pump}	Input pump power	6~18	<i>dBm</i>

Firstly, the second and fourth-order dispersion profile is calculated according to equation 4.18, and linear phase mismatch is further calculated with equation 4.17. Figure 4.12 shows β_2 , β_4 and linear phase mismatch Δk_{Linear} versus the signal light wavelength. The second-order derivative of the propagation constant β_2 can also be reformed to the commonly used Group Velocity Dispersion (GVD) by the following equation,

$$D = -\frac{2\pi c\beta_2}{\lambda^2} \quad (4.25)$$

The GVD versus signal wavelengths is shown in Figure 4.13(a). According to equation 4.17, the linear phase mismatch is mainly depending on β_2 , it is noticeable the 500 *nm* width waveguide performs most flat GVD with two zero-GVD points in the whole signal band, and

the two zero dispersion point is symmetrical with respect to the pump wavelength. The minimum value of β_2 , or the maximum value of GVD experiences a trend of red shifting and becomes flatter with increasing waveguide width. This is because the dispersion sensitivity of the waveguide is reducing due to the reduction in energy density caused by the increased cross-sectional area of the waveguide. β_4 of different widths generally show similar rising trends along the wavelength. Apparently, the slope of β_4 of narrow waveguide is much higher than a wide waveguide, which further deteriorates the phase mismatch of a narrow waveguide. Figure 4.12(c) is the original value of linear phase mismatch, but the trend is not very clear and demanding to be distinguished due to the data scale and overlapping of some curves with others, so the linear phase mismatch is reorganized in Figure 4.12(d) as $\Delta k_{Linear} \cdot L/\pi$, the waveguide length here is set as 1 cm. Foster suggests that the range of the magnitude of this transformed linear phase mismatch between $\pm\pi$ is approximately corresponding to the conversion band of FWM [123]. Obviously, the 500 nm width is predicted to have the widest conversion band, which will be 1470 to 1630 nm. The rest widths are generally showing a parabolic shape curve and are not promising for a wide-band FWM conversion. It is seen that the mouth direction is generally rotating contra-clockwise with increasing width; the fourth-order dispersion is correlated with this trend. The 450 nm and 550 nm waveguide also possess a very flat 2nd dispersion curve. However, because they hold only one zero GVD point in this signal band, coupled with the displacement between their minimum GVD point and pump wavelength, their linear phase mismatch curve is unsymmetric, which suggests their conversion is not broad as the 500nm width waveguide.

The conversion efficiency is then calculated by CNSE and small signal approximation methods, respectively. The parameter used for the simulation is listed in Table 4.1. Figure 4.13 illustrates the GVD, phase mismatch, and conversion efficiency versus signal wavelength. As shown in Figure 4.12(b), compared with the linear phase mismatch, introducing nonlinear terms does not change the phase mismatch trend of all widths in the short band region since the non-linear term is a constant value for different widths, respectively, according to equation 4.19. Figure 4.13(c) and (d) are the conversion efficiency spectrum calculated by CNSE and small signal approximation, respectively, the coupling length is 10 mm here, and the pump energy is set as 15 dBm. In general, the conversion calculated by both methods agrees with the linear phase mismatch result; 500 nm width waveguide displays the largest conversion band in both spectrums. Particularly, the conversion band obtained by a small signal approximation of 500 nm width prove the $\pm\pi$ range prediction before, as it is shown in Figure 4.13(d),

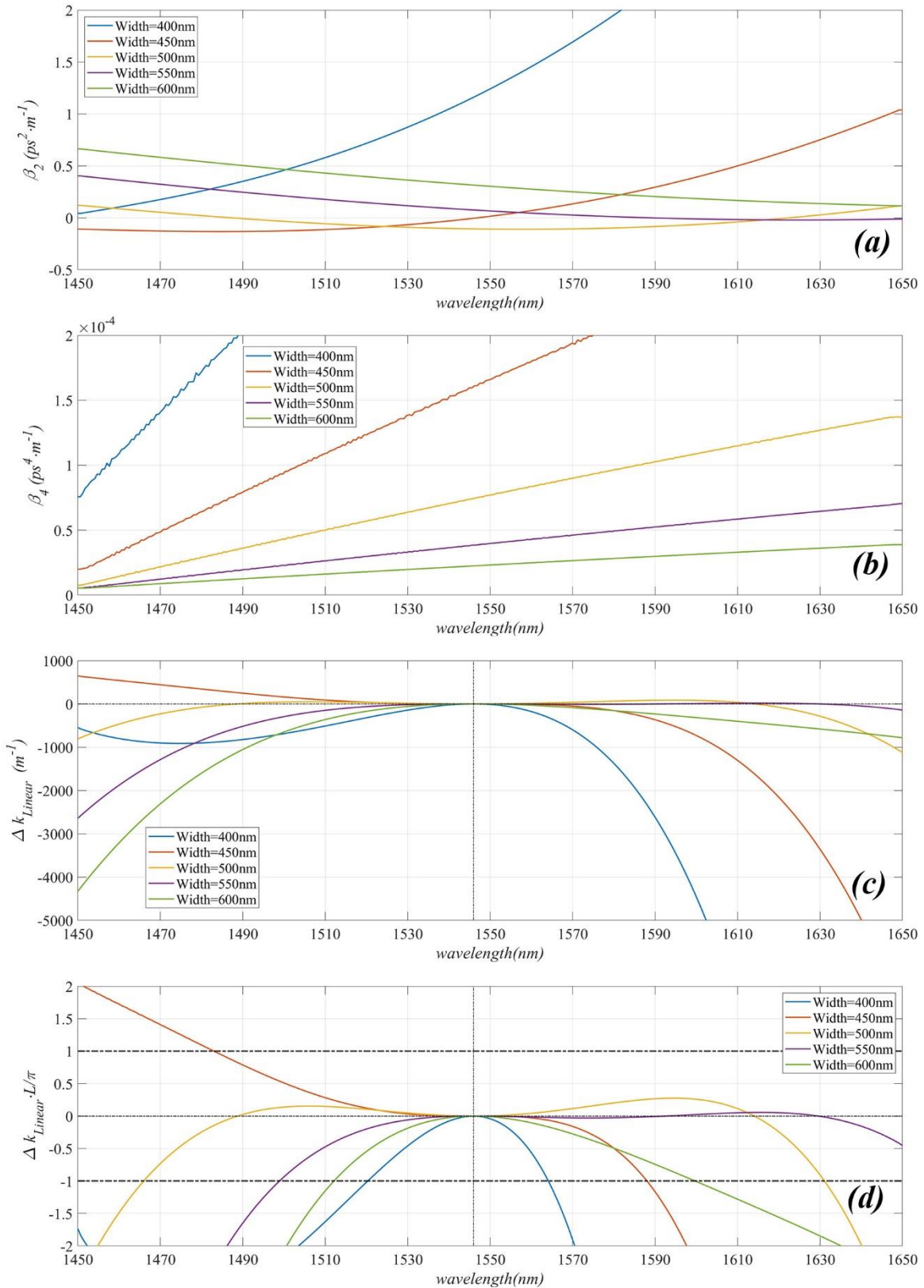


Figure 4.12 The high order dispersion and linear phase mismatch versus signal wavelengths, the pump wavelength is 1546 nm. (a) Beta 2 versus signal wavelengths, (b) Beta 4 versus signal

wavelengths, (c) Linear phase mismatch versus signal wavelengths, (d) $\Delta k_{Linear} \cdot L/\pi$ versus signal wavelengths

the yellow curve for 500 nm has a -3 dB conversion band around 1470 to 1630 nm. Both the two-neighbour width of 500 nm, 450 nm and 550 nm have a wide but unsymmetric conversion band as the expectation, the conversion band of 450 nm is biased towards the short wave band, on the contrary, 550nm is biased towards the long wave band. Therefore, the 500 nm width waveguide is adopted for the next step length sweeping. Obviously, the conversion efficiency derived by CNSE of every width is lower than the result of Small Signal Approximation, and the conversion bands of CNSE are narrower than Small Signal Approximation. That is because the CNSE solution considered the linear absorption of silicon material and non-linear absorption, including TPA and derived FCA, which suggests the result from CNSE is more reliable for the coupling length sweeping.

The longitudinal length of the waveguide is another essential factor that would influence the conversion efficiency and band. It is equal to the coupling length of FWM in the waveguide. For the fabrication process, the length of the SOI waveguide for ideal conversion needs to be identified. Equation 4.22 also shows that the solutions of CNSE are amplitudes of the different wave, or equivalently, the conversion efficiency, which can be reorganized to a function with respect to the coupling length L , and equation 4.20 indicated the conversion calculated by small signal approximation also could be seen as a function with respect to the coupling length L . Therefore, a sweeping length simulation towards the coupling length is implemented, and the results are shown in Figure 4.14. The length sweeping results of the CNSE and Small Signal Approximation are in Figure 4.14(a, b), respectively. In Figure 4.14(a), the max conversion efficiency increases with the growth of length firstly and reaches the maximum around 2 mm, then starts dropping since the absorption of waveguide. As for the results of small signal approximation, the max conversion efficiency is continuously climbing with increasing coupling length. Since a small approximation does not consider the absorption. For conversion derived by both methods, the conversion bands are shrinking with increasing coupling length.

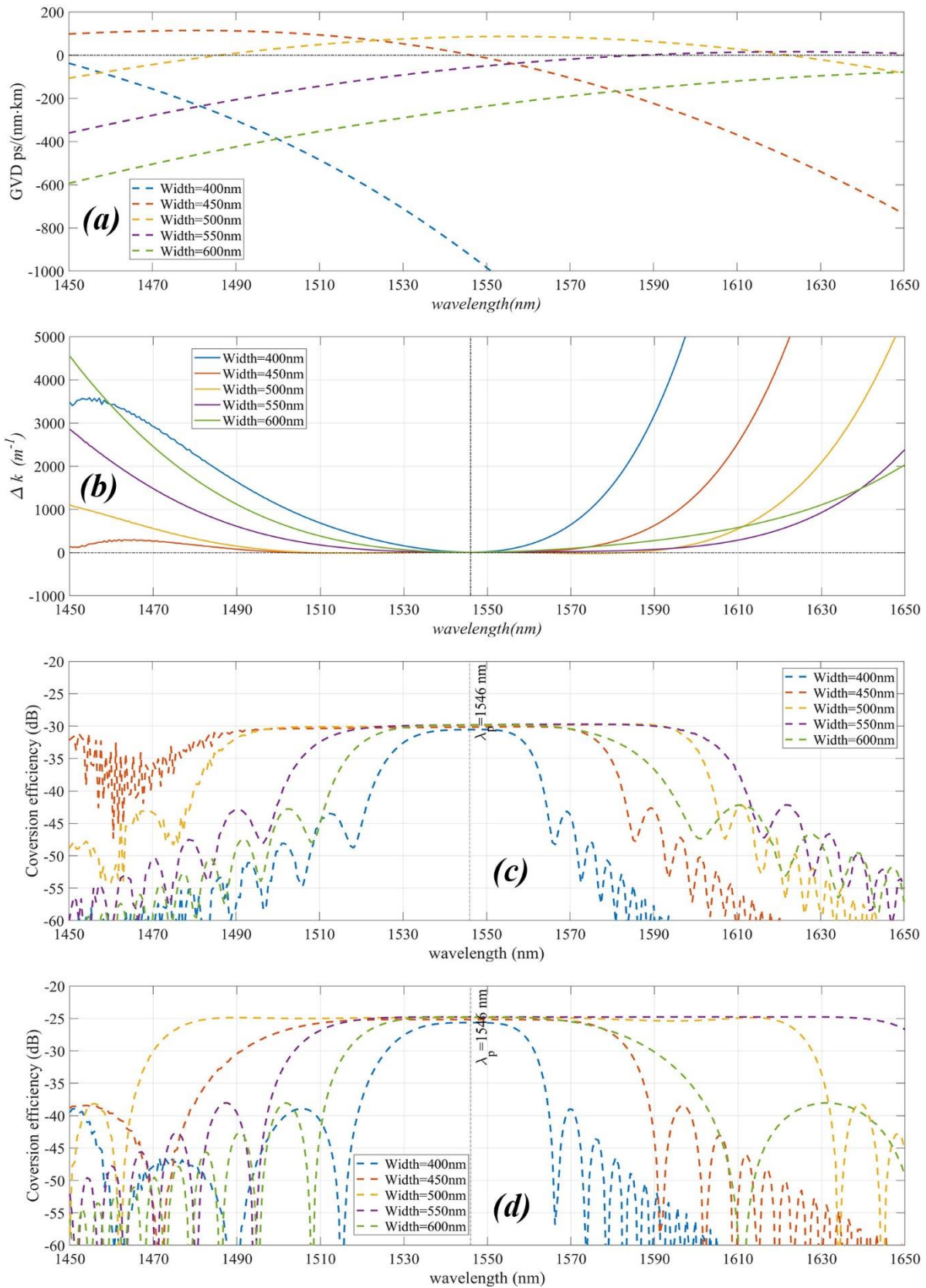


Figure 4.13 (a) The GVD of different width SOI waveguides with 220nm height. (b) the Phase mismatch versus signal wavelength. (c) the conversion efficiency calculated by the CNSE method. (d)

the conversion efficiency is calculated by Small Signal Approximation method. Here the pump energy is set as 15 dBm, the coupling length is 10 mm, and the pump wavelength is 1546 nm.

A finer length sweeping is conducted with CNSE to investigate the influence of coupling length in detail; the result is shown in Figure 4.15, where the left axis and blue curve is the maximum conversion efficiency with varying length, and the right axis and red curve is the Full Width of Half Maximum (FWHM) of the conversion bandwidth along different coupling lengths. The conversion bandwidth is the FWHM of the central band of the conversion spectrum. The pump energy and wavelength for the sweeping operation are set as 15 dBm and 1546 nm respectively. The results show that the conversion efficiency will increase as the coupling length increases, and the max conversion power is reached at 2.3 mm around -23.3 dB.

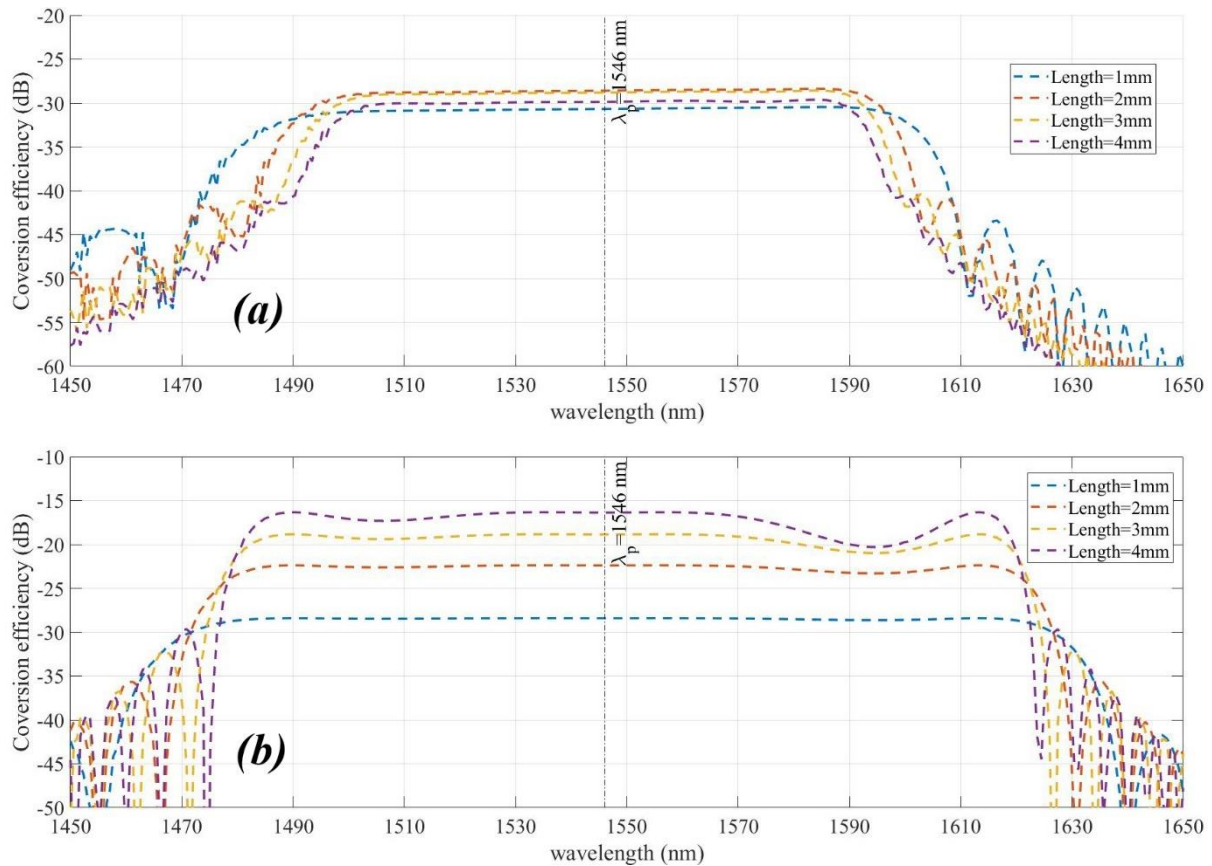


Figure 4.14 The length sweeping of conversion efficiency, the width is 500 nm, the pump power is 15 dBm at 1546 nm (a) the result of CNSE versus signal wavelength of different coupling length (b) the result of small signal approximation versus signal wavelength of different coupling length.

However, the coupling length cannot be infinitely long since the linear absorption is also enhanced by expanding the coupling length. The conversion efficiency will be reduced by continuously increasing linear absorption. As seen in the figure, the conversion efficiency decreases after the maximum point. Besides, the conversion bandwidth decreases dramatically

with increasing length. Therefore, a trade-off between the conversion band and efficiency for practical application is inevitable.

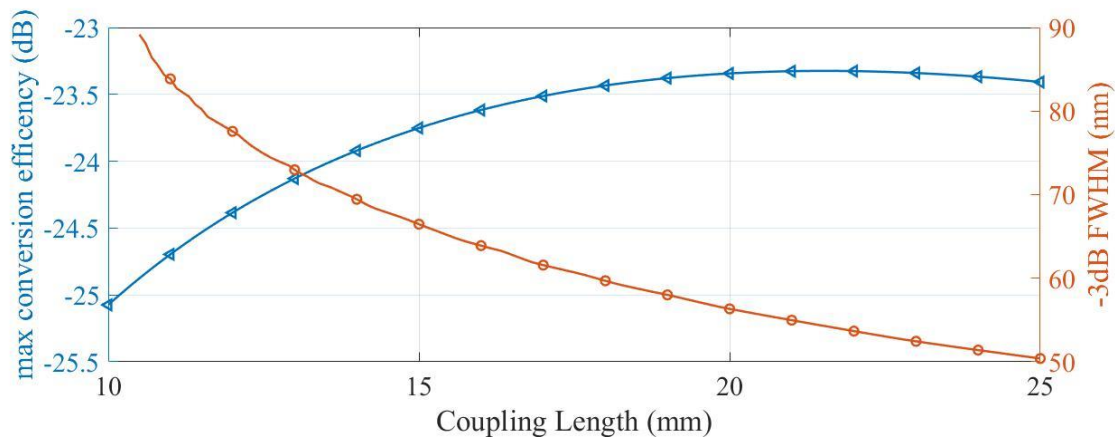


Figure 4.15 The fine length sweeping result solved by CNSE, the width is 500 nm, the pump power is 15 dBm at 1546 nm, the max conversion efficiency and conversion bandwidth versus coupling length is shown.

Another factor that could influence the conversion efficiency is the pump power, pump energy sweeping simulation is done with the small signal approximation method, and the result is shown in Figure 4.16. The conversion efficiency increases corresponding to the increasing pump power. This pump energy range of 6 dBm to 18 dBm is based on the source, and Erbium-Doped Fiber Amplifier (EDFA) is proposed to be used. A maximum -20 dB conversion is expected based on this simulation result when pump energy is 18dBm.

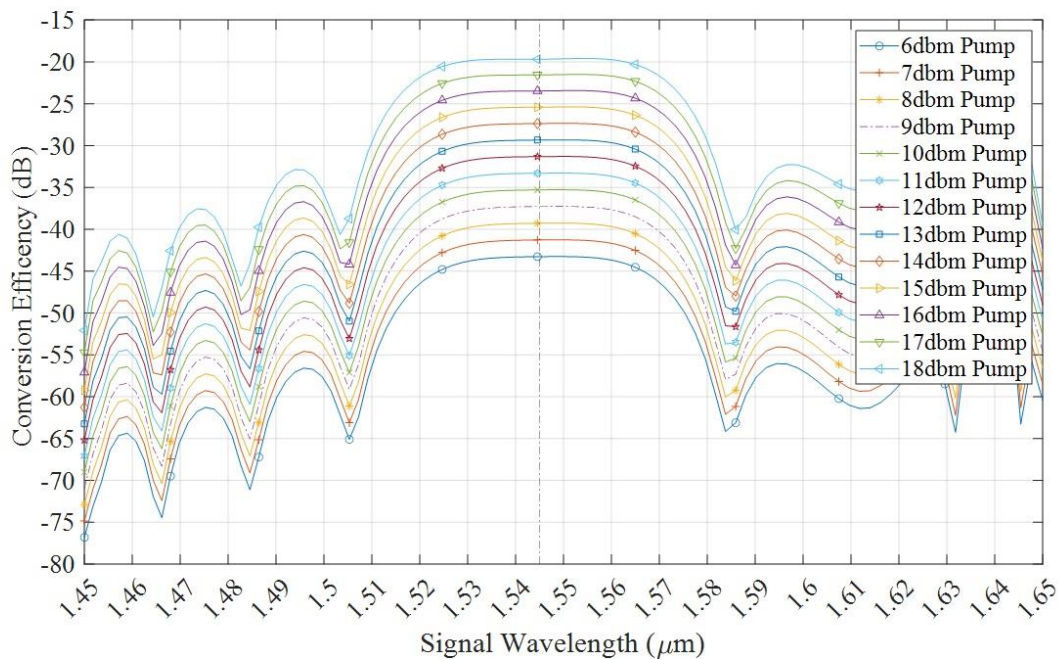


Figure 4.16 Conversion of different pump energy versus signal wavelength, where the width is 500 nm, length is 2.2 mm, and pump wavelength is 1546 nm.

Based on the simulation results, the waveguide with 500 nm width and 220 nm height waveguide is employed for fabrication. Two batches of waveguides were proposed to fabricate, the first batch with a 15 mm coupling length and the second batch with a 20 mm coupling length. The maximum coupling length was not chosen based on the fabrication side's advice. It is compromising to fabricate more waveguides on a single wafer. Indeed, the coupling length influences the conversion efficiency, but the impact is not that large, so a little loss of the conversion efficiency for more chips is acceptable. Both the 15 mm and 20mm coupling lengths still illustrate acceptable conversion efficiency and bandwidth.

4.5 Fibre-to-waveguide coupling

The FWM conversion efficiency is highly dependent on the pump energy, meaning the pump light's input energy into the waveguide must be as high as possible. The critical problem of fibre-to-waveguide coupling is the big difference between the cross-sectional scale of fibre (for SMF, 8 μm diameter) and nano waveguide (500 nm * 220nm for the proposed design), which brings them around 0.5 μm and 9 μm mode field diameter (MFD), respectively, resulting in -20 dB insertion loss with direct edge coupling in estimate with the mode overlapping theory. The coupling from the waveguide to the fibre or inverse significantly limited the application of PICs. To date, all proposed fibre-to-waveguide coupler structures can be categorized as grating couplers, lens couplers and taper couplers (Edge couplers).

A Taper coupler

The taper coupler, or Edge coupler, indicates that the fibre and waveguide are aligned in a line, and the energy is input directly from the edge or facet of the waveguide. The two typical taper couplers are forward and inverse taper couplers, both formed by a taper structure made of the core material. Figure 4.17 (a) and (b) show the schematic of typical forward and inverse taper couplers, respectively. The basic idea of forward taper is straightforward, fabricating a taper made of the core material with two ends area that matches the fibre's cross-section and waveguide's cross-section, respectively, so that the guided mode size is compressed or enlarged with propagation along the longitudinal direction (x direction in Figure 4.17 (a)) of taper. The fibre end of the forward taper usually is a facet match with the dimension of single mode fibre or lensed fibre (around 2~8 μm), and the waveguide end is the same size as

waveguide. The first horizontal taper coupler was proposed by Day et al. in 2003. The best coupling efficiency they achieved was -0.5 dB [157]. In 2003, Sure et al. reported a vertical taper coupler and achieved -2.6 dB coupling efficiency [158], and Fijol et al. fabricated another 3-dimensions taper coupler in the same year and achieved -0.63 dB coupling efficiency [159]. However, the process required for these forward taper couplers are relatively complicated, which is not suitable for mass production and wide application, besides, the waveguide suitable for forward taper coupler are relevantly large size (few micrometres level), since a smooth and continuous taper shape from few microns to sub-wavelength size is difficult to fabricate, the production yield is poor.

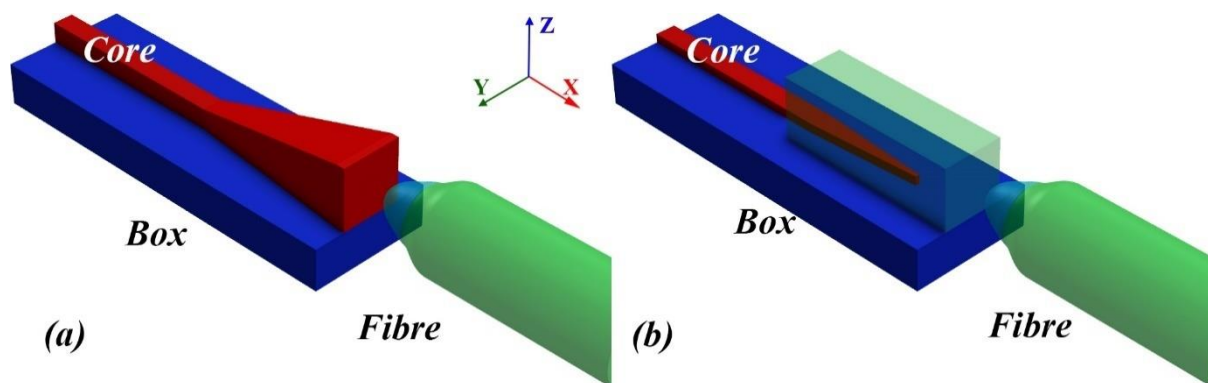


Figure 4.17 Schematic of typical edge coupling taper coupler. (a) Forward taper coupler. (b) Inverse taper coupler.

As for the inverse taper, its working scheme is different to the forward taper. It utilizes the mode match principle for designing. The narrower end, or tip end, typically with a dimension around 100 nm, faces the fibre end, as seen in Figure 4.17 (b). The larger end of the taper is the same size as the waveguide and is linked with the waveguide. With the narrowing core towards the tip end of the inverse taper, an increasing part of energy propagates in the cladding layer, which forms evanescent wave surroundings on the surface of the core waveguide. Therefore, the effective mode area is enlarged with a narrow waveguide at the tip side, further matching the fibre's mode area. The inverse taper coupler is suitable for small-size waveguides, for example, 220 nm or 340 nm thick SOI waveguide. Almeida from Cornell University proposed the first nanometre-level inverse taper coupler in 2003, which achieves around -3 dB coupling efficiency [160]. In 2002, Shoji et al. proposed a polymer-based inverse taper coupler for SOI waveguide and achieved -1 dB coupling efficiency; they further improved the coupling efficiency to -0.7 dB in 2008 [108].

Since both the forward and inverse taper are edge coupling, the injection facet and fibre-waveguide alignment conditions significantly influence the coupling efficiency. The facet condition is influenced by wafer slicing, facet polishing, and coating, all of which need to be careful during the fabrication and further complicate the process.

B Lensed coupler

The lensed coupler utilizes a dedicatedly designed prism or lens to focus the light into the waveguide. In 2004, Lu et al. invented a prism coupler with -1.55 dB coupling efficiency [161], but this external coupling structure is unsuitable for compact integration. Qian's team proposed a Gradient-Index (GRIN) lens for the coupler and achieved -1.08 dB coupling efficiency [162], but this structure requires extremely precise fabrication and fibre-coupler alignment.

C Grating coupler

The grating coupler based on the diffraction effect is another commonly used coupling structure on the SOI platform to date. Figure 4.18 shows a typical layout of a grating coupler and its cross-sectional view (XoZ plane). The incident light P_{in} is injected quasi-vertically into the grating plane, the interaction of guided mode and grating mode eventually guides the light energy into the waveguide. The grating coupler has more tolerance for alignment thanks to the out-of-plane coupling structure. But the coupling efficiency is limited by three irrelevant propagation directions, including transmission through the grating P_{sub} to substrate, reflection from the grating plane P_r , and diffraction to the opposite direct P_{wr} , all these three directions lead to losses, only diffraction to the core direction P_w can be coupled in. Besides, since grating is wavelength sensitive, the coupling band of the grating coupler is relatively poor. In 2002, Tailaert invented the first grating coupler for GaAsAl oxide waveguide [163] and obtained -4.6 dB coupling efficiency, and the fibre is tilted for 8 to 10 degrees normally to avoid the 2nd order reflection. Then they optimized that design and achieved -3 dB coupling efficiency with an attached cladding layer made of silicon on top of grating in 2006 [164]. Typically, there is a big difference between the simulation results and experimental results of insertion losses of grating couplers, and this requires to be addressed by better fabrication process [165, 166]. As for the conversion band, few works about a chirped grating structure were proposed, which is supposed to enlarge the coupling band with a variable grating period [167, 168]; the widest -1dB coupling band obtained via this method is around 100 nm [169]. Although the grating coupler still needs optimization through both fabrication and design, it

still is widely applied due to high compatibility with the CMOS process, mode tolerance for alignment, and less damage on the waveguide.

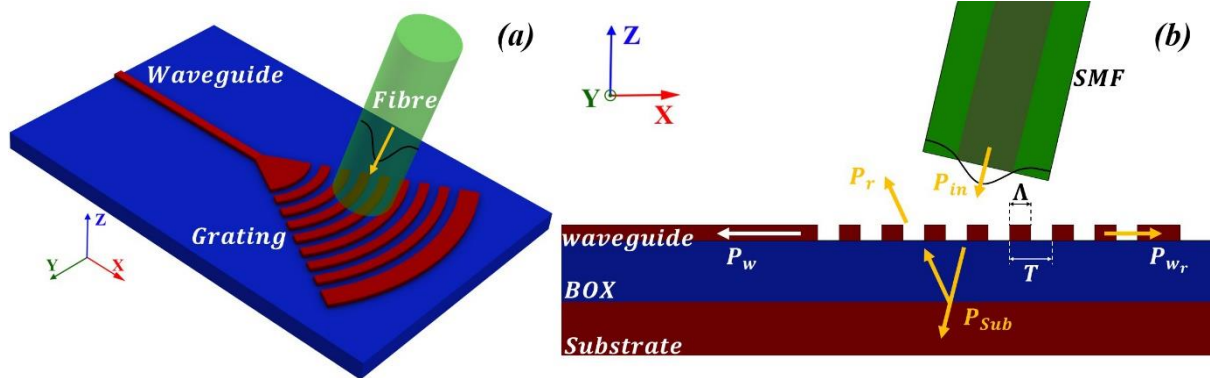


Figure 4.18 (a) The schematic of a grating coupler and the four propagating directions in the grating coupler. (b) The cross-section (from plane XoZ) of the grating coupler.

As mentioned before, the insertion loss is the object of designing a fibre-to-waveguide coupler, and the insertion loss is composed of propagation loss, Fresnel reflection loss, miss alignment loss, and mode mismatch loss. The propagation loss is dominated by material, the reflection loss can be reduced by coating or related techniques, and the miss alignment loss can be relieved by v-groove or other mechanical fixation structure. With the other three factors being solved ideally, the mode mismatch loss takes a prominent part of the total insertion loss, and this factor is determined by the design of fibre to waveguide coupler. The mode matching loss mainly depends on the mode difference between the inlet (fibre side) and outlet (waveguide side) and vice versa. The coupling efficiency η is given by an overlap integral equation between waveguide and fibre mode.

$$\eta = \frac{\int E_w(x, y)E_f(x, y)dxdy}{\int E_w^2(x, y)dxdy \int E_f^2(x, y)dxdy} \quad (4.26)$$

Where E_w and E_f are modes of waveguide and fibre, respectively. SMF usually possess a gaussian like centrosymmetric mode profile with a micrometres level diameter. However, the mode of the SOI waveguide is not centrosymmetric and far smaller than the fibre mode. As can be seen in Figure 4.10, such a mismatch leads to significant insertion loss. Therefore, a well-designed coupler plays a role as a bridge between fibre and waveguide, which must be able to change the mode size gradually and continuously from fibre to waveguide sides and maintain the single mode profile during the whole process as much as possible.

The waveguide adopted in this project is 220 nm SOI. Therefore, the candidates for coupler design are inverse taper and grating coupler. The rest of chapter 4.5 introduced the

design simulation based on Lumerical FDTD and Eigen Mode Expansion solver (EME) of both the grating coupler and inverse taper coupler. One design of grating coupler and two inverse taper couplers are proposed. Additionally, the impact of lensed fibre on coupling efficiency is discussed in the last section of this chapter based on the simulation results.

4.5.1 Simulation of the grating coupler

The simulation of a grating coupler is conducted along the model shown in Figure 4.18 (b). The period T and material filled length Λ are 750 and 375 nm respectively, the fill factor is 0.5. These values are taken based on the proposed working wavelength. The waveguide dimension is selected as 500 nm width and 220 nm thickness respectively. Without particular emphasis, the waveguide dimension in the rest of this chapter for coupler design is all this dimension. A PECVD silica layer covers the surface of the grating, unlike the mode analysis for FMW in chapter 4.4.1, the PECVD silica index here origins from Pan’s et al. experimental result [170].

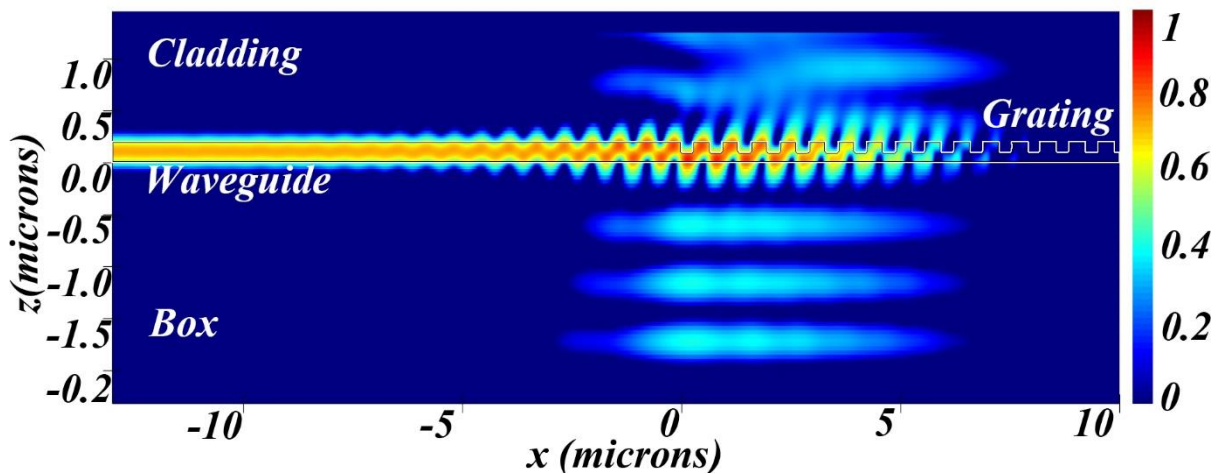


Figure 4.19 Normalized E field of cross-section (from XoZ plane) of the grating coupler, the grating period is $T = 750 \text{ nm}$, $\Lambda = 375 \text{ nm}$. Incident wavelength is 1548 nm.

Figure 4.19 illustrates the normalized E field of the grating coupler from a cross-section view (XoZ). The simulation is conducted using by Lumerical FDTD solution. Since the gating coupler is symmetrical with respect to the XoZ plane, the simulation is simplified to the 2D-FDTD simulation on the XoZ plane. As can be seen, incident light is injected from the top at x range 0 to 5microns with an angle of 11 degrees, a significant amount of light passes through the grating and is guided to the substrate through the box layer, and there is no reflection from the bottom since the simulation boundary is set as PML and the substrate layer is not included in this simulation model. As for the waveguide-cladding interface, since the waveguide index

is much higher than the cladding, no obvious reflection from this interface is observed. Despite the energy transmitting to the substrate, the main part of the incident energy is correctly coupled into the waveguide direction. And thanks to the incident angle, which could eliminate the 2nd order reflection from grating and waveguide, there is no clear reflection along the opposite direction P_{wr} of waveguide be observed in the figure.

A wavelength sweeping simulation is then implemented with the proposed model to investigate the broadband coupling efficiency of such a grating coupler, and the result is shown in Figure 4.20; the -3dB coupling band for this grating coupler is around 20 nm with centre at 1548 nm, and its minimum insertion loss is around -2.5 dB.

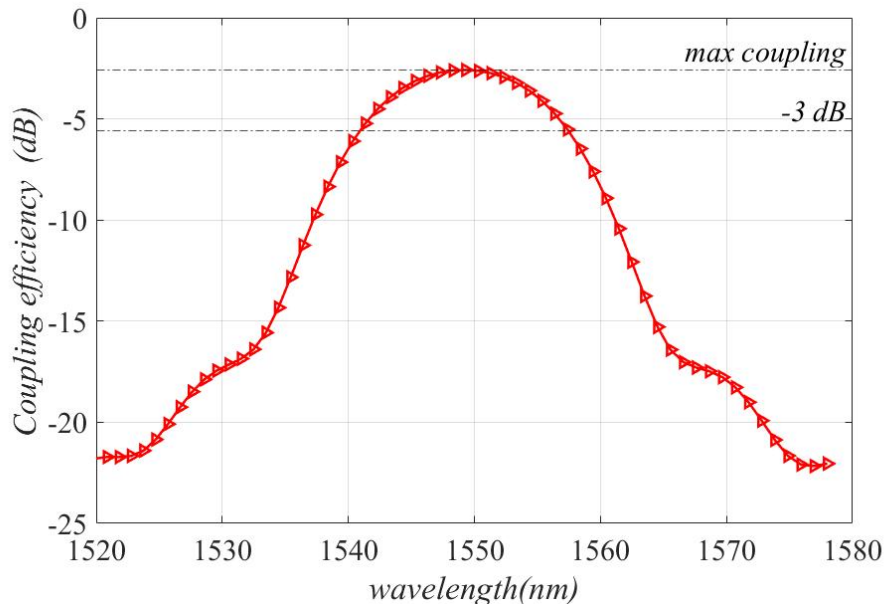


Figure 4.20 The 2D-FDTD simulated coupling efficiency of a grating coupler for 220 nm thick SOI waveguide, the grating period is 750 nm, and the grating fill factor is 0.5.

No further optimization was conducted for the grating coupler since one of the requirements of this project is to fabricate as much as possible waveguide on the wafer, the grating coupler occupies more space than the taper coupler, and the alignment of the grating coupler without package process is potentially complex than the edge couplers due to out of plane alignment and rotation of fibre.

4.5.2 Design and simulation of edge coupler I: SU-8 covered taper coupler

To control the technique risk of the whole project, an inverse taper coupler with SU-8 outer waveguide is mainly focused on since a similar layout was proved as a low-risk plan

[104], and the process polymer outer waveguide is relevantly cheap and fast. The schematic of this SU-8 coupler is shown below in Figure 4.21. The end of the silicon waveguide is tapered for the mode shrinking or enlarging. For better mode matching with lensed fibre, a more oversized or outer waveguide made by polymer SU-8 covers the taper part of the silicon waveguide. For this coupler, the design of both the taper and outer waveguide is crucial. The taper should have sufficient length to avoid dramatic change in effective mode area; as for the outer SU-8 waveguide, it should dimensionally match the lensed fibre beam size, or waist size as much as possible, while maintaining a similar mode profile in shape with the TE₀ mode of designed SOI waveguide.

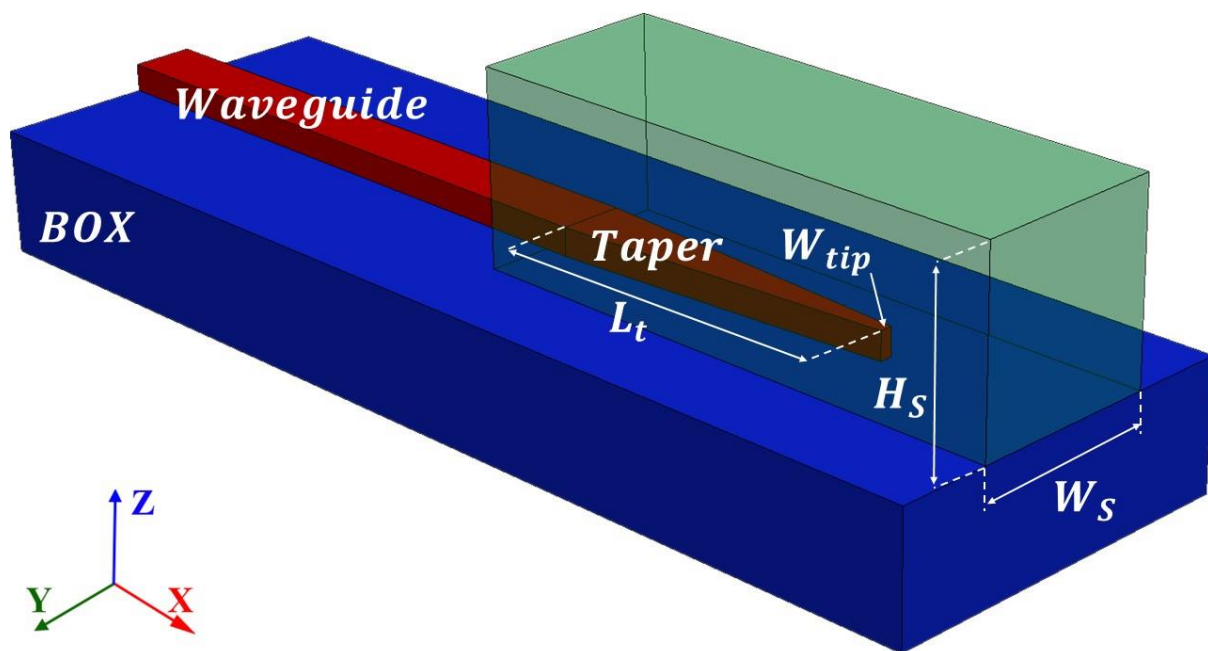


Figure 4.21 The simulation model of the Su-8 taper coupler.

Like the SOI waveguide, the EIM analysis is first implemented on the SU-8 outer waveguide. The beam waist of one of the lensed fibres proposed to be used for the experiment is $3 \mu m$, therefore the width W_s of SU-8 outer waveguide is set as $3 \mu m$ to match the beam size. Since the width-to-thickness ratio of the designed SOI waveguide is more significant than 1 (500:220), therefore the thickness H_s of SU-8 should be smaller than the width to ensure a similar mode shape. The index of Su-8 is dynamic and dependent on factors, including polymerization temperature, pressure, and exposure time [99] during the fabrication process. Thus, it is pretty challenging to be identified. Here the index adopted for this EIM simulation is based on the fitting equation proposed by Girault et al. based on their ellipsometer test result of SU8 film processed by a two-step thermal process [171]. The result of EIM is shown in

Figure 4.22, as it can be seen that the region of TE1 and TE2 cut-off corresponds to the thickness from $1.25 \mu\text{m}$ to $2.5 \mu\text{m}$. Because the proposed SOI is working with this mode area (as seen in Figure 4.9), therefore, to ensure best mode matching, this thickness range is employed for coupling efficiency simulation.

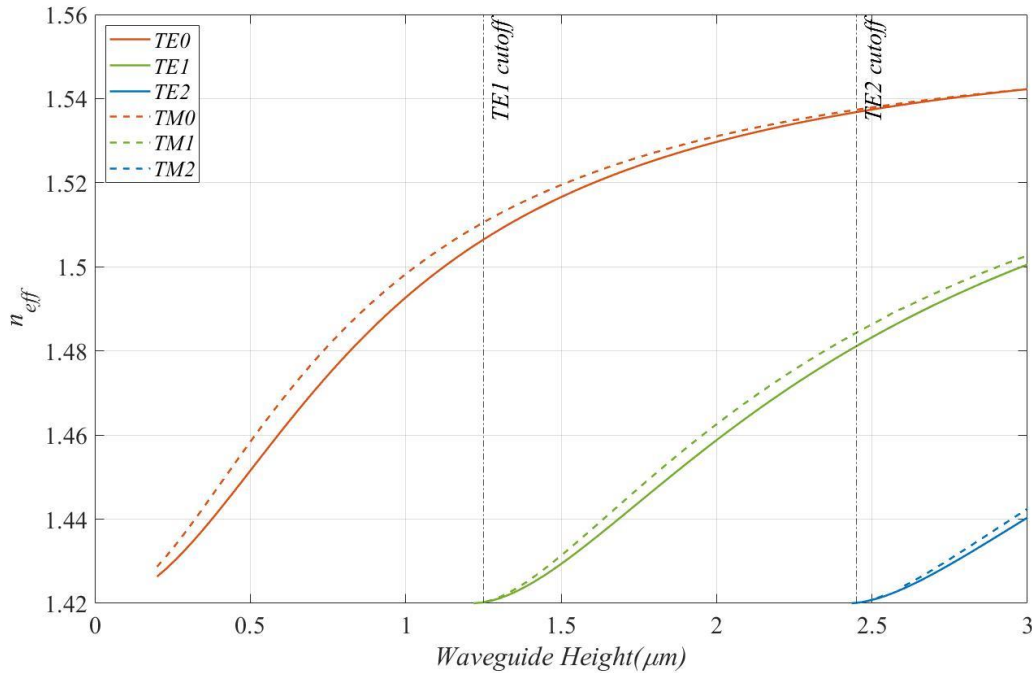


Figure 4.22 EIM calculated the effective index of modes of SU-8 outer waveguide. (Width $W_s=3 \mu\text{m}$, Thickness H_s sweeping from 0 to $3 \mu\text{m}$)

The coupling efficiency is solved by the EME solver in the Lumerical MODE solution. It is a faster simulation method based on frequency domain methods, which could calculate the coupling efficiency based on the mode overlapping between the eigenmode profile of two ports, namely the fibre and waveguide here. The result is shown in Figure 4.23. The tip width W_{tip} here is 80 nm . As it is shown, the coupling efficiency increases with a longer taper length L_t , for all SU8 Widths, the insertion loss reaches a minimum when the taper length L_t exceed $160 \mu\text{m}$. Particularly, the coupling efficiency of SU8 thickness at $1.5 \mu\text{m}$ (orange curve) show the highest magnitude along all taper length among all thickness simulated. It is seen that the highest coupling efficiency here is close to 0 dB. Therefore, the cross-section dimension of the SU8 outer waveguide is determined as $W_s = 3\mu\text{m}$ and $H_s = 2.5\mu\text{m}$. The reason for not using finer steps for thickness sweeping is that the thickness of SU8 is hard to be precisely controlled, many processes could influence the thickness, for example, spin coating, etching,

and washing. So, the thickness value $2.5 \mu\text{m}$ here is sufficient for a guideline for the fabrication side.

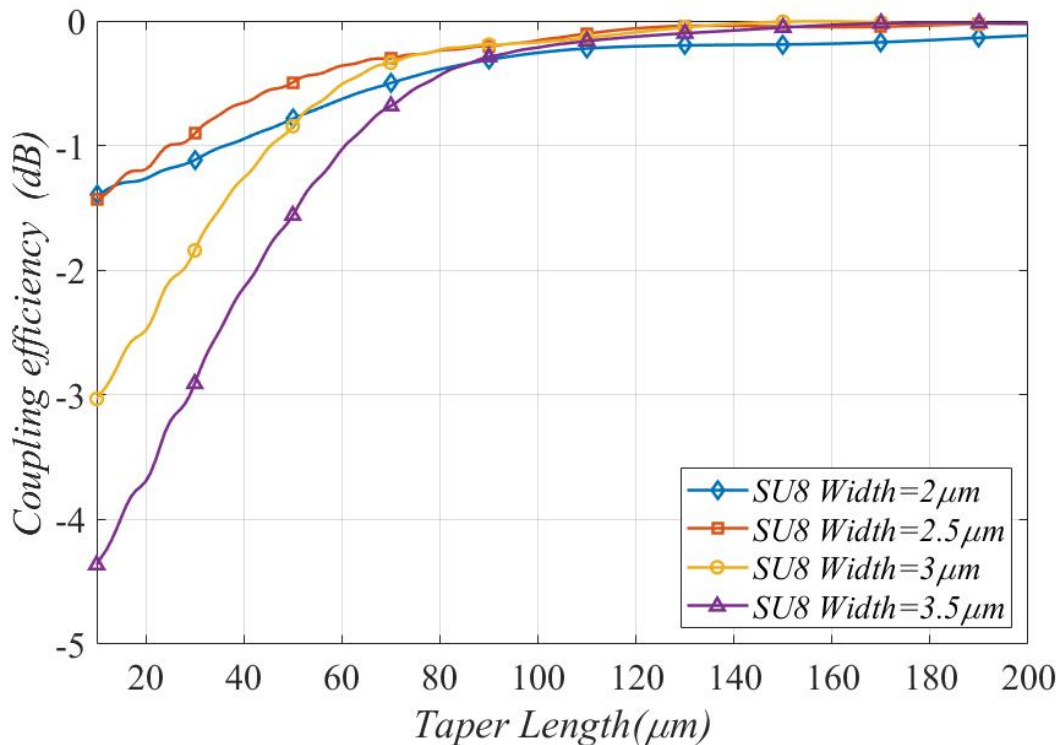


Figure 4.23 Coupling efficiency versus taper length of different Width SU8 waveguides. ($W_{tip} = 80\text{nm}$, $W_s = 3\mu\text{m}$, $\lambda = 1546\text{nm}$)

With the dimension of the SU8 and SOI waveguide determined, a 3D-FDTD simulation is performed to further verify the mode transforming process in the SU8 taper coupler. The normalized E field of the SU8 taper coupler from the top and side view is shown in Figure 4.24. The taper length adopted for this FDTD simulation is $50 \mu\text{m}$ (from $x = -25 \mu\text{m}$ to $x = 25 \mu\text{m}$), the taper length over $160 \mu\text{m}$ are not selected since they are hard to be shown due to the aspect ratio of their size, and the E field profile of $50 \mu\text{m}$ taper is sufficient to explain the principle of mode transforming. The distance between the tips end of SOI to the facet of SU8 is $20 \mu\text{m}$, and the length of SOI waveguide bonded with the taper at the bigger side is $20 \mu\text{m}$ as well. As it is seen in Figure 4.24 (a), the light is incident from the right ($x = 40 \mu\text{m}$) to left ($x = -40 \mu\text{m}$). The incident energy forms very strong evanescent field on the taper surface at x range from 10 to $-10 \mu\text{m}$, which indicates the energy is propagating on the surface of the taper. Remarkably, the evanescent field gets weaker with increasing taper width and with going deeper inside the coupler, which means more energy is coupled into the silicon waveguide. A stable waveguide propagating mode gradually shows up from $x = -10 \mu\text{m}$, and when exceeding

$x = -25 \mu\text{m}$, energy emerged in the SOI waveguide shows a stable guided mode. As for the side view, as it can be seen in Figure 4.24(b), the incident light beam is aligned to aim the centre axis of the SU8 waveguide for maximum coupling; the light firstly propagates as SU8's guided mode as been shown in x from 25 to 45 μm region. Then the light energy tends to concentrate on top surface of SOI taper around $x = 5 \mu\text{m}$, then a stable guided mode in SOI is gradually formed. In particular, energy leaking is observed on both the top surface and back surface of SU8. These boundaries are cladding-SU8 interfaces, and the material on both sides has similar refractive indexes.

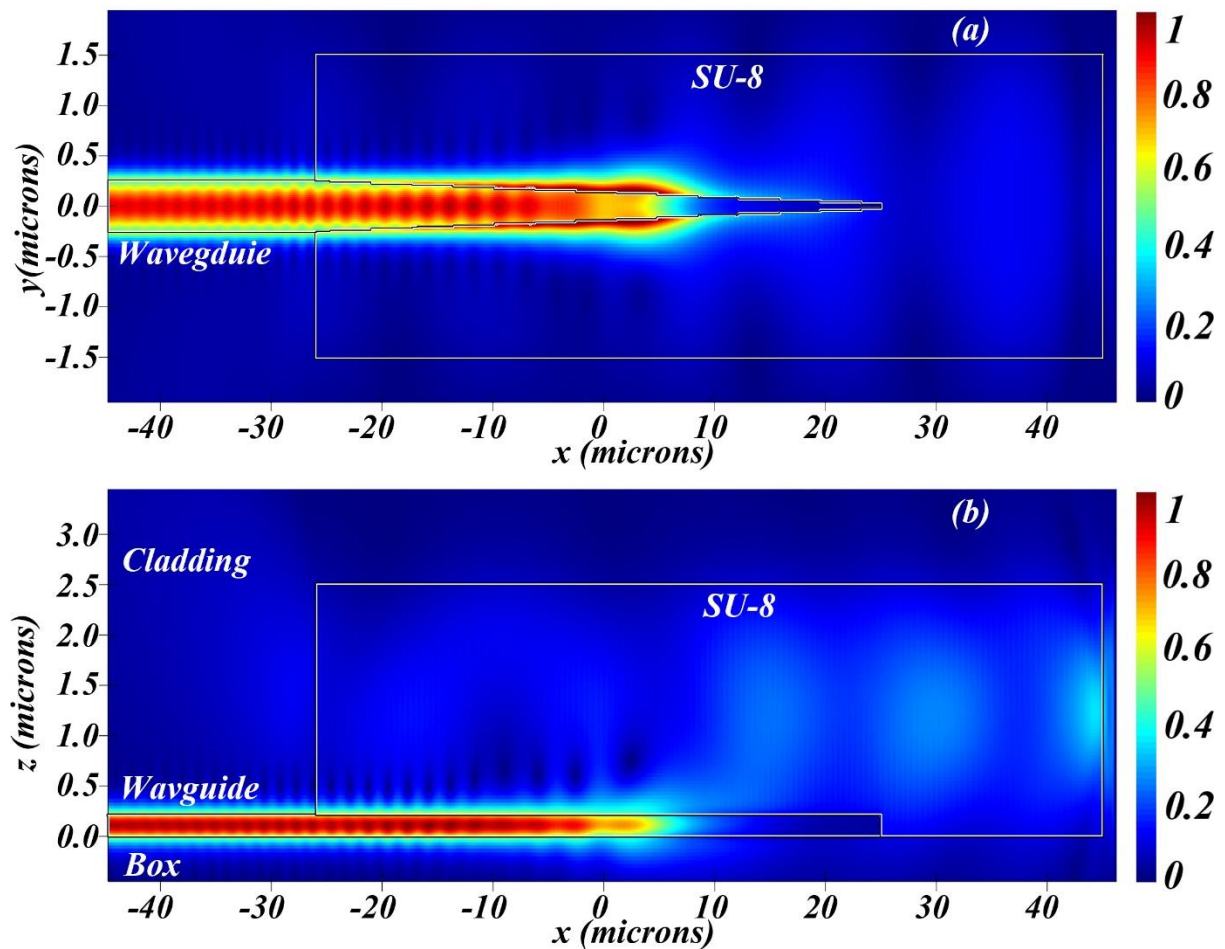


Figure 4.24 The Normalized E profile of SU-8 taper coupler ($W_t = 80\text{nm}$, $L_t = 50\mu\text{m}$, $\lambda = 1546\text{nm}$). (a) Top view (XoY plane). (b) Side view (XoZ plane)

The cross-section (YoZ plane) E field profiles at different propagating distances (X value) are shown in Figure 4.25. This set of images vividly illustrates the mode shrinking process. As seen, the light propagates with a single mode in the SU8 waveguide at $X=40 \mu\text{m}$, and part of mode leaking to the cladding layer is observed because this position is close to the facet of the SU8 waveguide and light just entered. As the light propagates deeper, a stable single mode is

witnessed at $X=30 \mu\text{m}$ just before interaction with SOI taper. Then the light starts to be influenced by both SU8 and SOI at $X=20 \mu\text{m}$, a tendency of concentrating to the side wall of SOI taper emerges. This tendency becomes more intensive at $X=10 \mu\text{m}$, where most of energy is confined on the side wall of the SOI taper, and only a weak E field is observed in the SU8 area. As the light continues propagating and the taper gets wider, a single mode like E field distribution becomes more evident, as shown in X from $0 \mu\text{m}$ to $-10 \mu\text{m}$. The taper section ends at $X=-25 \mu\text{m}$, eventually, a stable single mode propagation in SOI waveguide is formed as shown in Figure 4.25 (i) and (j) for the position at $X=-30 \mu\text{m}$ and $-40 \mu\text{m}$.

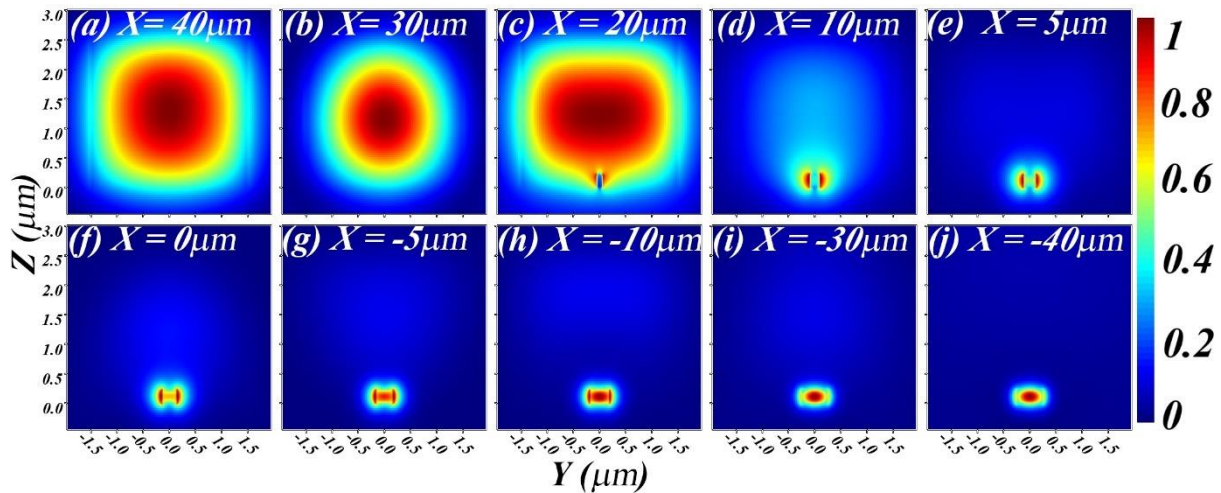


Figure 4.25 Normalized E field for different propagating distances, cross-section profile form Y o Z plane. (a) $X=40 \mu\text{m}$, (b) $X=30 \mu\text{m}$, (c) $X=20 \mu\text{m}$, (d) $X=10 \mu\text{m}$, (e) $X=5 \mu\text{m}$, (f) $X=0 \mu\text{m}$, (g) $X=-5 \mu\text{m}$, (h) $X=-10 \mu\text{m}$, (i) $X=-30 \mu\text{m}$, (j) $X=-50 \mu\text{m}$.

A broadband simulation and tip width sweeping are then conducted by EME solver, Figure 4.26 (a) is the coupling efficiency versus tip width W_{tip} , for all taper length, the maximum magnitude shows up at a tip width of 100 nm . Therefore, the tip width for the final design is determined as 100 nm . Figure 4.26 (b) is a broadband result for the SU8 taper coupler. As shown, for taper length over $180 \mu\text{m}$ the insertion loss on band from 1520 to 1580 nm is below -0.1 dB , which is theoretically much better than the grating coupler in Figure 4.20.

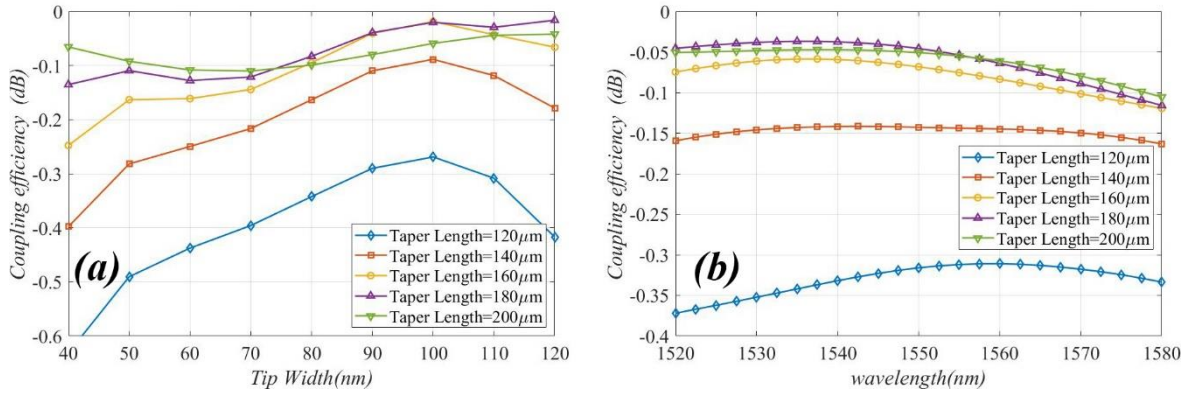


Figure 4.26 (a) The coupling efficiency versus wavelength of different taper lengths. (b) The coupling efficiency versus tip width of different taper lengths.

To summarise, the dimension spec of the SU8 covered taper coupler for fabrication is identified in this section. The parameters determined for fabrication are $W_s = 3 \mu m$, $H_s = 2.5 \mu m$, $W_t = 100 nm$, and taper length no less than $200 \mu m$. A schematic of the mask for lithography is drawn based on these parameters and is shown in the appendix A.2. In the mask layout, the taper length is extended to $300 \mu m$. The patterning error and washing process can lead to lithography error and potentially mistakenly removing the taper tip, respectively.

4.5.3 Design and simulation of edge coupler II: Free space taper coupler

The proposed SU8-covered taper coupler is a solution to the fibre waveguide coupling problem. However, its requirement of high precision of alignment significantly impacts the experiment, which will be introduced in detail in the following chapter. Besides, the SU8 material is hard to form an ideal rectangular waveguide, and the roughness of its top and side wall are unpredictable. Therefore, another edge coupler design is proposed, which is also an inverse taper structure but utilizes the free space coupling principle. The significant difference between this design and SU8 coupler is the absence of the SU8 outer waveguide, which means this design only contains three materials and performs a simple box-core-cladding structure from bottom to top. As seen in Figure 4.27, the SU8 waveguide is removed, and a pre-guiding SOI waveguide with the exact width of the tip of the taper extends to the facet. According to the coupled mode theory (CMT), the light energy propagating in free space will tend to concentrate on a high refractive index area. For this case, Although the dimension of pre guiding SOI waveguide does not support single-mode propagation inside, it still can attract the energy and performs a weak confinement effect on the incidence light, which could supply more tolerance for the alignment. Unlike the SU8 coupler, the fibre is supposed to aim at the

centre axis of the SOI waveguide for this free-space coupler. Besides, the taper plays the same role as shown in Figure 4.25.

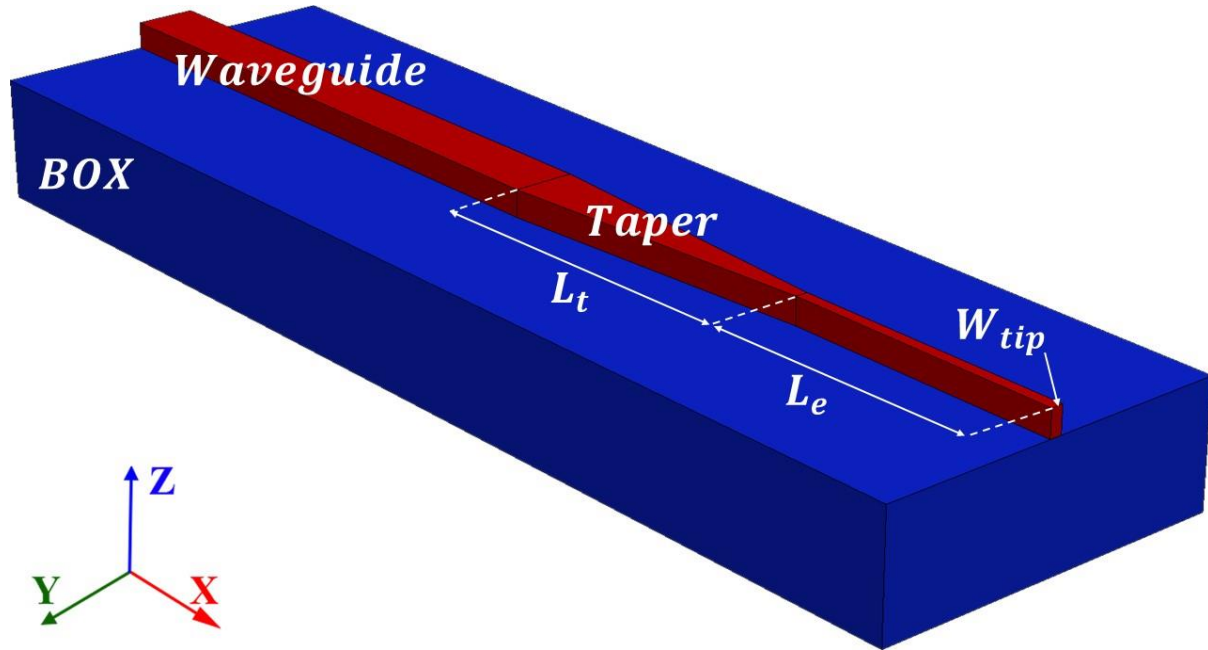


Figure 4.27 The simulation model of the free space coupler.

An FDTD simulation is conducted with $W_{tip} = 100 \text{ nm}$, as that is the optimized value from chapter 4.5.2, the L_e and L_t is set as $25 \mu\text{m}$ and $50 \mu\text{m}$ here, since this taper length is enough for verification of the taper's function. The normalized E field from the top view (XoY plane) and side (XoZ plane) sectional views are shown in Figure 4.28. Unlike the E-field distribution of the SU8 coupler, a significant amount of energy concentrates at the inlet boundary of the model and then dissipates to free space due to the absence of the SU8 outer coupler. The pre-guiding stage indeed plays a role in confinement, as seen in Figure 4.28 (a) at X range from 30 to $40 \mu\text{m}$, a tendency of concentration towards the side wall of pre-guiding stage is witnessed, but this effect is much weaker than the confinement of SU8. Similarly, a side wall concentration of energy is observed at X range from -10 to $10 \mu\text{m}$ of the taper, then a stable single mode propagation is shown a X range from -45 to $-25 \mu\text{m}$, but the magnitude of final guided mode in the SOI waveguide of this free space coupling is significantly weaker than the SU8 covered taper coupler, which indicates the coupling efficiency of this design could less than the design with SU8, the following EME based simulation also suggests this conclusion. As for the E field of the side view, the mode leaking in the box layer is much more severe than the cladding layer since the index of the bottom layer is more significant than the cladding layer.

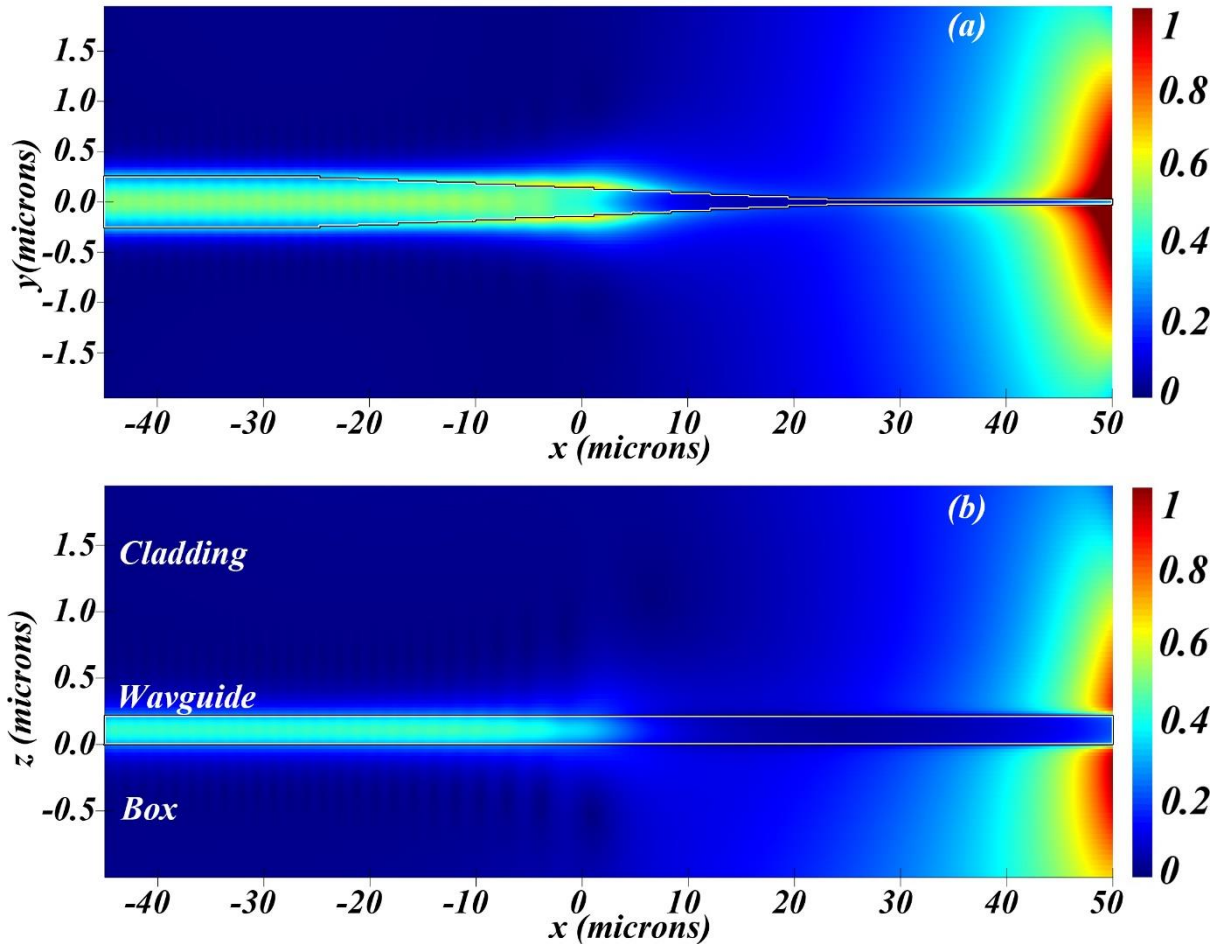


Figure 4.28 The simulated E profile of the direct taper coupler ($W_{tip} = 100 \text{ nm}$, $L_e = 25 \text{ }\mu\text{m}$, $L_t = 50 \text{ }\mu\text{m}$). (a) Top view (XoY plane). (b) Side view (XoZ plane)

Then an EME simulation is performed to numerically estimate the coupling efficiency versus taper length for this design. As the results are shown in Figure 4.29, in general, coupling efficiency rises with increasing taper length, similar to the SU8-covered taper coupler, but a longer taper length ($1630 \text{ }\mu\text{m}$) is required to this free space coupling design for achieving theoretical 0 loss maximum coupling, this length is impractical for achieving the object of this project. The major worry is about the impact on the FWM conversion band for such a long taper with $1630 \text{ }\mu\text{m}$ at both end of the SOI waveguide. Besides, From the fabrication perspective, fabricating and maintaining a decent gradient on the side walls for a taper with such an exaggerated length-width ratio is difficult and unfeasible. Therefore, a compromise of adopting a shorter taper length is inevitable. The taper length for the final design is determined as $300 \text{ }\mu\text{m}$, because an acceptable coupling efficiency ($\sim -1.25 \text{ dB}$) is predicted, and this length is also feasible for fabrication. The mask for the fabrication of this free space coupling design is also shown in the appendix A.2. Although the coupling efficiency in the simulation of this design is lower than the SU8 one, the large mode area at the inlet facet caused by the thin pre-

guiding stage can supply more tolerance for the manual alignment between lensed fibre and coupler, which is witnessed in following chapter 5.2.

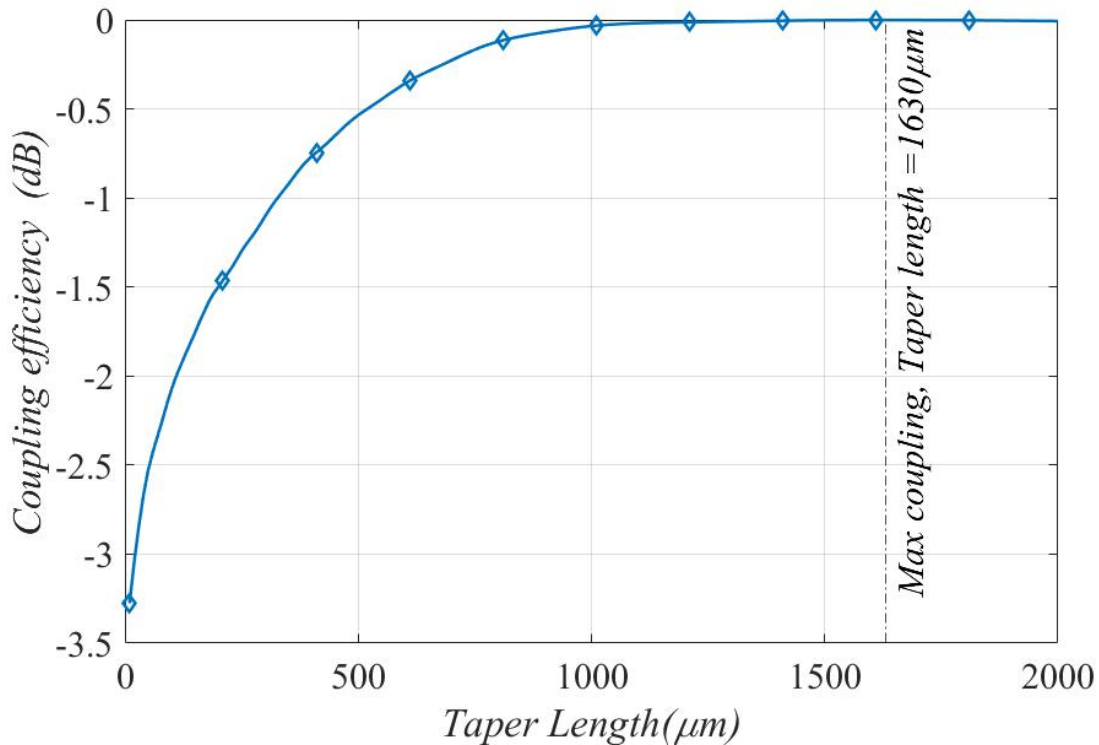


Figure 4.29 Coupling efficiency versus Taper Length of the free space taper coupler with $W_{tip} = 100 \text{ nm}$ and $\lambda = 1546 \text{ nm}$.

4.5.4 Insertion loss from lensed fibre to edge coupler

The proposed two designs of edge coupler numerically analyse the potential insertion loss caused by mode mismatch and mode transformation. However, another significant proportion is not considered, which is the insertion loss between the fibre lenses and to coupler facet. This section discusses this part of insertion loss based on numerical simulation.

The lensed fibre is a series of special optical fibres with a dedicated shaped end for reforming the output beam shape; commonly, it can be categorised as tapered, spherical, and multi-stage lensed fibre. The particular shape is usually formed by thermal stretch, melting and polishing. Diameters of the core of single-mode fibres for the C band are generally 8 to 10 μm , which is much larger than the coupler dimension, not to mention the dimension of the silicon waveguide. With the lensed fibre, the output beam size of the fibre is reduced to match the inlet dimension of an edge coupler. The lensed fibre deployed for the experiment of this project is tapered lensed fibre. For this species, its output beam is a gaussian like profile, as it is shown in Figure 4.30. The narrowest point of the beam is the beam waist w_b . L_f is the working

distance of the lensed fibre, which indicates the distance from the end of the lensed fibre to the beam waist. L_G is the distance from lensed fibre end to the facet of the edge coupler, and θ is the divergence angle of the output beam. The simulation is performed with a 2D FDTD solver with the previously determined coupler dimension. The fibre lensed is set as a Gaussian source, and the distance between the injection plane and the waist of the source is set as the exact value of L_f . As for beam waists, two lensed fibres are deployed in the lab with 3 μm and 5 μm of beam waists, respectively.

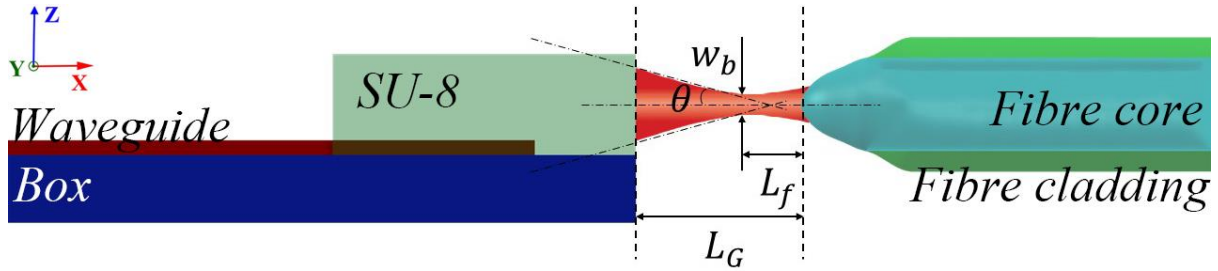


Figure 4.30 Schematic of the simulation model of lensed fibre to coupler facet coupling.

Figure 4.31 illustrates coupling efficiency versus gap distance between fibre and coupler for different beam waists. Assuming perfect alignment, only L_G and w_b are considered variable for this simulation. Both lensed fibres show maximum coupling at zero gap position. However, this gap position is impractical due to contamination and scratch on both surfaces caused by contact. With increasing gap distance, both waists experience a little drop in coupling and then maintain stability for a short range. That range corresponds to the working distance, meaning that the beam waist is nearly located on the facet of the coupler in this position range. Therefore the coupling efficiency maintains stability. Then with the gap continuing to rise, the coupling efficiency drops dramatically and inevitably. Besides, the coupling efficiency of 3 μm waist is larger than the waist of 5 μm in all the range.

Intuitively, the 3 μm waist is the best solution. However, another factor challenges this conclusion, the beam waist influences the divergence angle. According to the product spec, the lensed fibre with 3 μm waists is with $\sim 50^\circ$ divergence angle, and the 5 μm one is $\sim 40^\circ$, which caused inconsistent experimental results, as shown in chapter 5.2. The following equation gives the numerical aperture of the SU8 coupler.

$$NA = \sqrt{n_{SU-8}^2 - n_{PECVD SiO_2}^2} = 0.634 = \sin\theta \cdot n_{Air}, \quad \theta = 39.362^\circ \quad (4.27)$$

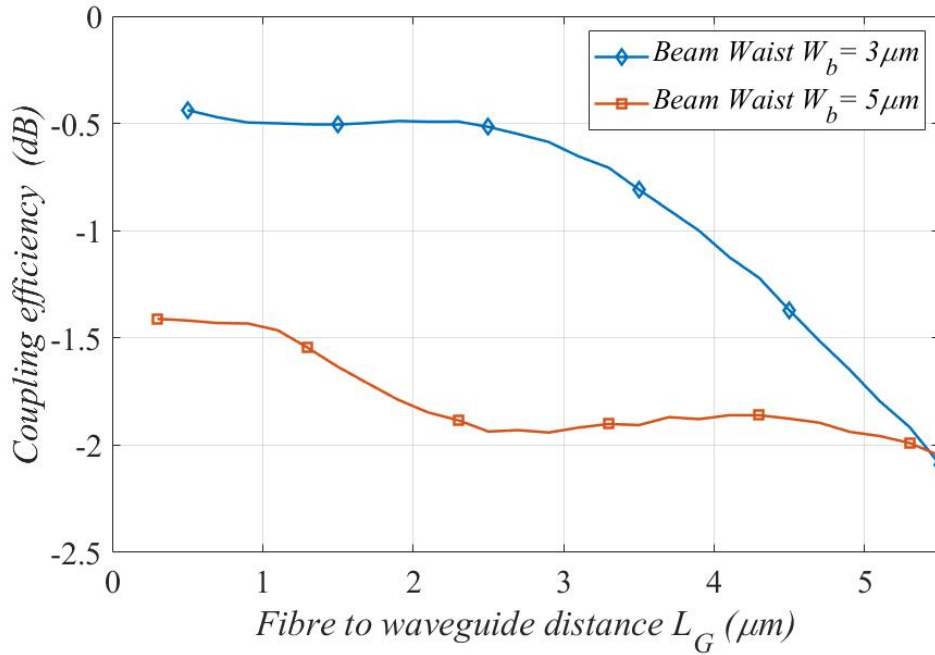


Figure 4.31 Coupling efficiency versus fibre to waveguide distance L_G for different beam waists respectively.

Where refractive indices are adopted as a single value at 1546 nm, the NA of the SU8 coupler is 0.634, and the acceptance angle θ of SU8 is then derived out as 39.362° according to Snell's law. These values suggest that although the beam waist of 3 μm is more overlapping than the 5 μm , its large divergence angle caused more loss for the inlet side of the SU8 coupler. Therefore, the final coupling layout adopts 5 μm waists lensed fibre at the inlet and 3 μm at the outlet, because a smaller divergence angle benefits the input coupling and a larger divergence angle ensures more receiving at the output side.

To summarise, this chapter proposes two edge coupler designs for fabrication. Namely, the SU8 covered taper coupler and the free space taper coupler, respectively. These couplers will be fabricated at both sides of the SOI waveguide, and lensed fibre with 5 μm and 3 μm of beam waist is adopted for the inlet and outlet of the chip, respectively.

4.6 Conclusion

This chapter describes systematic works towards the FWM in silicon waveguides in theory and numerical simulation. An optimized design of SOI waveguide on 220nm thickness wafer for single mode FWM is proposed. Two optimized designs of edge couplers are reported for addressing the fibre-to-waveguide coupling issue.

Chapter 5

Experiment

This chapter introduces the experiment system's layout and the experiments' inventory list, three main parts are covers in this chapter. Initially, the basal set up of whole experiment system is introduced, the equipment adopted in the experiment is listed. The rest two parts introduced the two parts of experiment including test of the coupling efficiency of the SOI waveguide sample and test of the conversion efficiency of FWM on SOI waveguide.

5.1 Experimental set up

5.1.1 SOI chip samples

Based on the design discussed in the last chapter, two batches of SOI waveguide chips with two types of edge couplers were fabricated at Glasgow University. The first batch includes four independent chips with the SU8 edge coupler. Each chip contains 35 independent SOI waveguides organized into seven groups. The waveguide length for this batch is 15 mm. For the second batch, the waveguide length is modified to 20 mm, and the coupler is replaced with the free space taper coupler. Only two chips are received in the 2nd batch, and each chip contains 20 independent waveguides.



Figure 5.1 Photos of the first batch of SOI chips (with SU-8 covered taper coupler), from left to right is the chips No. 1,2,3, and 4, respectively

Figure 5.1 exhibits photos of the first batch of SOI chips with SU-8 covered taper coupler, the size of those chips has slight differences due to a different position on the single wafer and

cleaving process. They are generally no more significant than the thumb fingernail size. As seen in the photo of waveguide No.2, the black object is a scissor handle, which could be a reference for a better understanding the chip size. More detail under microscope photos of the chip is shown in chapter 5.2 to discuss the coupling efficiency test.



Figure 5.2 Photos of the second batch of SOI chips (with free space taper coupler), from left to right is the chip no 1 and 2, respectively

Figure 5.2 shows photos of the 2nd batch of SOI chips, which are generally similar in size to the first batch. More detail is shown in Appendix A.3.

5.1.2 Manually alignment system

As mentioned before, alignment accuracy is crucial for the fibre-to-waveguide coupling, and a manual high-precision alignment system is employed. Figure 5.3 is a photo of the fibre-to-waveguide alignment system adopted. Component No.1 at the bottom is an X and Y axes stage supplied by Thorlabs; two of them are at the opposite position but overlapped by illustration. These stages are mounted on the optical table, representing the basement of the whole alignment system and in charge of wide-range rough position adjustment. Component No.2 mounted on No.1 is a pair of X, Y, and Z axes piezo controllers supplied by the Elliot E-Wedge series. They support manual and piezo-controlled adjustments and supply 10 nm resolution for 25 μm piezo controlling range. These stages are used for the fine position adjustment in all three axes. On top of component No. 2, component No. 3 is mounted, a pair of two axes rotation stages supplied by Elliot as well; they are adopted for the yaw and tilt control of lens fibre, which can supply less than one arc seconds resolution towards the degree. A pair of V-groove lensed fibre holders (No.4) are mounted on those rotation stages; these components are where the lensed fibres (No.5) are fixed on, the right side one is for input, and the left side one is for output. Between the two lensed fibres is the SOI chip (No.6), placed on

a stage supplied by Thorlabs (No.7). An optical microscope is deployed over the SOI chips to monitor the alignment process.

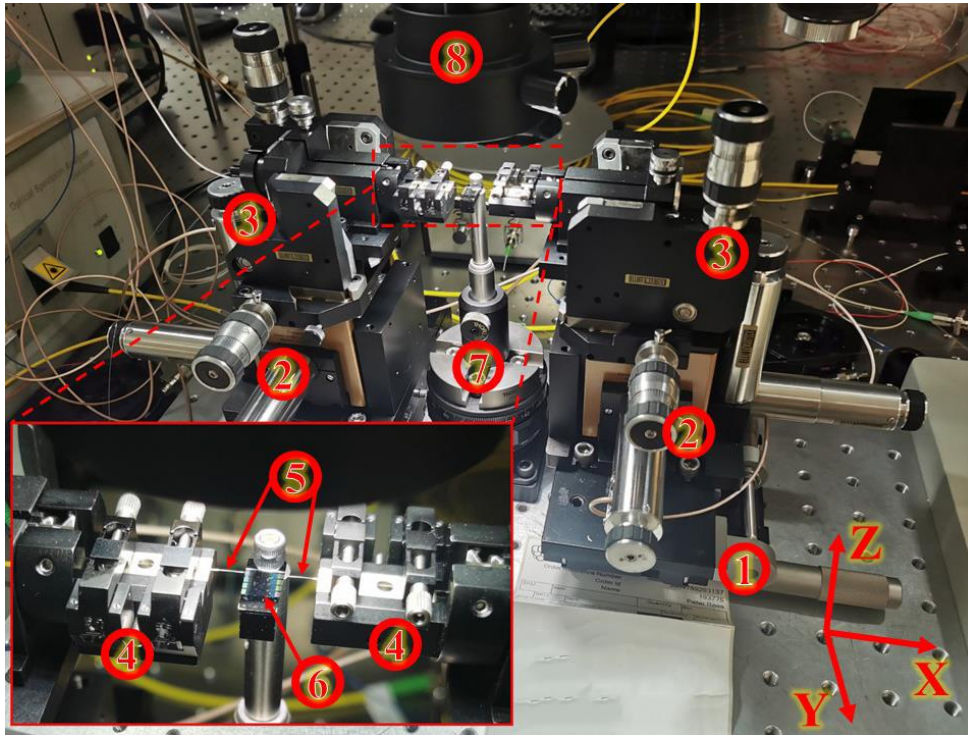


Figure 5.3 The fibre-to-waveguide alignment system

5.1.3 FWM testing system layout

The testing system to evaluate the FWM properties of SOI waveguide was built at the University of South Wales. Despite SOI chips, non-linear Semiconductor Optical Amplifiers (SOA) and High Nonlinear Fibres (HNLf) are tested as well as a comparison for the SOI chips.

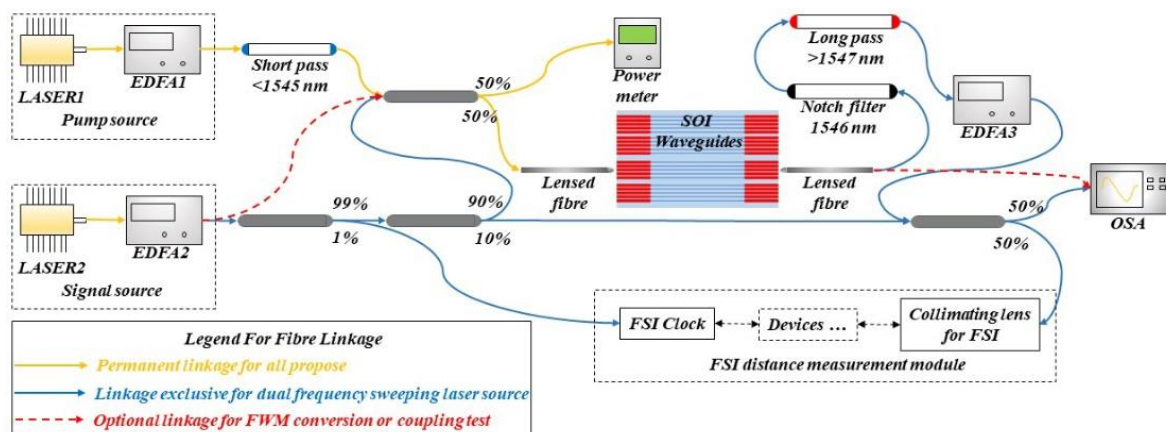


Figure 5.4 Block diagram of the experimental testing system of SOI waveguide.

Figure 5.4 is the block diagram of the SOI waveguide testing system. FWM properties tests, coupling efficiency tests, and dual frequency sweeping tests are all implemented by this

system. The pump source of the system is formed by a Thorlabs DFB laser with a 1544 nm to 1546 nm tuning range amplified by a 23 dBm output erbium-doped fibre amplifier (EDFA). The light output from the pump source will then pass a short pass filter (<1545 nm) to eliminate the noise from the EDFA gain spectrum, mainly located at the wavelength range over 1550 nm. A New Focus TLM-8700 tuneable laser is employed as the signal source, and its output is also amplified by another 23 dBm EDFA and then passes through a 99/1 splitter, where 1% of the energy of the light is directed to a clock module for the FSI, it is a Mach Zehnder interferometer to generate the clock signal for FSI sampling synchronization. The 99% output port is linked to a 90/10 splitter, and then 90% of the signal light is guided to a -3 dB coupler for mixing with the pump signal and then directed to the SOI waveguide for generating FWM. Another 10% of signal energy from the 90/10 splitter is guided to another -3dB coupler for recombination with the idler signal from FWM and then forms the dual-frequency sweeping laser output, another output from the -3dB coupler is linked to the Optical Spectrum Analyser (OSA) for measurement and record the spectrum and test result.

A notch filter and a long pass filter are placed after the SOI to eliminate the pump and signal light from the FWM output; after these two filters, only the idler light remains, which is then amplified by another 23 dBm EDFA to be combined with the rest 10% of the original signal light, finally to be guided to the collimating lens of FSI system for illuminating the target. The schematic of the FSI module is not shown comprehensively since this thesis only focuses on the dual frequency sweeping laser source and FWM generation.

When testing the coupling efficiency, the signal source part is switched off. Only the pump source is required. Besides, the notch filter, long pass filter, and EDFA3 are disconnected during the coupling test, and the output from the lensed fibre is directly linked to the input port of OSA, as the red dotted linkage shown in Figure 5.4.

During the FWM conversion test, both the pump and signal source are used. The signal source is directly linked to the -3dB coupler, and the output of SOI is directly linked to the input port of OSA, as the red dotted linkage shown in Figure 5.4.

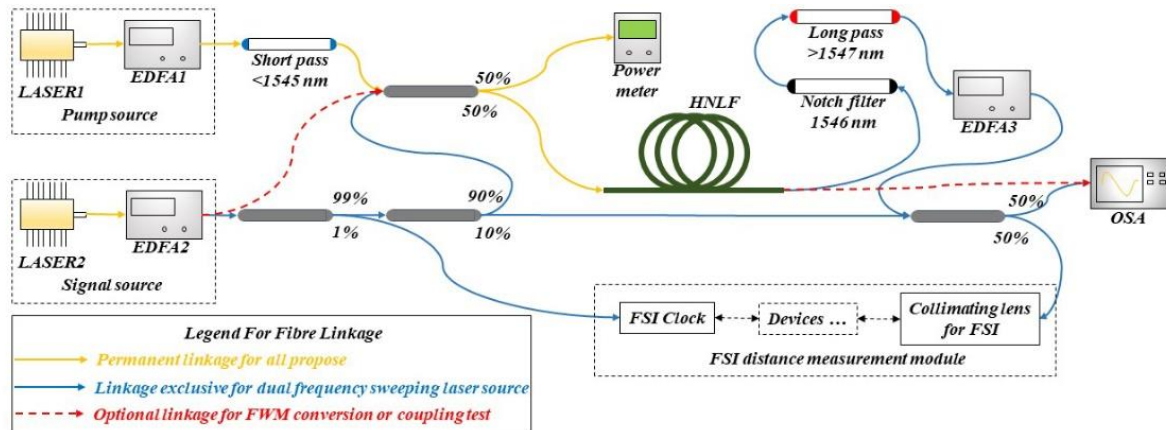


Figure 5.5 Block diagram of an experimental testing system for HNLF.

Figure 5.5 illustrates the block diagram for testing the HNLF, which is generally the same as the system for SOI. HNLF replaces only the SOI and lensed fibre module. Two types of HNLFs are prepared for testing. In particular, no coupling test is conducted for the HNLF since it does not have the coupling problem since it is directly linked with SMF with FC/APC or FC/PC connection.

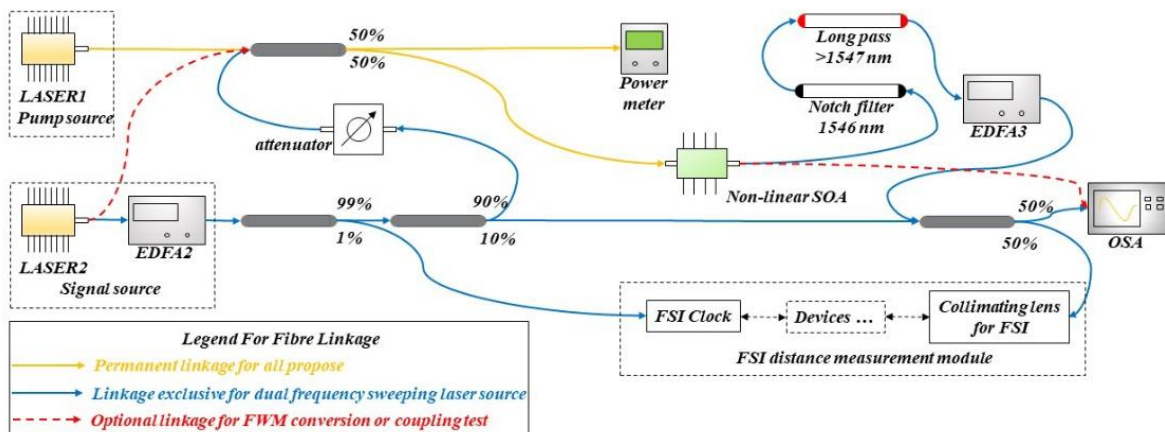





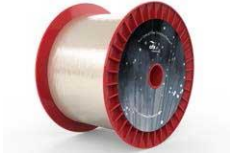
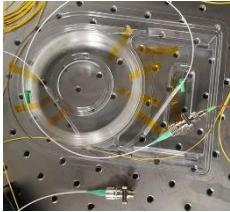





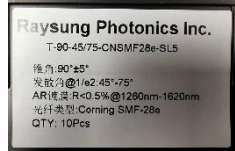
Figure 5.6 Block diagram of the experimental testing system for Non-linear SOA.

The system for non-linear SOA is slightly different, as seen in Figure 5.6. The SOA adopted for the test is Kamelian L1. Since non-linear SOA is an active filter component with a self-amplification effect, the EDFA 1 for the pump source is no longer required. The EDFA 2 for signal source is kept for ensuring sufficient energy for the FSI system and dual frequency sweeping laser source, but an optical attenuator is adopted between the 90/10 splitter and -3dB coupler in case high energy damage the non-linear SOA. The SOA does not have the coupling issue as well.

Table 5.1 lists the instruments adopted for the whole experiment section.

Table 5.1 Inventory list of adopted equipment

<i>Item title</i>	<i>Supplier and model</i>	<i>Key Parameter</i>	<i>Photo</i>
LASER 1	Newfocus TLM-8700	1510-1620 nm tuning range with 2-2000nm/s tuning speed, wavelength accuracy: ± 30 pm	
LASER 2	Thorlabs Pro 8000-4	1546 nm module is adopted, tuning range for 2 nm	
EDFA 1	Optilab EDFA-I-23-B	Up to 23 dBm output power	
EDFA 2	Amonic AEEDFA-PM-37-RF-A	Up to 23 dBm polarized maintain out put	
EDFA 3	Thorlabs 300s	Maximum output optical power 26 dBm	
HNLF 1	OFS HNLF-Z1-0100-1-2-Z0	100 meters length, Non-linear coefficient: $10.8W^{-1} \cdot km^{-1}$	
HNLF 2	NL 1016 B	100 meters length, Non-linear coefficient not specified	
Non-linear SOA	Kamelian SOA-NL-L1-C-FA	Biased at 300 mA, Peak gain wavelength of 1550 nm with gain of 26 dB and -3 dB bandwidth	

		of 64 nm, gain recovery time of 25 ps	
<i>OSA</i>	Anritsu MS9740B	For 600 nm to 1750 nm spectrum range, supporting multi and single mode input	
<i>Input lensed fibre</i>	OZ optics TPMJ-X-1550-8/125-0.4-7-5-26-2	Beam waist $5 \pm 0.5 \mu\text{m}$	
<i>Output lensed fibre</i>	Raysung Photonics Inc.	Beam waist $3 \mu\text{m}$ Divergence angle: 45 to 75 degree	

5.2 Experiment 1: Coupling efficiency test

The first experiment tests the coupling efficiency of each waveguide on every chip, which is necessary before FWM testing. Within this step, waveguides with the best coupling efficiency are identified so that the following experiment can be conducted. The system adopted for the coupling test is introduced in the previous section. All the coupling test is conducted with a single wavelength signal from the pump source with a wavelength from 1545.2 to 1546.9 nm. The input energy P_{in} is the read number for the power meter linked to another output port of the -3 dB coupler. As shown in the previous section, power output from this port equals the port linked with the input lensed fibre. The output power P_{out} is measured by another optical power meter deployed at the same connector as the OSA. For each waveguide, three independent data reading was recorded, and the maximum reading number is shown in this thesis. Then the single-side insertion loss is defined as,

$$\delta = \frac{P_{in} - P_{out}}{2} \quad (4.28)$$

As mentioned in section 4.5.4, the insertion loss at the input and output sides may differ. However, the power reading inside the SOI waveguide is impractical. This δ value is taken for the single side insertion loss as an average loss of both sides.

5.2.1 Coupling test of SU8-1

Figure 5.7 illustrates the microscope view photo of SOI waveguide chip No.1 with SU-8 covered taper coupler. As it can be, two photos are taken for the left and right parts, respectively, due to the limitation of the angle of view of the microscope used. From top to bottom, seven groups of the waveguide are in view, marked as groups No.1 to No.7, respectively. Each independent group contains five waveguides named waveguides 1 to 5, respectively. A clear white area is seen at both sides of the SOI waveguide (red dotted rectangular area); these are the SU-8 outer waveguides of the couplers. In particular, the SU8 coupler on the right-hand side is not the same length as the left side, which is made on purpose. The chip is cleaved down from the wafer with a cleave angle of about 8 to 10 degrees at the right side, which could supply various SU-8 waveguide lengths. Hence there should be a waveguide with the best SU-8 length for maximum coupling efficiency.

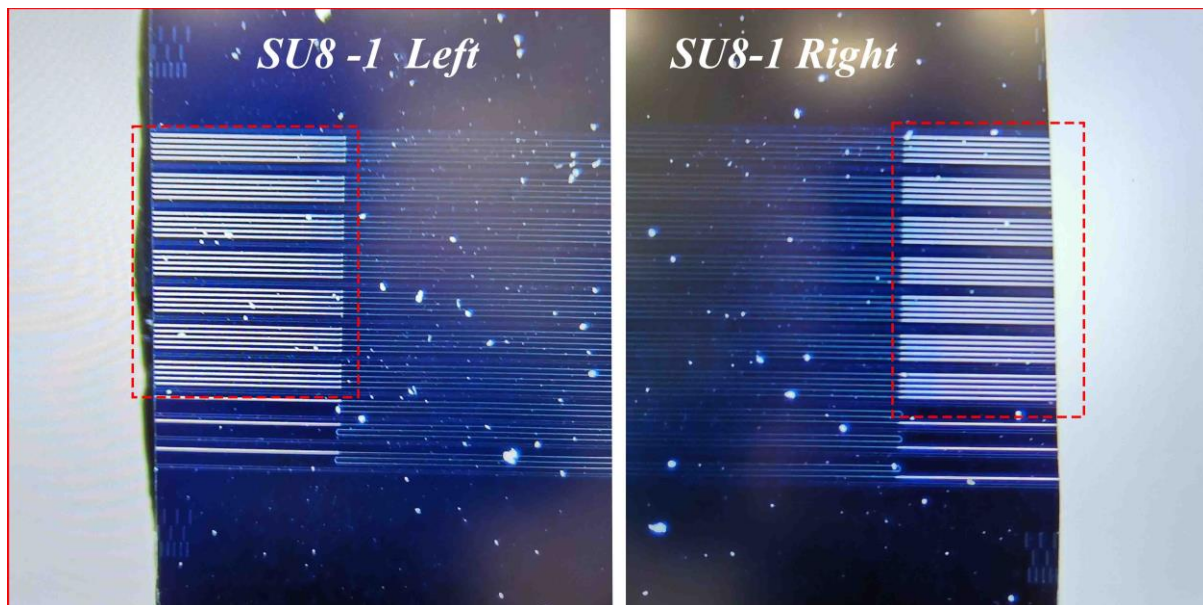


Figure 5.7 Microscope view of SOI waveguide with SU-8 covered taper coupler No.1.

Table 5.2 exhibits the coupling test results of waveguide SU8-1, the value NaN means no coupling-out signal is detected; the peak is immersed in the background noise, which indicates the waveguide is not working, maybe damaged. The insertion loss measured by this waveguide is generally high. Two minimum loss waveguides are No.1 and 2 in group 6, with an insertion loss of 4.58 dB and 4.515 dB, respectively. Waveguides No. 1, 2, and 3 are not work may be

due to the quality of the cleaving process. As seen on the left side, the facet of cleaving shows an irregular shape, indicating poor facet quality for couplers.

Table 5.2 Coupling test results of waveguide SU8-1.

<i>Group Number</i>	<i>Waveguide number</i>	<i>Input energy P_{in} (dBm)</i>	<i>Output energy P_{out} (dBm)</i>	<i>Insertion loss of single side δ(dB)</i>
1	1	18.23	NaN	NaN
	2	18.23	NaN	NaN
	3	18.23	NaN	NaN
	4	18.23	8.37	4.93
	5	18.23	4.66	6.785
2	1	18.23	NaN	NaN
	2	18.23	5.52	6.355
	3	18.23	7.08	5.575
	4	18.23	-13.93	16.08
	5	18.23	7.93	5.15
3	1	18.23	-32.53	25.38
	2	18.23	-55.64	36.935
	3	18.23	7.39	5.42
	4	18.23	6.32	5.955
	5	18.23	1.58	8.325
4	1	18.23	1.31	8.46
	2	18.23	1.43	8.4
	3	18.23	7.49	5.37
	4	18.23	8.03	5.1
	5	18.23	4.91	6.66
5	1	18.23	7.25	5.49
	2	18.23	7.14	5.545
	3	18.23	8.4	4.915
	4	18.23	8.06	5.085
	5	18.23	8.83	4.7
6	1	18.23	9.07	4.58
	2	18.23	9.2	4.515
	3	18.23	8.71	4.76
	4	18.23	-12.67	15.45
	5	18.23	9.04	4.595
	1	18.23	1.31	8.46
	2	18.23	1.33	8.45

7	3	18.23	2.88	7.675
	4	18.23	4.72	6.755
	5	18.23	5.73	6.25

5.2.2 Coupling test of SU8-2

The microscope photo of chip SU8-2 is shown in Figure 5.8. It is generally the same as chip SU8-1. However, only one group of waveguides is working on this chip, which is the group at the bottom. The other group are damaged to varying degrees for different reasons. As can be seen in red dotted rectangular No.1, the left couplers of waveguides in group 1 are irregular, and their SU-8 coupler contains an exact knot shape which is presumed to be formed due to the thermal process. Waveguides in group 2 meet similar problems as group 1. Although their deformation (in red dotted rectangular 2) is not apparent as in group 1, it still leads to unfunctional waveguides. Remarkably, a big scratch is seen on the chip SU8-2, as shown in red dotted rectangular 3, and it covers the range from waveguide group 3 to group 7. The reason group 7 survives is that the scratch on group 7 is relatively thin, which only hurts the cladding layer at this position. However, the other waveguides are all damaged. The wide scratch on them may damage both the cladding and core.

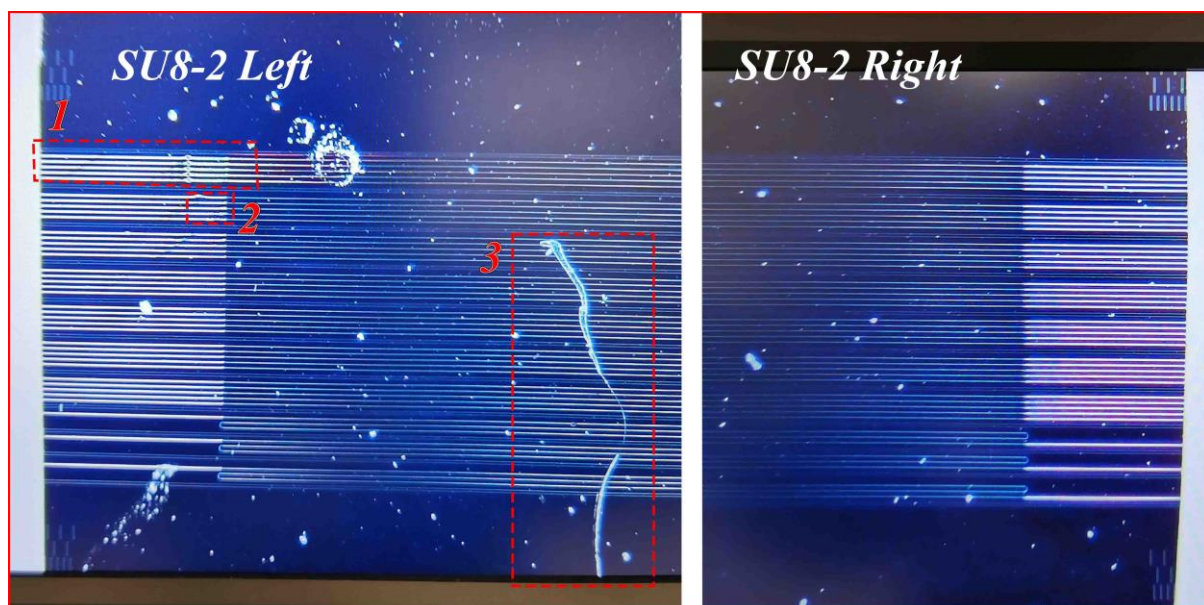


Figure 5.8 Microscope view of SOI waveguide with SU-8 covered taper coupler No.2.

Therefore, Table 5.3 only shows the results of group 7. Overall, the insertion loss of this group is higher than chip SU8-1. The minimum loss is seen on waveguide 4, which shows a 7.54 dB insertion loss.

Table 5.3 Coupling test results of waveguide SU8-2.

Group Number	Waveguide number	Input energy P_{in} (dBm)	Output energy P_{out} (dBm)	Insertion loss of single side δ (dB)
7	1	18.9	-0.22	9.56
	2	18.9	0.67	9.115
	3	18.9	-0.33	9.615
	4	18.9	3.82	7.54
	5	18.9	4.79	7.055

5.2.3 Coupling test of SU8-3

Chip SU8-3 is regular without any apparent damaged parts. One thing needs to be mentioned, the right-hand side coupler of waveguide No.3 in group 5 was deformed due to high-power laser input (~ 20 dBm) for over 1 hour, which happened during a dual sweeping test. As shown in Figure 4.39, the insertion figure is zoomed in view of that damage, clear bubbles are observed on that waveguide, which may be caused by scattering and absorption of laser energy by defects in that coupler. This phenomenon hints at the damage risk of polymer waveguides in use in a high-power system, which prompts the design and fabrication of waveguides with free space inverse taper coupler

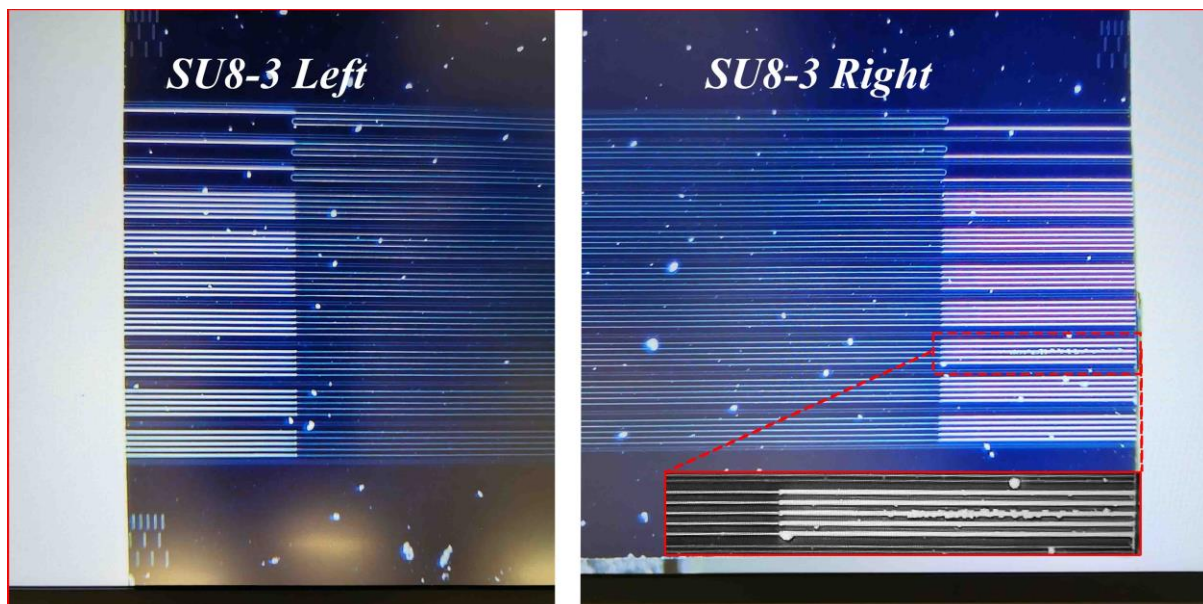


Figure 5.9 Microscope view of SOI waveguide with SU-8 covered taper coupler No.3.

Table 5.4 lists the tested insertion loss of waveguides on chip SU8-3. Two waveguides are not working, namely waveguide 1 of group 2 and waveguide 5 of group 6. The minimum

insertion loss obtained on this chip is 5.02 dB from waveguide No.5 of group 3. Besides, waveguide No.3 of group 1, waveguide No.3 of group 2, waveguide No.4 of group 4, and waveguide No.2 of group 5 all show insertion loss below 6 dB with 5.615 dB, 5.465 dB, 5.625 dB, and 5.205 dB respectively.

Table 5.4 Coupling test results of waveguide SU8-3.

<i>Group Number</i>	<i>Waveguide number</i>	<i>Input energy P_{in} (dBm)</i>	<i>Output energy P_{out} (dBm)</i>	<i>Insertion loss of single side δ(dB)</i>
1	1	18.56	4.48	7.04
	2	18.56	-25	21.78
	3	18.56	7.33	5.615
	4	18.56	-0.91	9.735
	5	18.56	5.11	6.725
2	1	18.56	NaN	NaN
	2	18.56	5.18	6.69
	3	18.56	7.63	5.465
	4	18.56	-1.8	10.18
	5	18.56	-2.56	10.56
3	1	18.56	-1.42	9.99
	2	18.56	-1.7	10.13
	3	18.56	6.16	6.2
	4	18.56	5	6.78
	5	18.56	8.52	5.02
4	1	18.56	4.92	6.82
	2	18.56	4.97	6.795
	3	18.56	5.5	6.53
	4	18.56	7.31	5.625
	5	18.56	-9	13.78
5	1	18.56	1.05	8.755
	2	18.56	8.15	5.205
	3	18.56	6.66	5.95
	4	18.56	2.8	7.88
	5	18.56	-3.82	11.19
6	1	18.56	-0.86	9.71
	2	18.56	3.09	7.735
	3	18.56	-1.18	9.87
	4	18.56	-0.21	9.385

	5	18.56	NaN	NaN
7	1	18.56	-0.52	9.54
	2	18.56	0.26	9.15
	3	18.56	-30.18	24.37
	4	18.56	-8.27	13.415
	5	18.56	-15.63	17.095

5.2.4 Coupling test of SU8-4

Chip SU8-4 has no apparent damage or defects, as shown in Figure 5.10. All waveguides on this chip are working correctly, and minimum insertion loss over all 4 SU8 chips is obtained on this chip. Therefore, this chip is adopted as the premier choice for the test of FWM and dual frequency sweeping laser.

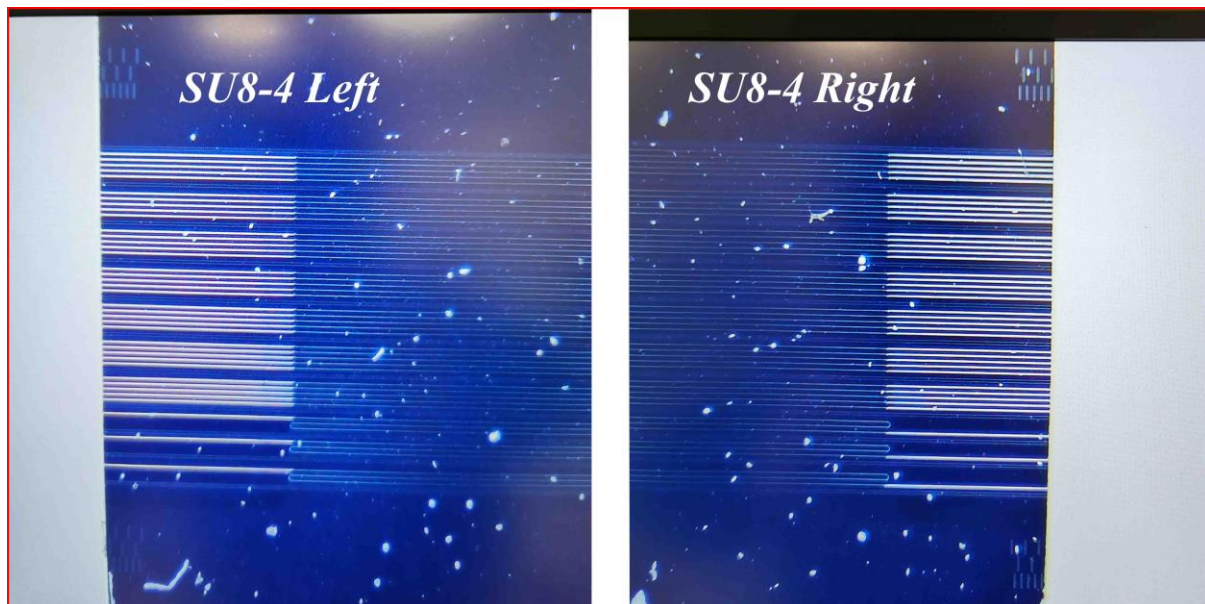


Figure 5.10 Microscope view of SOI waveguide with SU-8 covered taper coupler No.4.

As shown in Table 5.5, the minimum insertion achieved is 3.595 dB for waveguide No.1 in group 2. Besides, waveguide No.3 of group 1, waveguide No.1 of group 4, waveguide No.3 of group 4, and waveguide No.5 of group 3 all show insertion loss below 5 dB with 4.11 dB, 4.78 dB, 4.92 dB, and 4.005 dB respectively.

Table 5.5 Coupling test results of waveguide SU8-4.

Group Number	Waveguide number	Input energy P_{in} (dBm)	Output energy P_{out} (dBm)	Insertion loss of single side δ (dB)
	1	18.51	2.5	8.005

1	2	18.51	8.36	5.075
	3	18.51	10.29	4.11
	4	18.51	0.08	9.215
	5	18.51	8.26	5.125
	2	1	18.51	11.32
2		18.51	0.03	9.24
3		18.51	9.85	4.33
4		18.51	4.64	6.935
5		18.51	0.55	8.98
3	1	18.51	2.01	8.25
	2	18.51	-1.27	9.89
	3	18.51	0.52	8.995
	4	18.51	2.25	8.13
	5	18.51	3.46	7.525
4	1	18.51	8.95	4.78
	2	18.51	3.42	7.545
	3	18.51	7.05	5.73
	4	18.51	8.67	4.92
	5	18.51	10.5	4.005
5	1	18.51	6	6.255
	2	18.51	7.49	5.51
	3	18.51	2.36	8.075
	4	18.51	5.6	6.455
	5	18.51	5.08	6.715
6	1	18.51	7.08	5.715
	2	18.51	-1.64	10.075
	3	18.51	9.03	4.74
	4	18.51	8.44	5.035
	5	18.51	4.22	7.145
7	1	18.51	3.33	7.59
	2	18.51	7.45	5.53
	3	18.51	1	8.755
	4	18.51	8.18	5.165
	5	18.51	1.08	8.715

In summary, the measured coupling efficiency is not good as the simulation result. That is mainly caused by the quality of the facet at double sides; both sides are unpolished and uncoated, which leads to more losses on the facet than expected. The unstable SU-8 process is another issue to that problem. Besides, the error during the fabrication of the SOI may also

contribute to this mismatch between the simulation and experimental results. The plasma-enhanced chemical vapour deposition (PECVD) fabricated silicon dioxide covering the top of the waveguide may have a different refractive index than the index we adopted for the simulation.

The coupling efficiency of 2nd batch chips (with free space coupler) is generally lower than the SU-8 coupler, which agrees with the simulation result. However, it is easier for manual alignment. The microscope view of the 2nd batch chip is shown in Appendix A.3.

5.3 Experiment 2: FWM conversion efficiency test

Conversion bandwidth and efficiency are the two most concerned parameters of the designed SOI chip in this work. They are measured and tested by the system mentioned before. Where the pump source adopted is working at a wavelength around 1546 nm, the pump source is sweeping from 1547 nm to around 1570 nm. The notch filter, long pass filter and 10% of the original signal are not required for the FWM conversion test. The output from the FWM module is directly linked to the OSA for analysis. The conversion profiles are obtained from the OSA, the conversion efficiency equals the ratio of the magnitude of the idler peak to the magnitude of the signal peak, and the signal noise (SNR) ratio of the idler peak is recorded and analysed to evaluate the broadband conversion. In comparison, the FWM of nonlinear SOA and two types of HNLFs are tested.

The wavelength detuning is introduced when describing the wavelength parameters of the conversion band and efficiency. The wavelength detuning is defined as the difference of wavelength between pump and signal light, and it is given by $\Delta\lambda = |\lambda_p - \lambda_s|$.

5.3.1 Wideband FWM test of SOI chip

Figure 5.11 (a) and (b) are the FWM spectrum of SOI waveguide at the smallest (1.38 nm) and largest (27 nm) sampling wavelength detuning points, respectively. The waveguide adopted here is waveguide No.1 in group 2 from SU8 chip 4. Four peaks are seen in the spectrum of the most minor sampled $\Delta\lambda$ point, they are the converted pump, signal, pump, and idler peak, respectively, from left to right. Only the two peaks in the middle (pump and signal) are incident light; the FWM process in the SOI waveguide generates the others. The pump and signal for the smallest detuning are 1543.9 nm and 1545.22 nm respectively. Figure 5.11 (b) illustrates the FWM spectrum of the most significant sampled detuning point.

Only three laser signals are observed in the view: signal, pump, and idler, respectively. From left to right, the converted pump is out of the range for that single sample, which does not influence the result analysis. The pump and signal are located at 1546 nm and 1519.96 nm respectively. It is noticeable the pump wavelength is different between the two samples because the pump wavelength is merely adjusted for each sampling signal wavelength to achieve the highest magnitude of the idler peak. In addition, a clear baseline is seen in figure (b), which is the overall gain spectrum of EDFA. A hill is seen between the signal and pump peak. Since the FWM is an energy-sensitive process, both pump light and signal light are pre-amplified by two EDFAs, making the results suffer from the EDFA gain spectrum. Frankly, the gain spectrum is supposed to be symmetric with respect to the pump wavelength, which means another hill should appear on the idler side. However, for a better idler quality, a shot pass filter is applied between the pump source and the -3 dB coupler, as shown in Figure 5.4, to suppress that hill and impact from EDFA baseline to idler SNR. Particularly, the SNR of the idler is introduced to describe the conversion of FWM because the peaks' magnitude-based conversion calculation is significantly influenced by the baseline of EDFA. On the contrary, the EDFA merely impacts the SNR.

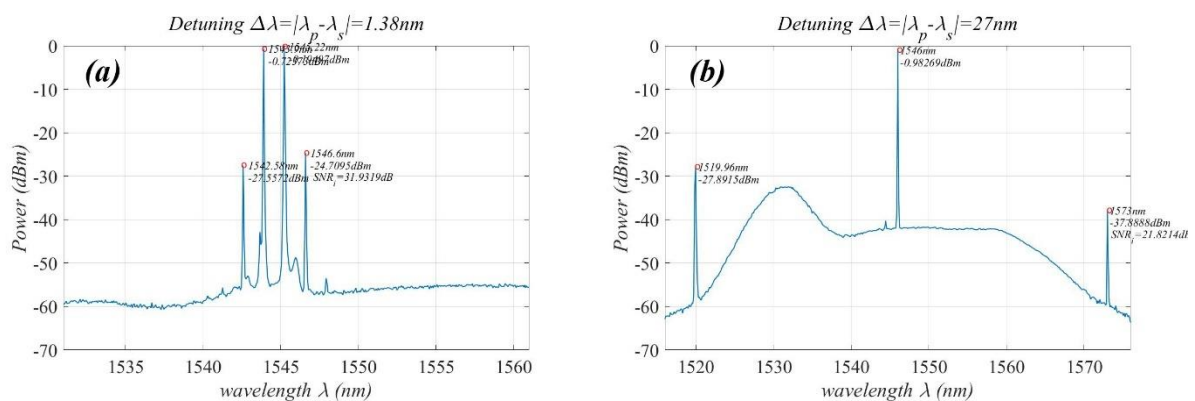


Figure 5.11 Measured FWM spectrum of SOI chip by OSA. (a) FWM spectrum of the smallest detuning. (b) FWM spectrum of the largest detuning.

Figure 5.12 illustrates the sampling and fitting results of the SNR of the idler SNR_i and conversion efficiency versus detuning wavelength, respectively. The SNR is defined as the ratio of its peak value to its adjacent baseline level. As shown, the tested conversion efficiency of SOI drops from -15 dB to -25 dB with the wavelength detuning increase from 5 to 20 nm, but SNR_i maintains stable at 30 dB in the same region because the conversion here is evaluated by the magnitude of peaks read from the optical spectrum analyser (OSA). When the detuning wavelength continuously increases, the scanning band of OSA is required to be

expanded to cover the range from signal to idler wavelength. Since the expanding spectrum measuring range will influence the sampling rate and wavelength step of the OSA, magnitudes read from OSA of large wavelength detuning will be relatively smaller than its actual value, which could lead to a misreading of conversion efficiency. Honestly, accurately measuring the conversion efficiency of FWM is quite tricky. The most accurate method, in theory, is using a different combination of filters and power meters to precisely measure the magnitude of peaks in different wavelength bands by filtering all the other wavelengths, but all these different devices for different wavelengths will introduce various noise figures to the system and further increase the uncertainty of the whole testing system. Therefore, to minimize the uncertainty, the result reading of the FWM testing in this project still adopts a single OSA.

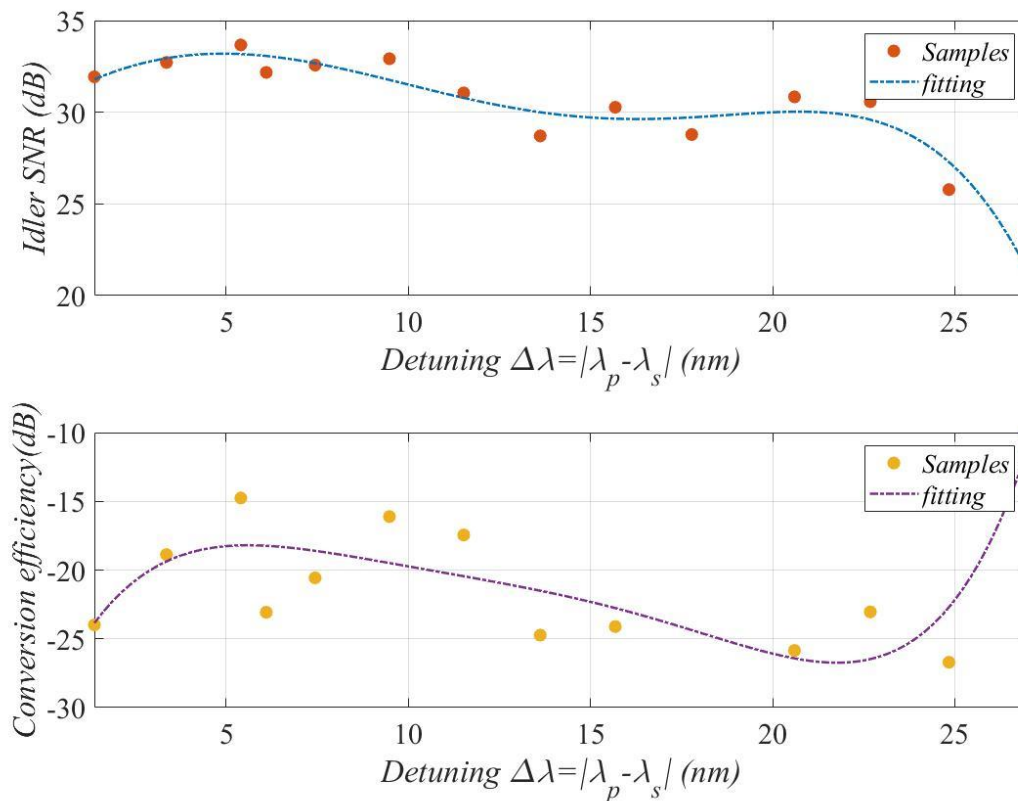


Figure 5.12 Measured wide band FWM results of SOI chip. (a) The SNR of idler SNR_i versus wavelength detuning $\Delta\lambda$, including sampled data points and fitting curve. (b) The conversion efficiency versus wavelength detuning $\Delta\lambda$, including sampled data points and fitting curve.

It is noticeable that the conversion efficiency of the most significant wavelength detuning point is abnormally higher than all the other sampling points, but the SNR is lower than all the other points. The reason behind this phenomenon is the influence of the EDFA's gain spectrum. As shown in Figure 5.11(b), both the signal and idler exceed the gain band of the EDFA, which

suggests that the result at the largest wavelength detuning point is not comparable with the others. Thus, the wide-band testing is cut off at this detuning value.

In conclusion, the SOI waveguide shows good wide band conversion in both conversion efficiency (around -20 dB) and SNR (around 30 dB) for $\Delta\lambda$ range from 0 to 25 nm, with pump wavelengths around 1546 nm, it can be seen as a conversion band from 1521 to 1571 nm, which covers the whole C band.

5.3.2 Wide band FWM test of HNLF

100 meters long OFS HNLF-Z1-0100-1-2-Z0 is first adopted as an FWM generator for this FWM test. The FWM spectrum of the smallest and largest sampling detuning point is shown in Figure 5.13. Unlike the SOI waveguide, two extra side peaks are observed surrounding the four FWM peaks, as shown in Figure 5.13 (a). These peaks are the 2nd-order conversion of FWM, which suggests high FWM conversion efficiency at this $\Delta\lambda$. It is also can be seen influence of EDFA baseline to idler peaks in Figure 5.13 (b).

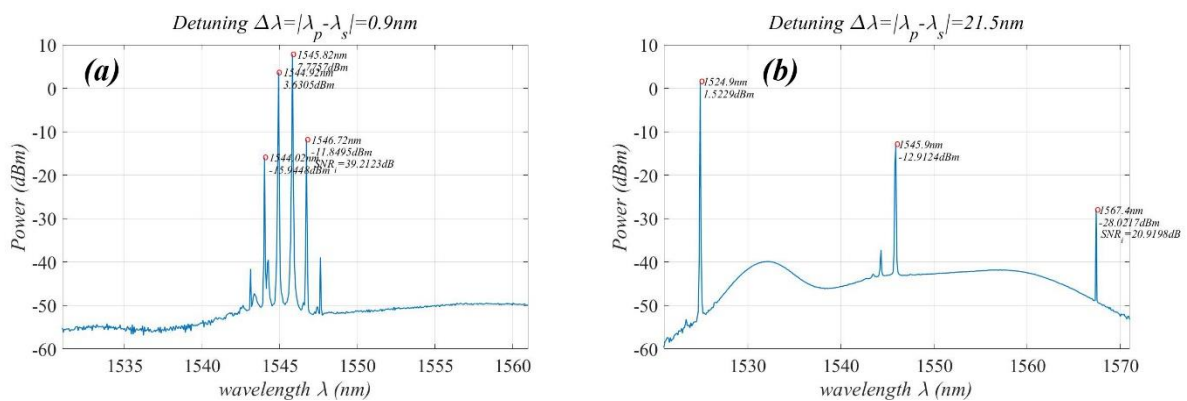


Figure 5.13 Measured FWM spectrum of HNLF1 by OSA. (a) FWM spectrum of the smallest detuning. (b) FWM spectrum of the largest detuning.

SNR_i and conversion efficiency of HNLF1 shows a similar trend in Figure 5.14. The conversion efficiency of HNLF 1 is overall higher than the SOI with slight detuning below 6 nm, and then drops to -30 dB with detuning increasing to 20 nm. SNR_i of HNLF1 below 6 nm detuning is generally 38 dB, which is higher than the SOI (around 32 dB) in the same region. However, it drops very fast when it exceeds 15 nm detuning, which is close to the boundary of the EDFA gain spectrum. SOI tested with the same EDFA shows a dropping trend over 20 nm detuning, which suggests the conversion band of SOI is wider than the conversion band of HNLF1.

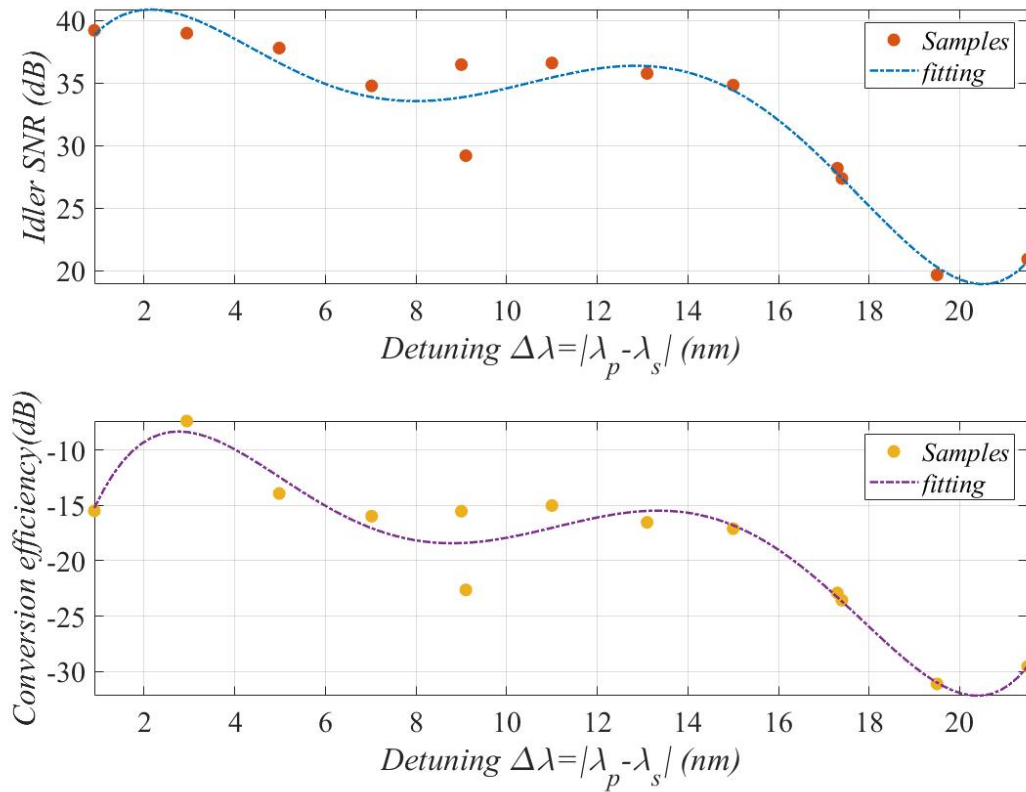


Figure 5.14 Measured wide band FWM results of HNLF1. (a) The SNR of idler SNR_i versus wavelength detuning $\Delta\lambda$, including sampled data points and fitting curve. (b) The conversion efficiency versus wavelength detuning $\Delta\lambda$, including sampled data points and fitting curve.

Another test is conducted on HNLF2, which is 100 meters of NL 1016 B fibre. The FWM spectrum for the smallest and largest sampling detuning point is shown below in Figure 5.15. Conversion in small detuning for HNLF2 is not good as HNLF1. The 2nd order FWM conversion is hard to be seen. The SNR of the idler also confirms this, as seen in Figure 5.16 (a), SNR_i is generally below 30 dB at detuning from 0 to 6 nm.

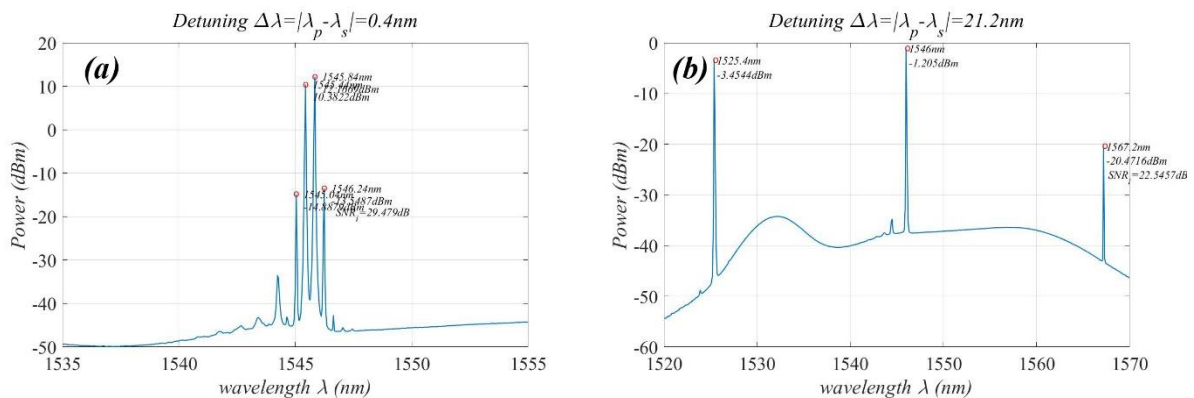


Figure 5.15 Measured FWM spectrum of HNL2 chip by OSA. (a) FWM spectrum of the smallest detuning. (b) FWM spectrum of the largest detuning.

SNR_i of HNL2 drops with increasing detuning. At the largest detuning, only 22 dB SNR remains. The conversion spectrum of HNL2 shows a strange trend and is different to the SNR spectrum. It fluctuates between -15 dB to -30 dB along the detuning band, suggesting inhomogeneous dispersion and poor quality for this particular HNL2.

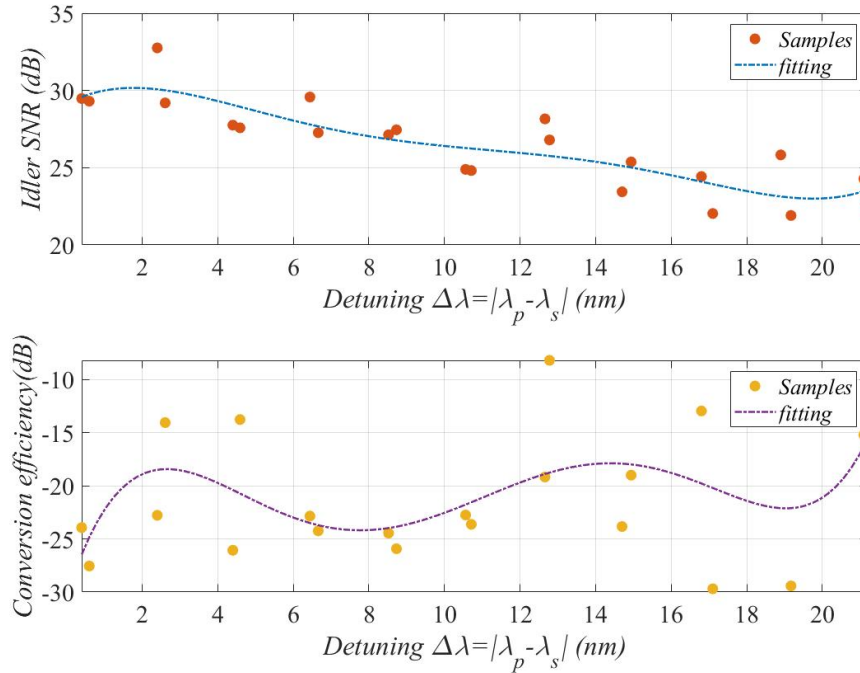


Figure 5.16 Measured wide band FWM results of HNL2. (a) The SNR of idler SNR_i versus wavelength detuning $\Delta\lambda$, including sampled data points and fitting curve. (b) The conversion efficiency versus wavelength detuning $\Delta\lambda$, including sampled data points and fitting curve.

Both conversion bands of two HNL2s are smaller than the SOI. The conversion efficiency of HNL2 is higher than the SOI at small detuning but drops faster than SOI with detuning increasing. HNL2's conversion efficiency is lower than SOI in the whole band.

5.3.3 Wideband FWM test of nonlinear SOA

The nonlinear SOA was successfully applied in dual-sweep FSI [5]. Therefore, the comparison with the FWM of non-linear SOA is also valuable for estimating the FWM of SOI. The testing system for non-linear SOA is slightly different from that for SOI and HNL2, the EDFA for the pump is removed because non-linear SOA is also working as an amplifier. However, A EDFA baseline is still observed in the FWM spectrum at the largest detuning due to EDFA for the signal source, as shown in Figure 5.17 (b). The Kamelian SOA was operated

with 300 mA current with 26 dB gain for the small signal. The FWM spectrum of non-linear SOA at smallest detuning also contains two clear peaks for 2nd order FWM conversion, which indicates high conversion for small detuning, but the idler peak at most significant detuning is small in both magnitude and SNR, which indicates narrow conversion band of non-linear SOA.

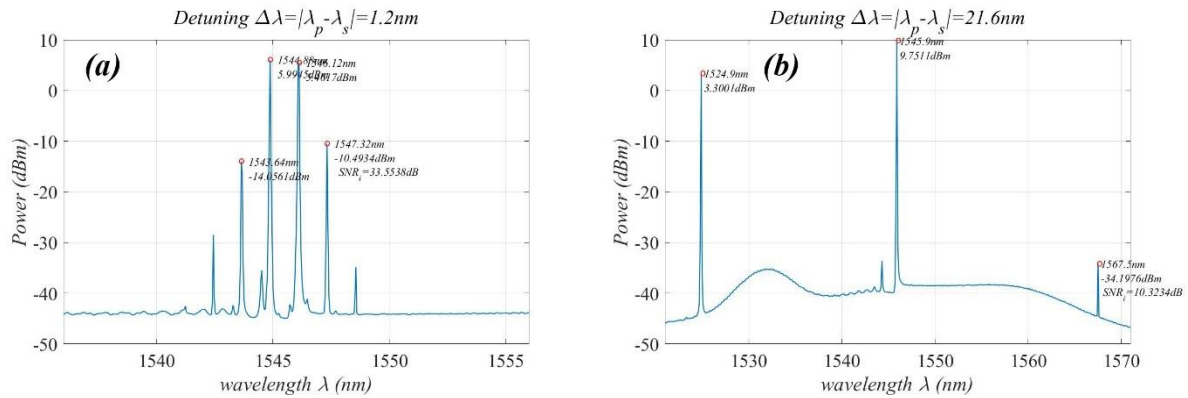


Figure 5.17 Measured FWM spectrum of Non-linear SOA by OSA. (a) FWM spectrum of the smallest detuning. (b) FWM spectrum of the largest detuning.

The wideband conversion efficiency and SNR spectrum also affirm this conclusion, as seen in Figure 5.18. Both SNR and conversion efficiency drop dramatically with increasing wavelength detuning. At the smallest detuning, 33.55 dB SNR and -10.5 dB conversion are acquired. The two numbers decrease to 10 dB and -40 dB at the largest detuning. That said, the conversion band of SOA is relatively narrow. The -3dB conversion bandwidth measure here is around 6 nm. With this poor idler signal quality, the dual-sweep FSI meets significant noise problems in data processing [5]. On the contrary, the SOI waveguide designed is tested for -3dB conversion bandwidth around 40 nm, which is promising to enhance the accuracy of dual-frequency FSI.

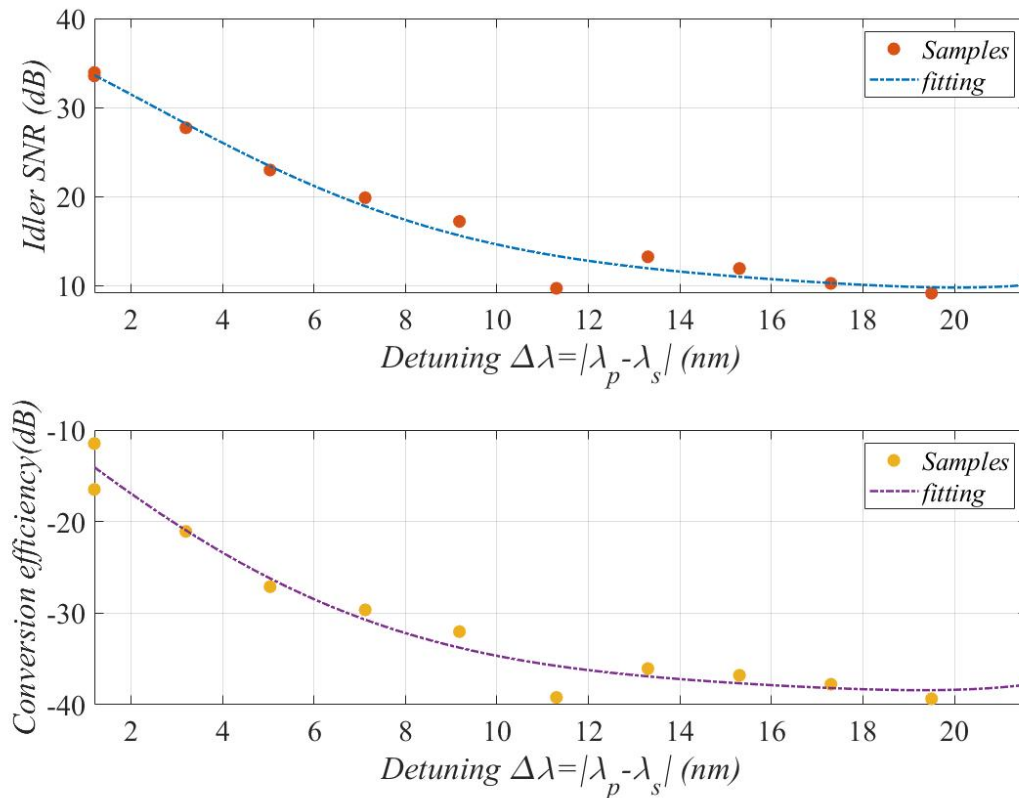


Figure 5.18 Measured wide band FWM results of Non-linear SOA. (a) The SNR of idler SNR_i versus wavelength detuning $\Delta\lambda$, including sampled data points and fitting curve. (b) The conversion efficiency versus wavelength detuning $\Delta\lambda$, including sampled data points and fitting curve.

5.4 Experiment 3: Dual-Frequency sweeping (filtered FWM) measurement

Dual-frequency sweeping laser output is tested based on the system for FWM. Essentially, the pump light is unwanted for generating the dual sweep laser output. Therefore, FWM output from the FWM module is filtered by a long pass and a notch filter to remove the signal light and pump light. The spectrum of the long-pass filter and notch filter is shown in Figure 5.19, the long-pass filter's cut-off wavelength is 1545 nm, which allows wavelength higher than 1545 nm to pass through, and the notch filter only reflected wavelength around 1546 nm. Only the idler peak from the FWM output remains with these two filters. However, applying these filters will also introduce extra losses on the idler peak; therefore, an extra EDFA3 is employed to compensate for the loss from filters. Output from EDFA 3 is then recombined with 10% of the original signal source to form the dual frequencies output. This complicated design removes

the pump peak of FWM, so the final output contains two sweeping peaks, namely the signal and idler light.

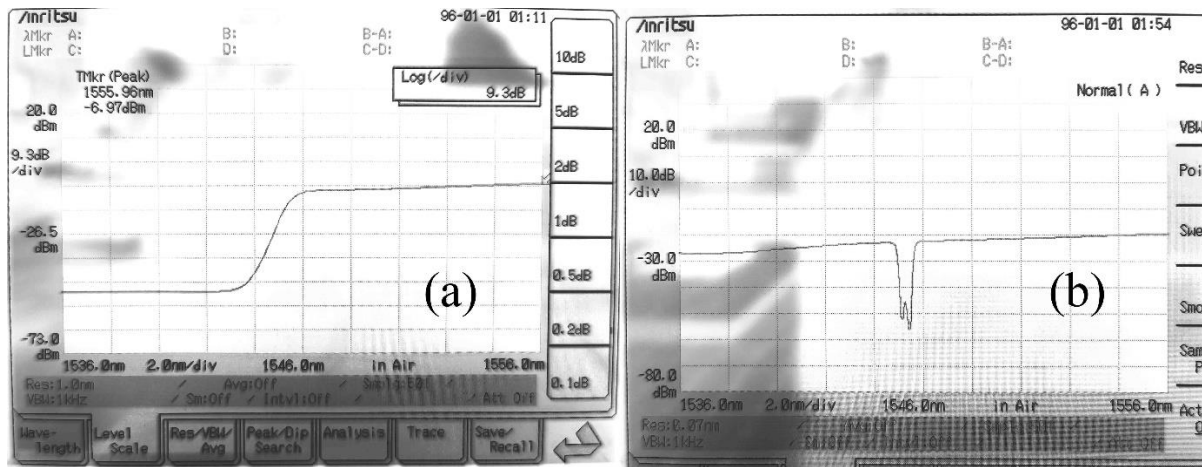


Figure 5.19 Transmission spectrums of long-pass and notch filter. (a) Long-pass filter. (b) Notch filter.

Figure 5.20 shows the dual sweeps generated on the SOI waveguide for different detuning wavelengths. A remained pump peak is located at the reference line named pump wavelength for each measurement. Due to the long pass filter, the idler side shows a higher baseline than the signal side. The SNR of the signal is higher than the SNR of the idler because signal light here is only amplified once; hence, a lower noise figure is introduced. The idler peak maintains a compatible magnitude with the signal peak, SNR_i reduces 3.1 dB from 1547. nm to 1561.68 nm, corresponding to 1,48 nm and 15.61 nm of detuning, respectively. For 20.8 nm of detuning, the baseline has risen since the expanded sampling range of OSA, and the idler remains at 20.6 dB of SNR.

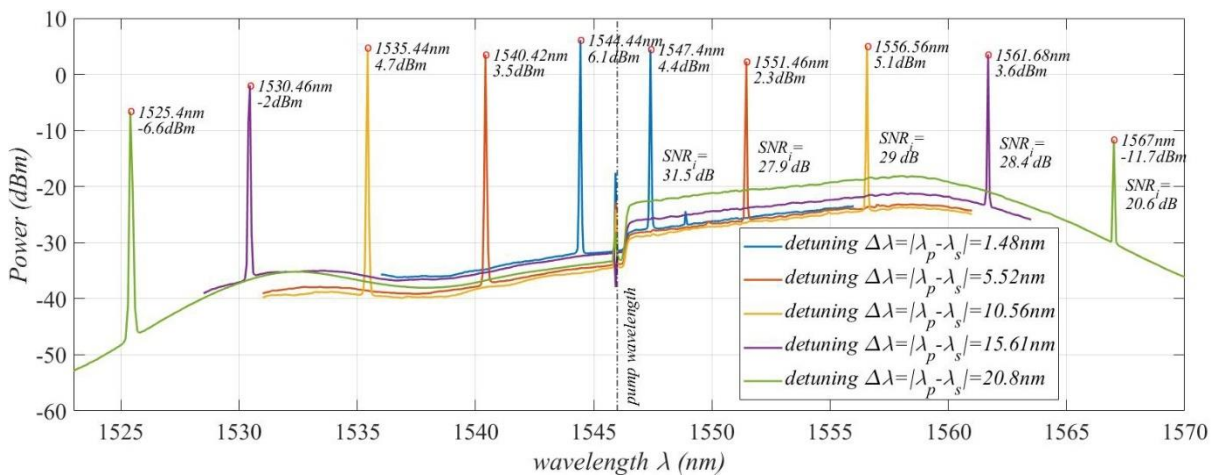


Figure 5.20 Dual sweeping generated by SOI waveguide. The left-side peaks are the filtered signal light plus the original signal light, and the right-side peaks are the idler peak after EDFA 3.

As mentioned in the last section, the left peak (signal peak) comprises 10% original signal light and long pass filtered signal light from FWM. At 20.8 nm detuning, the idler peak (-11.6956 dBm) of the SOI is still comparable with its signal peak (-6.6194 dBm). With the result shown, the dual-frequency sweeping laser output is achieved. It has a 20.8 nm detuning range and pump wavelength at 1546 nm, equivalent to a 1525.4 to 1567 nm tuning range, which is suitable enough to cover the whole C band, resulting in sufficient for dual-frequency FSI.

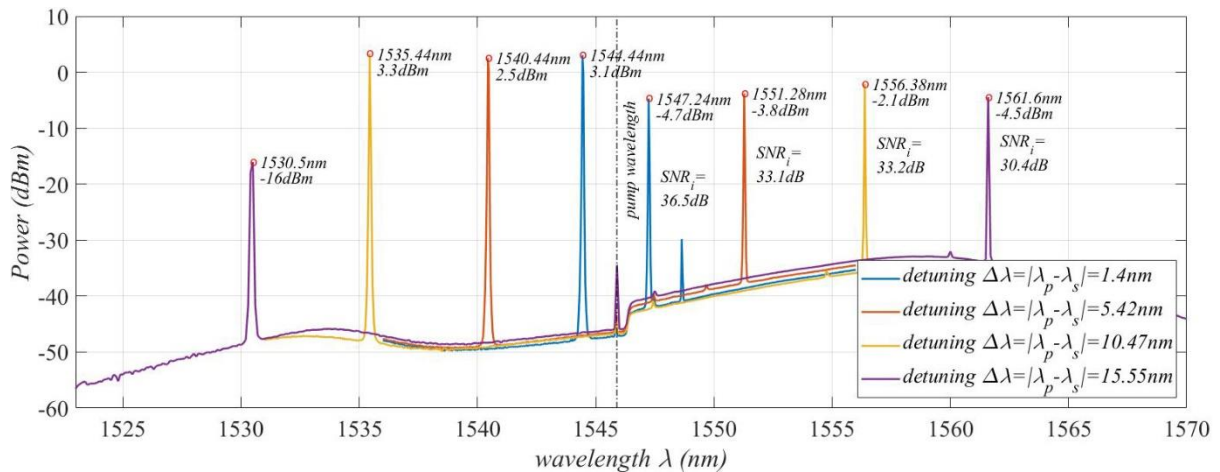


Figure 5.21 Dual sweeping generated by HNLf 1. The left-side peaks are the filtered signal light plus the original signal light, and the right-side peaks are the idler peak after EDFA 3.

Figure 5.21 and Figure 5.22 are the dual-sweep spectra generated by HNLf 1 and HNLf 2, respectively. Both spectrums contain a remained pump peak at the centre. In general, the SNR_i of HNLf1 is better than HNLf 2, over 30 dB SNR_i is seen for wavelength detuning below 15.55 nm on HNLf 1. Remarkably, the signal power of 15.55nm detuning is oddly smaller than the others, which is -16 dBm; however, the other signal peaks are 3.3, 2.5, and 3.1 dBm, respectively. This difference is caused by the change in OSA's sweeping range. As for HNLf 2, 26.5 dB SNR_i is witnessed at 20.7 nm detuning of wavelength, no significant drops towards SNR_i is seen with increasing detuning. jump of signal power is observed as well due to the OSA issue. The signal power for 1540.44 nm is significantly higher than the others.

Both HNLf 1 and HNLf 2 show decent dual sweep spectrum comparable to the SOI, and the HNLf 1 even perform higher SNR_i than SOI at a large detuning point. However, considering the scale of the devices, the capability of miniaturization of devices based on SOI is undeniable.

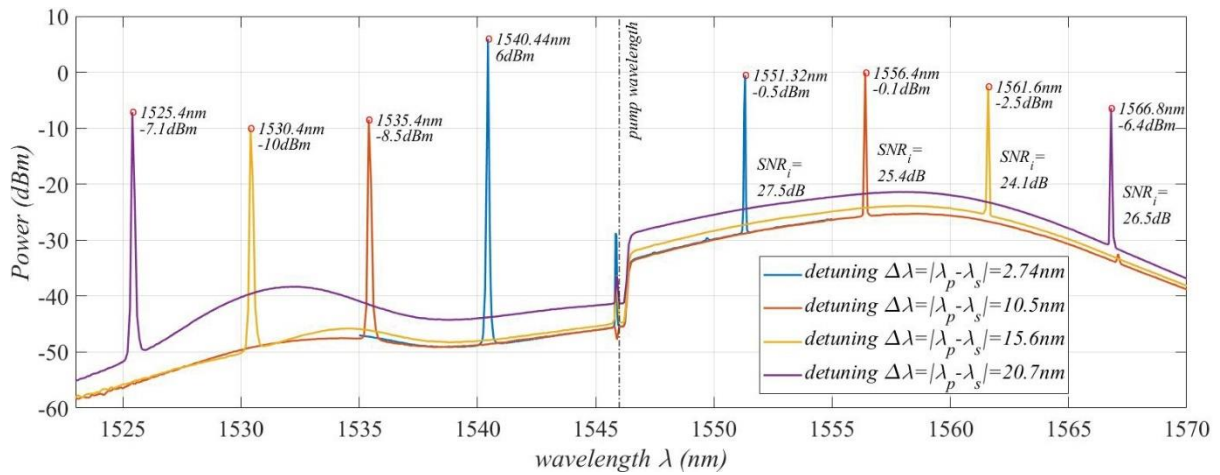


Figure 5.22 Dual sweeping generated by HNLF 2. The left-side peaks are the filtered signal light plus the original signal light, and the right-side peaks are the idler peak after EDFA 3.

Figure 5.23 shows the dual sweep spectrum of non-linear SOA, similar to the broadband FWM spectrum result of SOA shown in Figure 5.18; both power and SNR of idler peak drops dramatically with increasing wavelength detuning, which leads to noise for dual sweep FSI distance measurement [5].

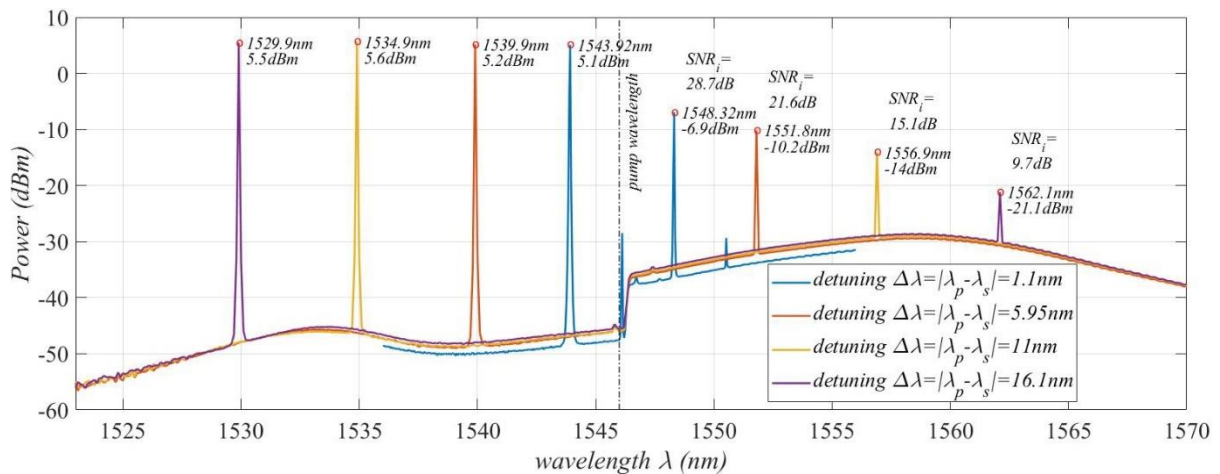


Figure 5.23 Dual sweeping generated by Non-linear SOA. The left-side peaks are the filtered signal light plus the original signal light, and the right-side peaks are the idler peak after EDFA 3.

In summary, the SOI show the best dual-sweep properties among the four devices. The experiment system based on SOI waveguide can supply an oppositely sweeping signal and idler laser output with comparable power along the whole C band. This dual sweeping laser is particularly suitable for a dual-frequency enhanced FSI distance measurement system.

5.5 Conclusion

The proposed devices are fabricated and analysed experimentally compared to other devices, including HNLF and non-linear SOA. Experiment results suggest that FWM on SOI waveguide is broader and higher than other devices, and the dual-sweep generated by SOI waveguide can cover the whole C band, which is promising for application in dual sweep FSI system.

Specifically, Table 5.6 compares the three FWM techniques based on the experimental results from three aspect including components dimension, usable conversion band for FSI and requirement of electric pump injection, particularly, the usable conversion bandwidth is taken as the -3dB dropping of idler SNR bandwidth. Obviously, the SOI waveguide achieves the widest usable band for FSI within the smallest dimension among all three techniques, which is best choice for highly compact dual-sweep FSI system. Both the two HNLF can achieve over 10 nm usable band, however, they require at least 100 metres length, which is far bigger than the SOI dimension (15 mm) and unsuitable for miniaturisation of FSI system. Where the Non-linear SOA has smaller dimension at centimetres level, but its usable conversion bandwidth is only 3 nm and it also require extra electric pump, which is difficult to be deployed in highly compact FSI system.

Table 5.6 Comparison among the FWM techniques based on experimental results

FWM conversion Devices	Component dimension	Usable conversion bandwidth for FSI	Extra electric pump
SOI waveguide	15 millimetres	23 nm	no
HNLF 1	100 meters length	15 nm	no
HNLF 2	100 metres length	13 nm	no
Non-linear SOA	Few centimetres	3 nm	yes

Chapter 6

Summary and Outlook

6.1 Contribution to knowledge

This thesis contributes towards the nanostructure design of OLEDs and photonic integrated devices for improving devices' performance and achieving specific objectives, respectively, here the imported conclusions and outcomes for whole thesis are listed.

- A novel TEOLED with grating on Ag anode to enhance the LEE is introduced. Simulation-based investigation indicates the enhancement of LEE by grating with various grating dimension parameters, which suggests improvements in LEE and angular emission profile by the grating on the anode. A 60% LEE enhancement is predicted.
- Then polarized OLED devices are focused. A refractive index grating structure in the EML of polarized OLED made by luminescent liquid crystal material to improve both the EQE and polarized ratio is introduced. This is the first example reported for index grating in EML formed by mesogenic molecules.
- The proposed polarized OLED structure is based on manipulating the molecules' orientation in the EML layer by patterned linearly polarized UV exposure. A polarized OLED structure with index grating inside the EMI and another with both grating-EML and extra crystallized EML is reported.
- A scheme of how the refractive index grating design influences the emission band, EQE, and polarized ratio is discussed based on the numerical simulation. The proposed structure's feasibility from both material and fabrication perspectives is discussed rigorously. 56% EQE and 19 dB polarized ratio are promising for the optimized design.
- A novel dual-sweep laser source achieved by FWM in SOI nano waveguide is developed. In particular, the two laser sweep synchronized with the same tuning speed and waveband but in opposite directions. In other words, a symmetrically dual-frequency sweeping laser is achieved.

- The dual-sweep laser source is proposed to be used in a dual-sweep FSI system for vibration compensation. The final design of SOI chips and corresponding edge couplers is proposed based on comprehensive numerical simulation and optimisation.
- The experiments were implemented to investigate not only the FWM conversion properties of fabricated SOI chips but also the HNLFs and non-linear SOA for comparison. The experiment reveals the advantages of SOI waveguides in FWM conversion bandwidth and efficiency; the proposed SOI chips design successfully achieves dual-sweep laser output covering the whole C band, which is promising for driving the dual-sweep FSI system and improving the accuracy of measurement. This is the first dual-sweep source for the FSI system based on SOI chips.

6.2 Limitation of work in thesis

- The designed polarized OLEDs devices haven't been fabricated and characterised experimentally, which could be addressed in future.
- The taper shape of the fibre-to-chip coupler could be further optimized to achieve higher coupling efficiency, curved taper has been reported, which is valuable to be investigated specifically.
- Scanning Electron Microscopy (SEM) wasn't implemented for the SOI chip analysis, which could suggest the reason for relatively poor coupling efficiency, for example, the side wall roughness and error of the cross-sectional shape of the waveguide.
- AR coating on the facet of the chip could further improve the coupling efficiency.

6.3 Prospective work

Future work for the polarized OLED design is to be done to expand the application of luminescent LC materials. First, Although the simulation results indicate that efficient OLED emission with a high polarized ratio can be achieved, the perfect alignment of molecules is unrealistic, and the degree of molecule orientation could impact the polarized ratio of real devices. This is essential to be addressed in the next stage of the study. Besides, this project's

next stage should cooperate with industrial partners to synthesize the derivation with rod-like molecules. By replacing the BDAVBi with other organic luminescent material with rod-like shape molecules [51] and adopting the optical design introduced in this thesis, enhanced the EQE of polarized OLEDs in other colours, including red and green, are possibly implemented. In addition, the polarized ratio could be further improved by eliminating the emission from the amorphous area, which is usually achieved by doping to decrease the conductivity of the amorphous area [4]. In addition, This exciting work enlightens a vast potential for other UV patternable photoreactive materials with broader applications in combining the organic semiconductor and nano-photonics such as nano colour filters [172].

The work on designing SOI chips can still be improved. Firstly, the maximum coupling efficiency achieved is -3.595 dB, which can be optimized by polishing and coating at both ends of the chip. The manual alignment inserts significant uncertainty into the experiment, which is addressable by the packaging process. The stability of SOI waveguides can be significantly enhanced after packaging with lensed fibre. Besides, other materials, including Ge-on-Si and III-V semiconductors, can also be used for FWM due to their promising $\chi^{(3)}$ properties.

Bibliography

- [1] G. E. Moore, "Cramming more components onto integrated circuits," *Proceedings of the IEEE*, vol. 86, no. 1, pp. 82-85, 1998.
- [2] L. Poldervaart and C. Sluijter, "Photonics: the profile of a new discipline," in *High Speed Photography*: Springer, 1975, pp. 585-591.
- [3] A. Einstein, "The photoelectric effect," *Ann. Phys*, vol. 17, no. 132, p. 4, 1905.
- [4] G. Koch and N. Copner, "Organic light emitting diode devices," Patent U.S. patent 9,130,193 B2, 2015.
- [5] J. J. Martinez, M. A. Campbell, M. S. Warden, E. Hughes, N. J. Copner, and A. Lewis, "Dual-sweep frequency scanning interferometry using four wave mixing," *IEEE Photonics Technology Letters*, vol. 27, no. 7, pp. 733-736, 2015.
- [6] K. Yee, "Numerical solution of initial boundary value problems involving Maxwell's equations in isotropic media," *IEEE Transactions on antennas propagation*, vol. 14, no. 3, pp. 302-307, 1966.
- [7] A. Taflove, S. C. Hagness, and M. Picket-May, "Computational electromagnetics: the finite-difference time-domain method," in *The Electrical Engineering Handbook*, vol. 3, 2005, pp. 629-670.
- [8] J.-P. Berenger, "A perfectly matched layer for the absorption of electromagnetic waves," *Journal of computational physics*, vol. 114, no. 2, pp. 185-200, 1994.
- [9] P. Harms, R. Mittra, and W. Ko, "Implementation of the periodic boundary condition in the finite-difference time-domain algorithm for FSS structures," *IEEE transactions on antennas propagation*, vol. 42, no. 9, pp. 1317-1324, 1994.
- [10] P. Mezzanotte, L. Roselli, and R. Sorrentino, "A simple way to model curved metal boundaries in FDTD algorithm avoiding staircase approximation," *IEEE microwave guided wave letters*, vol. 5, no. 8, pp. 267-269, 1995.
- [11] R. Courant, "Variational methods for the solution of problems of equilibrium and vibrations," *Lecture notes in pure applied mathematics*, pp. 1-1, 1994.
- [12] M. J. Turner, R. W. Clough, H. C. Martin, and L. Topp, "Stiffness and deflection analysis of complex structures," *journal of the Aeronautical Sciences*, vol. 23, no. 9, pp. 805-823, 1956.
- [13] K. Han and C.-H. Chang, "Numerical modeling of sub-wavelength anti-reflective structures for solar module applications," *Nanomaterials*, vol. 4, no. 1, pp. 87-128, 2014.
- [14] L. Bieniasz and D. Britz, "Recent developments in digital simulation of electroanalytical experiments," *Polish journal of chemistry*, vol. 78, no. 9, pp. 1195-1219, 2004.
- [15] J. J. Hench and Z. Strakoš, "The RCWA method-a case study with open questions and perspectives of algebraic computations," *Electronic Transactions on Numerical Analysis*, vol. 31, pp. 331-357, 2008.
- [16] J. Van Roey, J. Van der Donk, and P. Lagasse, "Beam-propagation method: analysis and assessment," *JOSA B*, vol. 71, no. 7, pp. 803-810, 1981.
- [17] A. H.-D. Cheng and D. T. Cheng, "Heritage and early history of the boundary element method," *Engineering analysis with boundary elements*, vol. 29, no. 3, pp. 268-302, 2005.
- [18] D. Qiao *et al.*, "Design and optical characterization of an efficient polarized organic light emitting diode based on refractive index modulation in the emitting layer," *Optics Express*, vol. 28, no. 26, pp. 40131-40144, 2020.
- [19] D. Qiao, K. Li, N. Copner, Y. Gong, and G. Chen, "The Enhanced Light Extraction Top-emitting Organic Light-emitting Diode Based on Metallic Grating Anode," in *2019 IEEE*

International Conference on Manipulation, Manufacturing and Measurement on the Nanoscale (3M-NANO), 2019, pp. 49-52: IEEE.

[20] C. W. Tang and S. A. VanSlyke, "Organic electroluminescent diodes," *Appl. Phys. Lett.*, vol. 51, no. 12, pp. 913-915, 1987.

[21] C. Adachi, M. A. Baldo, M. E. Thompson, and S. R. Forrest, "Nearly 100% internal phosphorescence efficiency in an organic light-emitting device," *Journal of Applied Physics*, vol. 90, no. 10, pp. 5048-5051, 2001.

[22] T. Yamasaki, K. Sumioka, and T. Tsutsui, "Organic light-emitting device with an ordered monolayer of silica microspheres as a scattering medium," *Appl. Phys. Lett.*, vol. 76, no. 10, pp. 1243-1245, 2000.

[23] Y. Qu, J. Kim, C. Coburn, and S. R. Forrest, "Efficient, nonintrusive outcoupling in organic light emitting devices using embedded microlens arrays," *ACS photonics*, vol. 5, no. 6, pp. 2453-2458, 2018.

[24] J.-G. Zhou *et al.*, "Nano-modified indium tin oxide incorporated with ideal microlens array for light extraction of OLED," *J. Mater. Chem. C*, vol. 7, no. 13, pp. 3958-3964, 2019.

[25] J. Yang, Q. Bao, Z. Xu, Y. Li, J. Tang, and S. Shen, "Light out-coupling enhancement of organic light-emitting devices with microlens array," *Appl. Phys. Lett.*, vol. 97, no. 22, p. 256, 2010.

[26] S. Möller and S. Forrest, "Improved light out-coupling in organic light emitting diodes employing ordered microlens arrays," *J. Appl. Phys.*, vol. 91, no. 5, pp. 3324-3327, 2002.

[27] Y. Sun and S. R. Forrest, "Organic light emitting devices with enhanced outcoupling via microlenses fabricated by imprint lithography," *J. Appl. Phys.*, vol. 100, no. 7, p. 073106, 2006.

[28] H.-W. Chang *et al.*, "Nano-particle based scattering layers for optical efficiency enhancement of organic light-emitting diodes and organic solar cells," *J. Appl. Phys.*, vol. 113, no. 20, p. 204502, 2013.

[29] C. Lee and J. J. Kim, "Enhanced light out-coupling of OLEDs with low haze by inserting randomly dispersed nanopillar arrays formed by lateral phase separation of polymer blends," *Small*, vol. 9, no. 22, pp. 3858-3863, 2013.

[30] T.-W. Koh, J. A. Spechler, K. M. Lee, C. B. Arnold, and B. P. Rand, "Enhanced outcoupling in organic light-emitting diodes via a high-index contrast scattering layer," *ACS photonics*, vol. 2, no. 9, pp. 1366-1372, 2015.

[31] W. H. Koo *et al.*, "Light extraction from organic light-emitting diodes enhanced by spontaneously formed buckles," *Nat. Photonics*, vol. 4, no. 4, pp. 222-226, 2010.

[32] J.-H. Jang, M.-C. Oh, T.-H. Yoon, and J. C. Kim, "Polymer grating imbedded organic light emitting diodes with improved out-coupling efficiency," *Appl. Phys. Lett.*, vol. 97, no. 12, p. 203, 2010.

[33] H. Liang *et al.*, "Corrugated organic light-emitting diodes to effectively extract internal modes," *Opt. Express*, vol. 27, no. 8, pp. A372-A384, Apr 15 2019.

[34] Y. R. Do, Y.-C. Kim, Y.-W. Song, and Y.-H. Lee, "Enhanced light extraction efficiency from organic light emitting diodes by insertion of a two-dimensional photonic crystal structure," *Journal of Applied Physics*, vol. 96, no. 12, pp. 7629-7636, 2004.

[35] Y. Sun and S. R. Forrest, "Enhanced light out-coupling of organic light-emitting devices using embedded low-index grids," *Nat. Photonics*, vol. 2, no. 8, pp. 483-487, 2008.

[36] T. W. Koh, J. M. Choi, S. Lee, and S. Yoo, "Optical outcoupling enhancement in organic light-emitting diodes: highly conductive polymer as a low-index layer on microstructured ITO electrodes," *Adv. Mater.*, vol. 22, no. 16, pp. 1849-1853, 2010.

[37] M. Slights and S. R. Forrest, "Enhancing waveguided light extraction in organic LEDs using an ultra-low-index grid," *Opt. Lett.*, vol. 35, no. 7, pp. 1052-1054, 2010.

- [38] T. W. Koh, J. M. Choi, S. Lee, and S. Yoo, "Optical outcoupling enhancement in organic light-emitting diodes: highly conductive polymer as a low-index layer on microstructured ITO electrodes," *Adv Mater*, vol. 22, no. 16, pp. 1849-53, Apr 22 2010.
- [39] H. Peng, M. Wong, and H. S. Kwok, "Design and Characterization of Organic Light Emitting Diodes with Microcavity Structure," in *SID Symposium Digest of Technical Papers*, 2003, vol. 34, no. 1, pp. 516-519: Wiley Online Library.
- [40] C.-H. Chang, T.-F. Chang, Y.-H. Liang, Y.-J. Lo, Y.-J. Wu, and H.-H. Chang, "Improving the outcoupling efficiency of white organic light-emitting devices based on a gradient refractive index substrate," *Japanese Journal of Applied Physics*, vol. 55, no. 3S1, 2016.
- [41] G. Gu, V. Bulović, P. Burrows, S. Forrest, and M. Thompson, "Transparent organic light emitting devices," *Applied Physics Letters*, vol. 68, no. 19, pp. 2606-2608, 1996.
- [42] G. Parthasarathy, P. Burrows, V. Khalfin, V. Kozlov, and S. Forrest, "A metal-free cathode for organic semiconductor devices," *Applied Physics Letters*, vol. 72, no. 17, pp. 2138-2140, 1998.
- [43] N. Naghavi, A. Rougier, C. Marcel, C. Guery, J. Leriche, and J. Tarascon, "Characterization of indium zinc oxide thin films prepared by pulsed laser deposition using a Zn₃In₂O₆ target," *Thin Solid Films*, vol. 360, no. 1-2, pp. 233-240, 2000.
- [44] K. Fuchs, "The conductivity of thin metallic films according to the electron theory of metals," in *Mathematical Proceedings of the Cambridge Philosophical Society*, 1938, vol. 34, no. 1, pp. 100-108: Cambridge University Press.
- [45] R. Pode, C. Lee, D. Moon, and J. Han, "Transparent conducting metal electrode for top emission organic light-emitting devices: Ca-Ag double layer," *Applied physics letters*, vol. 84, no. 23, pp. 4614-4616, 2004.
- [46] J. Cesario, M. U. Gonzalez, S. Cheylan, W. L. Barnes, S. Enoch, and R. Quidant, "Coupling localized and extended plasmons to improve the light extraction through metal films," *Optics express*, vol. 15, no. 17, pp. 10533-10539, 2007.
- [47] J.-H. Jang, M.-C. Oh, T.-H. Yoon, and J. C. Kim, "Polymer grating imbedded organic light emitting diodes with improved out-coupling efficiency," *Applied Physics Letters*, vol. 97, no. 12, 2010.
- [48] Y. Sun and S. R. Forrest, "Organic light emitting devices with enhanced outcoupling via microlenses fabricated by imprint lithography," *Journal of applied physics*, vol. 100, no. 7, p. 073106, 2006.
- [49] H. Wang *et al.*, "Smooth ZnO: Al-AgNWs composite electrode for flexible organic light-emitting device," *Nanoscale research letters*, vol. 12, no. 1, pp. 1-7, 2017.
- [50] P. Dyreklev, M. Berggren, O. Inganäs, M. R. Andersson, O. Wennerström, and T. Hjertberg, "Polarized electroluminescence from an oriented substituted polythiophene in a light emitting diode," *Adv. Mater.*, vol. 7, no. 1, pp. 43-45, 1995.
- [51] M. Jandke, P. Stroehriegl, J. Gmeiner, W. Brütting, and M. Schworer, "Polarized Electroluminescence from Rubbing-Aligned Poly (p-phenylenevinylene)," *Adv. Mater.*, vol. 11, no. 18, pp. 1518-1521, 1999.
- [52] V. Cimrová, M. Remmers, D. Neher, and G. Wegner, "Polarized light emission from LEDs prepared by the Langmuir-Blodgett technique," *Adv. Mater.*, vol. 8, no. 2, pp. 146-149, 1996.
- [53] D.-M. Lee, Y.-J. Lee, J.-H. Kim, and C.-J. Yu, "Birefringence-dependent linearly-polarized emission in a liquid crystalline organic light emitting polymer," *Opt. Express*, vol. 25, no. 4, pp. 3737-3742, 2017.
- [54] D. Yokoyama, "Molecular orientation in small-molecule organic light-emitting diodes," *J. Mater. Chem.*, vol. 21, no. 48, pp. 19187-19202, 2011.

- [55] T. Höfler, M. Weinberger, W. Kern, S. Rentenberger, and A. Pogantsch, "Modifying the Output Characteristics of an Organic Light-Emitting Device by Refractive-Index Modulation," *Adv. Funct. Mater.*, vol. 16, no. 18, pp. 2369-2373, 2006.
- [56] L. Wang, J. Amano, and P.-C. Hung, "Simulating Plasmon Effect in Nanostructured OLED Cathode Using Finite Element Method," *Konica Minolta technology report*, vol. 13, pp. 101-106, 2016.
- [57] Z. B. Wang *et al.*, "Optical design of organic light emitting diodes," *Journal of Applied Physics*, vol. 109, no. 5, 2011.
- [58] G. Koch, "Liquid crystal photoalignment materials.," Patent U.S. patent 9,508,942 B2, 2016.
- [59] Y. Wang *et al.*, "Highly efficient blueish-green fluorescent OLEDs based on AIE liquid crystal molecules: from ingenious molecular design to multifunction materials," *Journal of Materials Chemistry C*, vol. 5, no. 16, pp. 3999-4008, 2017.
- [60] L.-X. Guo *et al.*, "Luminescent liquid crystals bearing an aggregation-induced emission active tetraphenylthiophene fluorophore," *Journal of Materials Chemistry C*, vol. 7, no. 16, pp. 4828-4837, 2019.
- [61] S. Kim, B. Kim, J. Lee, H. Shin, Y.-I. Park, and J. Park, "Design of fluorescent blue light-emitting materials based on analyses of chemical structures and their effects," *Materials Science Engineering: R: Reports*, vol. 99, pp. 1-22, 2016.
- [62] T. Hagler, K. Pakbaz, and A. Heeger, "Polarized-electroabsorption spectroscopy of a soluble derivative of poly (p-phenylenevinylene) oriented by gel processing in polyethylene: Polarization anisotropy, the off-axis dipole moment, and excited-state delocalization," *Physical Review B*, vol. 49, no. 16, p. 10968, 1994.
- [63] A. E. Contoret *et al.*, "The photopolymerization and cross-linking of electroluminescent liquid crystals containing methacrylate and diene photopolymerizable end groups for multilayer organic light-emitting diodes," *Chemistry of materials*, vol. 14, no. 4, pp. 1477-1487, 2002.
- [64] K. J. C. r. Ichimura, "Photoalignment of liquid-crystal systems," vol. 100, no. 5, pp. 1847-1874, 2000.
- [65] R. Harding, A. L. May, S. Greenfield, J. Lub, C. Doornkamp, and R. T. Wegh, "Alignment layer with reactive mesogens for aligning liquid crystal molecules," Patent U.S. patent 8.481,130 B2 2013.
- [66] C. Selvarasu and P. Kannan, "Synthesis, characterization of azobenzene and cinnamate ester based calamitic liquid crystalline compounds and their photoresponsive properties," *Journal of Molecular Structure*, vol. 1092, pp. 176-186, 2015.
- [67] K. Ichimura, "Photoalignment of liquid-crystal systems," *Chem. Rev.*, vol. 100, no. 5, pp. 1847-1874, 2000.
- [68] S. Ishihara and M. Mizusaki, "Alignment control technology of liquid crystal molecules," *J. Soc. Inf. Display*, vol. 28, no. 1, pp. 44-74, 2019.
- [69] V. G. Chigrinov, V. M. Kozenkov, and H.-S. Kwok, *Photoalignment of liquid crystalline materials: physics and applications*. John Wiley & Sons, 2008.
- [70] H. Tokuhisa, M. Era, and T. Tsutsui, "Novel liquid crystalline oxadiazole with high electron mobility," *Advanced Materials*, vol. 10, no. 5, pp. 404-406, 1998.
- [71] S. H. Kim, I. Cho, M. K. Sim, S. Park, and S. Y. Park, "Highly efficient deep-blue emitting organic light emitting diode based on the multifunctional fluorescent molecule comprising covalently bonded carbazole and anthracene moieties," *J. Mater. Chem.*, vol. 21, no. 25, pp. 9139-9148, 2011.
- [72] D. Yokoyama, K. Nakayama, T. Otani, and J. Kido, "Wide-range refractive index control of organic semiconductor films toward advanced optical design of organic optoelectronic devices," *Adv. Mater.*, vol. 24, no. 47, pp. 6368-73, Dec 11 2012.

- [73] D. Yokoyama, A. Sakaguchi, M. Suzuki, and C. Adachi, "Horizontal orientation of linear-shaped organic molecules having bulky substituents in neat and doped vacuum-deposited amorphous films," *Organic Electronics*, vol. 10, no. 1, pp. 127-137, 2009.
- [74] A. Salehi, X. Fu, D. H. Shin, and F. So, "Recent Advances in OLED Optical Design," *Adv. Funct. Mater.*, vol. 29, no. 15, p. 1808803, 2019.
- [75] J. W. Kim *et al.*, "FDTD analysis of the light extraction efficiency of OLEDs with a random scattering layer," *Opt. Express*, vol. 22, no. 1, pp. 498-507, Jan 13 2014.
- [76] H. Cho *et al.*, "Importance of Purcell factor for optimizing structure of organic light-emitting diodes," *Opt. Express*, vol. 27, no. 8, pp. 11057-11068, Apr 15 2019.
- [77] L. Zhou *et al.*, "Highly linearly polarized light emission from flexible organic light-emitting devices capitalized on integrated ultrathin metal-dielectric nanograting," *Opt. Express*, vol. 28, no. 9, pp. 13826-13836, Apr 27 2020.
- [78] K. A. Neyts, "Simulation of light emission from thin-film microcavities," *J. Opt. Soc. Am. A*, vol. 15, no. 4, pp. 962-971, 1998.
- [79] J. Frischeisen *et al.*, "Light extraction from surface plasmons and waveguide modes in an organic light-emitting layer by nanoimprinted gratings," *Opt. Express*, vol. 19, no. 101, pp. A7-A19, 2011.
- [80] Y. Wang, J. Shi, J. Chen, W. Zhu, and E. Baranoff, "Recent progress in luminescent liquid crystal materials: design, properties and application for linearly polarised emission," *J. Mater. Chem. C*, vol. 3, no. 31, pp. 7993-8005, 2015.
- [81] S. E. Miller, "Integrated optics: An introduction," *J The Bell System Technical Journal*, vol. 48, no. 7, pp. 2059-2069, 1969.
- [82] S. Somekh and A. Yarive, "Fiber optic communications," in *Proc. Conf. International Telemetry, Los Angeles.(407-418)*, 1972.
- [83] L. Arizmendi, "Photonic applications of lithium niobate crystals," *physica status solidi*, vol. 201, no. 2, pp. 253-283, 2004.
- [84] M. Li, J. Ling, Y. He, U. A. Javid, S. Xue, and Q. Lin, "Lithium niobate photonic-crystal electro-optic modulator," *Nature Communications*, vol. 11, no. 1, pp. 1-8, 2020.
- [85] J. Petykiewicz *et al.*, "Direct bandgap light emission from strained germanium nanowires coupled with high-Q nanophotonic cavities," *Nano letters*, vol. 16, no. 4, pp. 2168-2173, 2016.
- [86] M. Grabherr, R. Jager, R. Michalzik, B. Weigl, G. Reiner, and K. J. Ebeling, "Efficient single-mode oxide-confined GaAs VCSEL's emitting in the 850-nm wavelength regime," *IEEE Photonics Technology Letters*, vol. 9, no. 10, pp. 1304-1306, 1997.
- [87] T. Wood *et al.*, "High-speed optical modulation with GaAs/GaAlAs quantum wells in ap-i-n diode structure," *Applied Physics Letters*, vol. 44, no. 1, pp. 16-18, 1984.
- [88] D. Liang and J. Bowers, "Photonic integration: Si or InP substrates?," *Electronics Letters*, vol. 45, no. 12, pp. 578-581, 2009.
- [89] S. Saeidi, K. M. Awan, L. Sirbu, and K. Dolgaleva, "Nonlinear photonics on-a-chip in III-V semiconductors: quest for promising material candidates," *Applied optics*, vol. 56, no. 19, pp. 5532-5541, 2017.
- [90] M. Pu *et al.*, "Ultra-Efficient and Broadband Nonlinear AlGaAs-on-Insulator Chip for Low-Power Optical Signal Processing," *Laser & Photonics Reviews*, vol. 12, no. 12, p. 1800111, 2018.
- [91] C. O. de Beeck *et al.*, "III/V-on-lithium niobate amplifiers and lasers," *Optical Engineering*, vol. 8, no. 10, pp. 1288-1289, 2021.
- [92] M. L. Davenport, S. Skendžić, N. Volet, J. C. Hulme, M. J. Heck, and J. E. Bowers, "Heterogeneous silicon/III-V semiconductor optical amplifiers," *IEEE Journal of Selected Topics in Quantum Electronics*, vol. 22, no. 6, pp. 78-88, 2016.

- [93] Z. Yin and X. Tang, "A review of energy bandgap engineering in III–V semiconductor alloys for mid-infrared laser applications," *Solid-state electronics*, vol. 51, no. 1, pp. 6-15, 2007.
- [94] R. LaPierre, M. Robson, K. Azizur-Rahman, and P. Kuyanov, "A review of III–V nanowire infrared photodetectors and sensors," *Journal of Physics D: Applied Physics*, vol. 50, no. 12, p. 123001, 2017.
- [95] M. Kawachi, "Silica waveguides on silicon and their application to integrated-optic components," *Optical Quantum Electronics*, vol. 22, no. 5, pp. 391-416, 1990.
- [96] R. Kashyap, G. D. Maxwell, and D. L. Williams, "Photoconduction in germanium and phosphorus doped silica waveguides," *Applied physics letters*, vol. 62, no. 3, pp. 214-216, 1993.
- [97] C. F. Kane and R. R. Krchnavek, "Benzocyclobutene optical waveguides," *IEEE photonics technology letters*, vol. 7, no. 5, pp. 535-537, 1995.
- [98] T. Sum, A. Bettiol, H. Seng, I. Rajta, J. Van Kan, and F. Watt, "Proton beam writing of passive waveguides in PMMA," *Nuclear Instruments Methods in Physics Research Section B: Beam Interactions with Materials Atoms*, vol. 210, pp. 266-271, 2003.
- [99] M. Nordström, D. A. Zauner, A. Boisen, and J. Hübner, "Single-mode waveguides with SU-8 polymer core and cladding for MOEMS applications," *Journal of Lightwave Technology*, vol. 25, no. 5, pp. 1284-1289, 2007.
- [100] D. J. Blumenthal, R. Heideman, D. Geuzebroek, A. Leinse, and C. Roeloffzen, "Silicon nitride in silicon photonics," *Proceedings of the IEEE*, vol. 106, no. 12, pp. 2209-2231, 2018.
- [101] R. Baets *et al.*, "Silicon Photonics: silicon nitride versus silicon-on-insulator," in *Optical Fiber Communication Conference*, 2016, p. Th3J. 1: Optical Society of America.
- [102] L. Chrostowski and M. Hochberg, *Silicon photonics design: from devices to systems*. Cambridge University Press, 2015.
- [103] D. Taillaert, P. Bienstman, and R. Baets, "Compact efficient broadband grating coupler for silicon-on-insulator waveguides," *Optics letters*, vol. 29, no. 23, pp. 2749-2751, 2004.
- [104] T. Tsuchizawa *et al.*, "Microphotonics devices based on silicon microfabrication technology," *IEEE Journal of selected topics in quantum electronics*, vol. 11, no. 1, pp. 232-240, 2005.
- [105] K. Isamoto, K. Kato, A. Morosawa, C. Chong, H. Fujita, and H. Toshiyoshi, "A 5-V operated MEMS variable optical attenuator by SOI bulk micromachining," *IEEE Journal of selected topics in quantum electronics*, vol. 10, no. 3, pp. 570-578, 2004.
- [106] J. Song *et al.*, "Fast and low power Michelson interferometer thermo-optical switch on SOI," *Optics express*, vol. 16, no. 20, pp. 15304-15311, 2008.
- [107] M. Nedeljkovic *et al.*, "Mid-infrared thermo-optic modulators in SoI," *IEEE Photonics Technology Letters*, vol. 26, no. 13, pp. 1352-1355, 2014.
- [108] T. Shoji, T. Tsuchizawa, T. Watanabe, K. Yamada, and H. Morita, "Low loss mode size converter from 0.3 μm square Si wire waveguides to singlemode fibres," *Electronics Letters*, vol. 38, no. 25, pp. 1669-1670, 2002.
- [109] H. Inoue, K. Hiruma, K. Ishida, T. Asai, and H. Matsumura, "Low loss GaAs optical waveguides," *IEEE Transactions on Electron Devices*, vol. 32, no. 12, pp. 2662-2668, 1985.
- [110] D. Dai, Y. Tang, and J. E. Bowers, "Mode conversion in tapered submicron silicon ridge optical waveguides," *Optics express*, vol. 20, no. 12, pp. 13425-13439, 2012.
- [111] Q. Xu, V. R. Almeida, R. R. Panepucci, and M. Lipson, "Experimental demonstration of guiding and confining light in nanometer-size low-refractive-index material," *Optics letters*, vol. 29, no. 14, pp. 1626-1628, 2004.
- [112] V. M. Passaro and M. La Notte, "Optimizing SOI slot waveguide fabrication tolerances and strip-slot coupling for very efficient optical sensing," *Sensors*, vol. 12, no. 3, pp. 2436-2455, 2012.

- [113] Y. Xu, R. K. Lee, and A. Yariv, "Propagation and second-harmonic generation of electromagnetic waves in a coupled-resonator optical waveguide," *JOSA B*, vol. 17, no. 3, pp. 387-400, 2000.
- [114] I. Avrutsky and R. Soref, "Phase-matched sum frequency generation in strained silicon waveguides using their second-order nonlinear optical susceptibility," *Optics express*, vol. 19, no. 22, pp. 21707-21716, 2011.
- [115] C. Monat *et al.*, "Integrated optical auto-correlator based on third-harmonic generation in a silicon photonic crystal waveguide," *Nature communications*, vol. 5, no. 1, pp. 1-8, 2014.
- [116] M. A. Foster, A. C. Turner, J. E. Sharping, B. S. Schmidt, M. Lipson, and A. L. Gaeta, "Broad-band optical parametric gain on a silicon photonic chip," *Nature*, vol. 441, no. 7096, pp. 960-963, 2006.
- [117] G. P. Agrawal, "Nonlinear fiber optics," in *Nonlinear Science at the Dawn of the 21st Century*: Springer, 2000, pp. 195-211.
- [118] D. Tan, K. Ikeda, P. Sun, and Y. Fainman, "Group velocity dispersion and self phase modulation in silicon nitride waveguides," *Applied Physics Letters*, vol. 96, no. 6, p. 061101, 2010.
- [119] V. G. Ta'eed *et al.*, "All optical wavelength conversion via cross phase modulation in chalcogenide glass rib waveguides," *Optics express*, vol. 14, no. 23, pp. 11242-11247, 2006.
- [120] A. Liu, H. Rong, M. Paniccia, O. Cohen, and D. Hak, "Net optical gain in a low loss silicon-on-insulator waveguide by stimulated Raman scattering," *Optics Express*, vol. 12, no. 18, pp. 4261-4268, 2004.
- [121] F. Poletti, M. N. Petrovich, and D. J. Richardson, "Hollow-core photonic bandgap fibers: technology and applications," *Nanophotonics*, vol. 2, no. 5-6, pp. 315-340, 2013.
- [122] Q. Lin, O. J. Painter, and G. P. Agrawal, "Nonlinear optical phenomena in silicon waveguides: modeling and applications," *Optics express*, vol. 15, no. 25, pp. 16604-16644, 2007.
- [123] M. A. Foster, A. C. Turner, R. Salem, M. Lipson, and A. L. Gaeta, "Broad-band continuous-wave parametric wavelength conversion in silicon nanowaveguides," *Optics Express*, vol. 15, no. 20, pp. 12949-12958, 2007.
- [124] Z. Wang, H. Liu, N. Huang, Q. Sun, and J. Wen, "Impact of dispersion profiles of silicon waveguides on optical parametric amplification in the femtosecond regime," *Optics express*, vol. 19, no. 24, pp. 24730-24737, 2011.
- [125] T. Gu *et al.*, "Regenerative oscillation and four-wave mixing in graphene optoelectronics," *Nature photonics*, vol. 6, no. 8, pp. 554-559, 2012.
- [126] S. K. Turitsyn, A. E. Bednyakova, M. P. Fedoruk, S. B. Papernyi, and W. R. Clements, "Inverse four-wave mixing and self-parametric amplification in optical fibre," *Nature photonics*, vol. 9, no. 9, pp. 608-614, 2015.
- [127] X. Xue *et al.*, "Second-harmonic-assisted four-wave mixing in chip-based microresonator frequency comb generation," *Light: Science Applications*, vol. 6, no. 4, pp. e16253-e16253, 2017.
- [128] C. Lu, G. Liu, B. Liu, F. Chen, and Y. Gan, "Absolute distance measurement system with micron-grade measurement uncertainty and 24 m range using frequency scanning interferometry with compensation of environmental vibration," *Optics express*, vol. 24, no. 26, pp. 30215-30224, 2016.
- [129] K. Umetsu, R. Furutnani, S. Osawa, T. Takatsuji, and T. Kurosawa, "Geometric calibration of a coordinate measuring machine using a laser tracking system," *Measurement science technology*, vol. 16, no. 12, p. 2466, 2005.
- [130] R. Schneider, P. Thuermel, and M. Stockmann, "Distance measurement of moving objects by frequency modulated laser radar," *Optical Engineering*, vol. 40, no. 1, pp. 33-37, 2001.

- [131] M. Tatham, G. Sherlock, and L. Westbrook, "20-nm optical wavelength conversion using nondegenerate four-wave mixing," *IEEE photonics technology letters*, vol. 5, no. 11, pp. 1303-1306, 1993.
- [132] T. Durhuus, B. Mikkelsen, C. Joergensen, S. L. Danielsen, and K. E. Stubkjaer, "All-optical wavelength conversion by semiconductor optical amplifiers," *Journal of Lightwave technology*, vol. 14, no. 6, pp. 942-954, 1996.
- [133] P. Dumon *et al.*, "Linear and nonlinear nanophotonic devices based on silicon-on-insulator wire waveguides," *Japanese journal of applied physics*, vol. 45, no. 8S, p. 6589, 2006.
- [134] M. G ppert-Mayer, "ber Elementarakte mit zwei Quantenspr ngen," *Annalen der Physik*, vol. 401, no. 3, pp. 273-294, 1931.
- [135] T. H. Maiman, *Stimulated optical radiation in ruby*. 1960.
- [136] N. V. Tkachenko, *Optical spectroscopy: methods and instrumentations*. Elsevier, 2006.
- [137] J. Leuthold, C. Koos, and W. Freude, "Nonlinear silicon photonics," *Nature photonics*, vol. 4, no. 8, pp. 535-544, 2010.
- [138] H. Garcia and R. Kalyanaraman, "Phonon-assisted two-photon absorption in the presence of a dc-field: the nonlinear Franz-Keldysh effect in indirect gap semiconductors," *Journal of Physics B: Atomic, Molecular Optical Physics*, vol. 39, no. 12, p. 2737, 2006.
- [139] A. D. Bristow, N. Rotenberg, and H. M. Van Driel, "Two-photon absorption and Kerr coefficients of silicon for 850–2200 nm," *Applied Physics Letters*, vol. 90, no. 19, p. 191104, 2007.
- [140] T.-K. Liang and H.-K. Tsang, "Nonlinear absorption and Raman scattering in silicon-on-insulator optical waveguides," *IEEE Journal of Selected Topics in Quantum Electronics*, vol. 10, no. 5, pp. 1149-1153, 2004.
- [141] R. Jones *et al.*, "Net continuous wave optical gain in a low loss silicon-on-insulator waveguide by stimulated Raman scattering," *Optics Express*, vol. 13, no. 2, pp. 519-525, 2005.
- [142] H. Rong, A. Liu, R. Nicolaescu, M. Paniccia, O. Cohen, and D. Hak, "Raman gain and nonlinear optical absorption measurements in a low-loss silicon waveguide," *Applied physics letters*, vol. 85, no. 12, pp. 2196-2198, 2004.
- [143] R. Soref and B. Bennett, "Electrooptical effects in silicon," *IEEE journal of quantum electronics*, vol. 23, no. 1, pp. 123-129, 1987.
- [144] R. Van Laer, B. Kuyken, D. Van Thourhout, and R. Baets, "Interaction between light and highly confined hypersound in a silicon photonic nanowire," *Nature Photonics*, vol. 9, no. 3, pp. 199-203, 2015.
- [145] B. Morrison *et al.*, "Compact Brillouin devices through hybrid integration on silicon," *Optical Engineering*, vol. 4, no. 8, pp. 847-854, 2017.
- [146] M. Smith, B. Kuhlmeier, C. M. de Sterke, C. Wolff, M. Lapine, and C. Poulton, "Metamaterial control of stimulated Brillouin scattering," *Optics letters*, vol. 41, no. 10, pp. 2338-2341, 2016.
- [147] A. Mocofanescu *et al.*, "SBS threshold for single mode and multimode GRIN fibers in an all fiber configuration," *Optics Express*, vol. 13, no. 6, pp. 2019-2024, 2005.
- [148] X. Hu, Q. Huang, Y. Lu, and Z. Meng, "Stimulated Brillouin Scattering Threshold in Presence of Modulation Instability for Optical Pulse in Long Optical Fiber," *Applied Sciences*, vol. 12, no. 21, p. 10868, 2022.
- [149] V. I. Kovalev and R. G. Harrison, "Threshold for stimulated Brillouin scattering in optical fiber," *Optics Express*, vol. 15, no. 26, pp. 17625-17630, 2007.
- [150] S. Gao *et al.*, "All-optical wavelength conversion based on four-wave mixing in silicon waveguides," in *9th International Conference on Optical Communications and Networks (ICOCN 2010)*, 2010, pp. 195-200: IET.

- [151] S. Sivanathan, M. A. Roula, N. J. Copner, and B. Copner, "Development of a Hardware for Frequency Scanning Interferometry for Long Range Measurement," in *2022 IEEE International Instrumentation and Measurement Technology Conference (I2MTC)*, 2022, pp. 1-6: IEEE.
- [152] J. Hansryd, P. A. Andrekson, M. Westlund, J. Li, and P.-O. Hedekvist, "Fiber-based optical parametric amplifiers and their applications," *IEEE Journal of Selected Topics in Quantum Electronics*, vol. 8, no. 3, pp. 506-520, 2002.
- [153] S. Signorini *et al.*, "Intermodal four-wave mixing in silicon waveguides," *Photonics Research*, vol. 6, no. 8, pp. 805-814, 2018.
- [154] E. D. Palik, *Handbook of optical constants of solids*. Academic press, 1998.
- [155] L. Zhang, A. M. Agarwal, L. C. Kimerling, and J. Michel, "Nonlinear Group IV photonics based on silicon and germanium: from near-infrared to mid-infrared," *Nanophotonics*, vol. 3, no. 4-5, pp. 247-268, 2014.
- [156] P. Apiratikul, A. M. Rossi, and T. E. Murphy, "Nonlinearities in porous silicon optical waveguides at 1550 nm," *Optics express*, vol. 17, no. 5, pp. 3396-3406, 2009.
- [157] I. Day *et al.*, "Tapered silicon waveguides for low insertion loss highly-efficient high-speed electronic variable optical attenuators," in *Optical Fiber Communication Conference*, 2003, p. TuM5: Optica Publishing Group.
- [158] A. Sure, T. Dillon, J. Murakowski, C. Lin, D. Pustai, and D. W. Prather, "Fabrication and characterization of three-dimensional silicon tapers," *Optics express*, vol. 11, no. 26, pp. 3555-3561, 2003.
- [159] J. J. Fijol *et al.*, "Fabrication of silicon-on-insulator adiabatic tapers for low-loss optical interconnection of photonic devices," in *Photonics Packaging and Integration III*, 2003, vol. 4997, pp. 157-170: SPIE.
- [160] V. R. Almeida, R. R. Panepucci, and M. Lipson, "Nanotaper for compact mode conversion," *Optics letters*, vol. 28, no. 15, pp. 1302-1304, 2003.
- [161] Z. Lu and D. W. Prather, "Total internal reflection–evanescent coupler for fiber-to-waveguide integration of planar optoelectric devices," *Optics express*, vol. 29, no. 15, pp. 1748-1750, 2004.
- [162] Q. Wang, T.-H. Loh, D. K. T. Ng, and S.-T. Ho, "Design and analysis of optical coupling between silicon nanophotonic waveguide and standard single-mode fiber using an integrated asymmetric super-GRIN lens," *IEEE Journal of Selected Topics in Quantum Electronics*, vol. 17, no. 3, pp. 581-589, 2010.
- [163] D. Taillaert *et al.*, "An out-of-plane grating coupler for efficient butt-coupling between compact planar waveguides and single-mode fibers," *IEEE Journal of Quantum Electronics*, vol. 38, no. 7, pp. 949-955, 2002.
- [164] G. Roelkens, D. Van Thourhout, and R. Baets, "High efficiency Silicon-on-Insulator grating coupler based on a poly-Silicon overlay," *Optics Express*, vol. 14, no. 24, pp. 11622-11630, 2006.
- [165] F. Van Laere *et al.*, "Compact and highly efficient grating couplers between optical fiber and nanophotonic waveguides," *Journal of lightwave technology*, vol. 25, no. 1, pp. 151-156, 2007.
- [166] J. Schrauwen, F. Van Laere, D. Van Thourhout, and R. Baets, "Focused-ion-beam fabrication of slanted grating couplers in silicon-on-insulator waveguides," *IEEE Photonics Technology Letters*, vol. 19, no. 11, pp. 816-818, 2007.
- [167] X. Chen, C. Li, and H. Tsang, "Characterization of silicon-on-insulator waveguide chirped grating for coupling to a vertical optical fiber," in *2008 IEEE/LEOS International Conference on Optical MEMs and Nanophotonics*, 2008, pp. 56-57: IEEE.

- [168] X. Chen, C. Li, and H. K. Tsang, "Fabrication-tolerant waveguide chirped grating coupler for coupling to a perfectly vertical optical fiber," *IEEE Photonics Technology Letters*, vol. 20, no. 23, pp. 1914-1916, 2008.
- [169] X. Chen and H. K. Tsang, "Polarization-independent grating couplers for silicon-on-insulator nanophotonic waveguides," *Optics letters*, vol. 36, no. 6, pp. 796-798, 2011.
- [170] Y. Pan, H. Liu, Z. Wang, J. Jia, and J. Zhao, "Optical constant and conformality analysis of SiO₂ thin films deposited on linear array microstructure substrate by PECVD," *Coatings*, vol. 11, no. 5, p. 510, 2021.
- [171] P. Girault *et al.*, "Integrated polymer micro-ring resonators for optical sensing applications," *Journal of applied Physics*, vol. 117, no. 10, p. 104504, 2015.
- [172] W. J. Joo *et al.*, "Metasurface-driven OLED displays beyond 10,000 pixels per inch," *Science*, vol. 370, no. 6515, pp. 459-463, Oct 23 2020.

Appendix

A.1 Script for CNSE method

The following code achieves the calculation of conversion efficiency with respect to wavelength by CNSE methods in Matlab. This function requires input parameters, including the effective index and mode area calculated by the FEM method in Comsol multi Physics software.

```
function [lambda_ss,CE,D2] = FWM_Schrodinger(neff,Aeff,f,P_p,lambda_p,L)
% FWM conversion eff calculation
c=2.99792e+008; % light speed m/s
P_s=100e-3; % Signal power (w)
P_i=0*0.01e-3; % Idler power (w)
alpha=2*1e2/(4.343); % linear loss
h=6.626*1e-34; % Planck constant
tau=1.1e-9; % Eq.(6) unit: s Carrier lifetime
beta_t=9.95e-12; % two photons absorption (m/W)
n2=5.59e-18; % non-linear Kerr index (m^2/W)
wav=c./f;
lambdaA=c./f;
Aeff_f=Aeff;
p_Aeff=polyfit(lambdaA,Aeff_f,5);
Aeff_1=polyval(p_Aeff,lambda_p);
beta=2*pi./wav.*neff;
K=301;
p=polyfit(f,beta,5);
beta0 = polyval(p,f);
f1=linspace(f(1),f(end),K);
beta00=polyval(p,f1);
lamda=c./f1;
omega=2*pi*f1;
diff_omega=mean(diff(omega));
beta1=diff(beta00)./diff_omega;
beta2=diff(beta1)./diff_omega;
D2=-2*pi*c./lamda(1:end-2).^2.*beta2;
D2=D2+D_mod*1e-6;
beta2=-D2.*lamda(1:end-2).^2./(2.*pi.*c);
beta3=diff(beta2)./diff_omega;
beta4=diff(beta3)./diff_omega;
beta22=[beta2(1) beta2 beta2(end)];
beta44=[beta4(1) beta4(1) beta4 beta4(end) beta4(end)];
neff00=spline(f,neff,f1);
D00=[D2(1) D2 D2(end)];
Dis_1=D00;
neff_1=neff00;
beta2_1=beta22;
beta4_1=beta44;
K=length(neff_1);
```

```

lambda_s=lamda; % signal wavelength
lambda_i=1./(2./lambda_p-1./lambda_s); % idler wavelenth
omega_s=2*pi*c./lambda_s;
omega_p=2*pi*c./lambda_p;
gamma_p_1=n2*2*pi./lambda_p/Aeff_1; % nonliear waveguide parameter
deltaK_1=beta2_1.*(omega_s-omega_p).^2+beta4_1.*(omega_s-omega_p).^4+
2*gamma_p_1*P_p;

[lambda_ss,CE] =
FWM(lambda_s,deltaK_1,lambda_p,P_p,P_s,P_i,Aeff_1,L,c,h,alpha,tau,beta_t,n2);

%%%%%%%%%%%%%%%%%%%%%%%%%%%%%%%%%%%%%%%%%%%%%%%%%%%%%%%%%%%%%%%%%%%%%%%%%%

function
[lambda_ss,CE]=FWM(lambda_ss,deltaKK,lambda_p,P_p,P_s,P_i,Aeff,L,c,h,alpha,tau,bet
a,n2)
K=length(lambda_ss);
for k=1:K
    k/K*100

lambda_s=lambda_ss(k); % signal wavelength
lambda_i=1./(2./lambda_p-1./lambda_s); % idler wavelenth
A_p0=P_p.^0.5; % Pump amplitutue
global A_s0;
A_s0=P_s.^0.5;
A_i0=1*P_i.^0.5;
f_p=c/lambda_p;
f_s=c/lambda_s;
f_i=c/lambda_i; % Frequency
sigma_p=1.45*1e-21*(lambda_p/(1546*1e-9)).^2;
sigma_s=1.45*1e-21*(lambda_s/(1546*1e-9)).^2;
sigma_i=1.45*1e-21*(lambda_i/(1546*1e-9)).^2;
gamma_p=n2*2*pi./lambda_p/Aeff; % nonliear parameter waveguide
gamma_s=n2*2*pi./lambda_s/Aeff;
gamma_i=n2*2*pi./lambda_i/Aeff;
deltaK=deltaKK(k);
[Z,A0]=ode45(@F,[0 L],[A_p0 A_s0 A_i0]);
Ap(k)=A0(end,1);
As(k)=A0(end,2);
Ai(k)=A0(end,3);
end

CE0=abs(Ai/(A_s0*0.8)).^2;
CE=10*log10(CE0);

function Q=F(z,A)
Q=zeros(3,1);

N_density_p=tau*beta*(lambda_p.*abs(A(1)).^4+lambda_s.*abs(A(2)).^4+lambda_i.*abs(
A(3)).^4)./2/h/c/Aeff^2;
N_density_s=tau*beta*(lambda_p.*abs(A(1)).^4+lambda_s.*abs(A(2)).^4+lambda_i.*abs(
A(3)).^4)./2/h/c/Aeff^2;
N_density_i=tau*beta*(lambda_p.*abs(A(1)).^4+lambda_s.*abs(A(2)).^4+lambda_i.*abs(
A(3)).^4)./2/h/c/Aeff^2;
alpha_p_FCA=sigma_p*N_density_p; % Free Carrier absorption
alpha_s_FCA=sigma_s*N_density_s;
alpha_i_FCA=sigma_i*N_density_i;

%All-optical wavelength conversion based on four-wave mixing in silicon waveguides

```

```
alpha_p_TPA=beta/Aeff.*(abs(A(1)).^2+2*abs(A(2)).^2+2*abs(A(3)).^2);
alpha_s_TPA=beta/Aeff.*(2*abs(A(1)).^2+abs(A(2)).^2+2*abs(A(3)).^2);
alpha_i_TPA=beta/Aeff.*(2*abs(A(1)).^2+2*abs(A(2)).^2+abs(A(3)).^2);

Q(1)=-0.5*(alpha+alpha_p_TPA+alpha_p_FCA).*A(1)+...
    i*gamma_p*(abs(A(1)).^2+2*abs(A(2)).^2+2*abs(A(3)).^2).*A(1)+...
    2*i*gamma_p.*conj(A(1)).*A(2).*A(3).*exp(i*deltaK.*z);
Q(2)=-0.5*(alpha+alpha_s_TPA+alpha_s_FCA).*A(2)+...
    i*gamma_s*(2*abs(A(1)).^2+abs(A(2)).^2+2*abs(A(3)).^2).*A(2)+...
    i*gamma_s.*conj(A(3)).*A(1).^2.*exp(-i*deltaK.*z);
Q(3)=-0.5*(alpha+alpha_i_TPA+alpha_i_FCA).*A(3)+...
    i*gamma_i*(2*abs(A(1)).^2+2*abs(A(2)).^2+abs(A(3)).^2).*A(3)+...
    i*gamma_i.*conj(A(2)).*A(1).^2.*exp(-i*deltaK.*z);
end
end
end
```

A.2 Mask Drawing for lithography



Figure A 1 Mask of a group of SOI waveguides with SU-8 cladding coupler at both ends.

The above figure is the mask of a group of SOI waveguides with SU-8 coupler. The zoom-in view clearly shows the SOI layer (red layer) covered by SU-8 layer (purple layer).

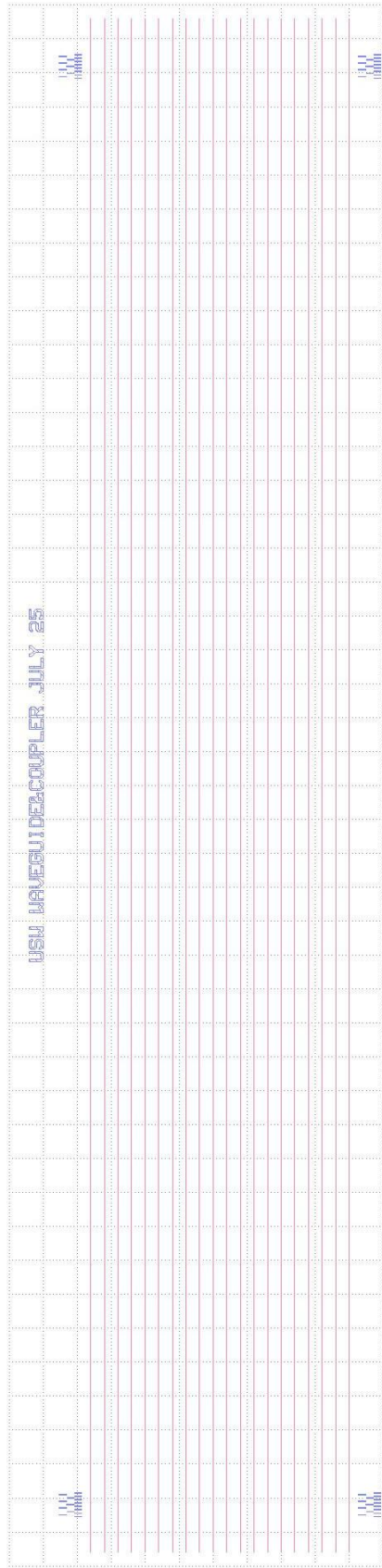


Figure A 2 Mask of a group of SOI waveguides with free space couplers

Because the waveguide length (~15mm) is far bigger than the width of the tip (~100 nm) and waveguide (500 nm), it is hard to observe the width change directly from the accurate scale mask scale. The cleaving mark at both ends indicates the position of the narrow waveguide (with the same width as the tip) part.

A.3 SOI chip with free space coupler

Two SOI chips with free space taper coupler were fabricated. Waveguides on those chips have not been grouped. Below figure A 3 is the microscope view of chip1; the photo is taken with three shots due to the limited view range of the microscope. As seen in the left part, many waveguides are discontinuous and partially missed, overly HF washing process may cause this damage. Therefore, most of the waveguides on this chip are not working. The lowest insertion loss measured is 5.8 dB for single-side coupling. In addition, the dotted rectangular in the right part marks a colour-changed area, the waveguide in this area is reddish, which is caused by the width change of the waveguide. Therefore, the taper part should be located in this area. As same as the chip with the SU-8 coupler, this chip also has a cleave angle at the right side, which is made to ensure at least one waveguide with the best cleave point.

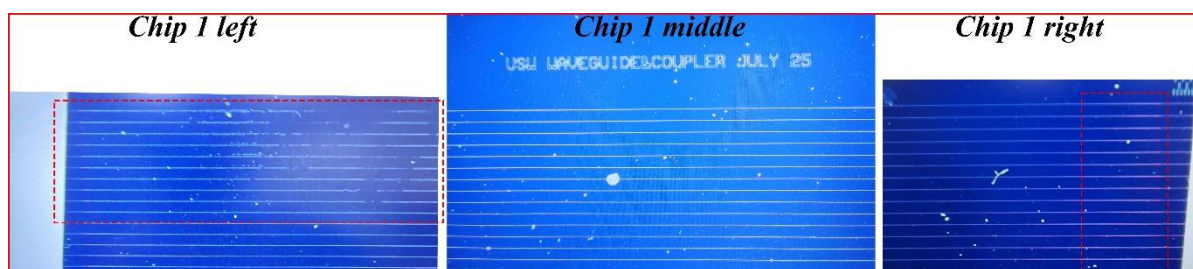


Figure A 3 Microscope view of SOI waveguide with free space taper coupler No.1.

The below figure is the photo of chip 2. All waveguides on this chip are fully functional, and no apparent damage is observed. The lowest insertion loss for single-side measured is 5.47 dB, which is still higher than the best value achieved by the SU-8 coupler.



Figure A 4 Microscope view of SOI waveguide with free space taper coupler No.2